UCLA
UCLA Electronic Theses and Dissertations

Title

Technological Advances and New Physiological Insights for Reliably Probing Myocardial Oxygenation with Magnetic Resonance Imaging

Permalink

https://escholarship.org/uc/item/77t7s1f6

Author

Yang, Hsin-Jung

Publication Date

2016

Peer reviewed|Thesis/dissertation

eScholarship.org Powered by the California Digital Library
University of California

UNIVERSITY OF CALIFORNIA

Los Angeles

Technological Advances and New Physiological Insights for Reliably Probing Myocardial Oxygenation with Magnetic Resonance Imaging

A dissertation submitted in partial satisfaction of the

requirements for the degree Doctor of Philosophy

in Biomedical Engineering

by

Hsin-Jung Yang

2016

© Copyright by

Hsin-Jung Yang

2016

ABSTRACT OF THE DISSERTATION

Technological Advances and New Physiological Insights for Reliably Probing Myocardial Oxygenation with Magnetic Resonance Imaging

by

Hsin-Jung Yang

Doctor of Philosophy in Biomedical Engineering

University of California, Los Angeles, 2016

Professor Daniel B. Ennis, Chair

Coronary artery disease (CAD) is the leading cause of death in the developed world. Evaluation of coronary function is critically important in the course of CAD management. Myocardial perfusion imaging (MPI) is the most popular noninvasive means of probing coronary function. While various imaging modalities have been used to image myocardial perfusion, the current clinical standards usually require the use of ionizing radiation or the exogenous contrast agent. The requirements increase the potential risks and render MPI infeeasible in a large segment of patients with CAD.

Blood oxygenation level dependent (BOLD) cardiac MRI (CMR) is a newer approach for imaging myocardial perfusion. BOLD CMR utilizes the intrinsic contrast of the deoxygenated blood to probe myocardial oxygenation without ionizing radiation and contrast agent.

Developments in the past twenty years have made significant advance in BOLD CMR and recent studies have shown promising results for the clinical application of the approach. However, BOLD CMR still suffer from multiple challenges, such as inadequate accuracy, imaging confounders, limited imaging speed, and sub optimal stress imaging protocols, all which significantly limit its reliability and clinical applicability. In this dissertation, we propose to overcome these limitations from the technical and physiological vantage points to enable a reliable BOLD CMR exam, which can rapidly accelerate the clinical translation and adoption of the approach.

The first objective of this dissertation is to develop, test and validate a cardiac MRI technique that is robust, reliable and fast. To overcome the challenging cardiac imaging condition at 3T and provide reliable and sensitive BOLD signal, this dissertation utilized multiple techniques, such as motion correction, SR preparation, adiabatic pulses and novel reconstruction methods, to realize a confounder-corrected, free-breathing 3D T2 mapping technique at 3T that can be completed within the period of adenosine stress. The technique was tested and validated with simultaneously acquired ^{13}N-ammonia PET perfusion in a whole-body PET/MR system. Ex-vivo studies demonstrated the proposed approach could be used to overcome the heart-rate dependent changes in T2 between rest and stress. In canines without coronary stenosis, T2 under adenosine stress was significantly greater than at rest, which was consistent with the observed increase in PET perfusion measurements. The changes in BOLD signal between rest and stress was highly correlated to myocardial perfusion reserve. In animals with coronary stenosis, perfusion anomalies were consistently detected between the developed technique and PET. These results demonstrate the proposed approach has the capability to enable rapid and reliable measurements of whole heart perfusion.

The second objective of the dissertation is to explore innovative vasodilation strategies to improve the reliability and applicability of BOLD CMR exams. Two novel ways of inducing vasodilation (Regadenoson and hypercapnia) for BOLD CMR were studied. Regadenoson is a new pharmacological vasodilator that has a prolonged vasodilation effect compared to the standard stress agent (adenosine). Utilizing the longer vasodilation period, we found that a significantly improved stress image quality and reliability can be achieved by imaging at a delayed time point (10 mins after the regadenoson administration). For validation purpose, BOLD and PET images were acquired simultaneously in healthy animals. The delayed acquisitions showed markedly increased myocardial T2 from the BOLD images and increased myocardial blood flow from ^{13}N-ammonia PET perfusion. To further improve the sensitivity and reliability of regadenoson BOLD exam, a repeated BOLD image acquisition strategy was proposed to continuously monitor the dynamics of BOLD signal after regadenoson injection. The BOLD signal changes were used to investigate the coronary dynamics after the peak vasodilation in healthy and diseased subjects. The coronary dynamic parameters (CDPs) were derived and were used to compare to the conventional single time point approach. CDPs showed the capability of extracting greater BOLD response in the healthy subjects and improved performance in disease identification in the animals with impaired coronary arteries. This preliminary study showed the potential of improving BOLD CMR performance with existing stress agents and better-designed strategies to assess coronary vasodilatation.

Hypercapnia (elevated arterial CO2 ($PaCO_2$)) is a known mediator of carotid vasodilation, but its effects on the coronary arteries had been unclear given the lack of tools to accurately and rapidly alter arterial CO2. By prospectively and independently controlling PaCO2, this dissertation first investigated whether a physiologically tolerable hypercapnic stimulus can

increase MBF in healthy and diseased animals. The extent of effect on MBF due to hypercapnia was compared to adenosine using quantitative ^{13}N-ammonia PET measurements. In the healthy animals, MBF under hypercapnia and adenosine were positively correlated; and were not different. Under LAD stenosis, MBF increased under hypercapnia and adenosine but the effect was significantly lower in the affected territories. Mean perfusion defect volumes measured with adenosine and hypercapnia were significantly correlated and were not different. The BOLD MR signal response to the controlled hypercapnia was also investigated under similar setup. In intact canines, changes in myocardial BOLD MR signal were equivalent to changes with adenosine. In addition, BOLD response under repeat hypercapnic stimulations were also tested. Reproducible BOLD responses were observed following repeat stimulation between baseline and equivalent hypercapnic states. In the dogs with coronary artery stenosis, BOLD MR signal changes during hypercapnia and adenosine infusion were also not different. The results demonstrate arterial blood CO_2 tension is an independent variable of MBF, which can induce MBF and BOLD signal to the same level as standard dose of adenosine.

In summary, this dissertation culminates in key advancements which have the capacity to reliably advance cardiac BOLD in the clinical arena in the assessment of myocardial perfusion in the setting of ischemic heart disease. The technical and physiological advances direly address the key obstacles present with in the current BOLD techniques and build the foundation for a reliable, robust and practical myocardial BOLD exam.

This dissertation of Hsin-Jung Yang is approved.

Danny Jiong Jiong Wang

Peng Hu

Rohan Dharmakumar

Daniel B. Ennis, Committee Chair

University of California, Los Angeles

2016

This dissertation is dedicated to my family, my friends and my loved ones.

Table of Contents

LIST OF FIGURES

LIST OF TABLES

LIST OF ABBREVIATIONS

1D/2D/3D – One/two/three dimensional

ANOVA – Analysis of variance

BOLD – Blood Oxygenation Level Dependent

bSSFP – Balanced steady-state free precession

CAD – Coronary arteries diseases

CCC – Cross-correlation coefficient

CKD – Chronic kidney disease

CHD – Coronary heart disease

CNR – Contrast-to-noise ratio

CT – Computed tomography

CTP – Computed tomography Perfusion

ECG – Electrocardiography

FFR – Fractional Flow Reserve

FLASH – Fast low angle shot

FOV – Field of view

GRAPPA – Generalized auto-calibrating partially parallel imaging

LAD – Left anterior descending coronary artery

MBF – Myocardial blood flow

MCE Myocardial contrast echocardiography

MI – Myocardial infarction

MPI – Myocardial perfusion imaging

MR – Magnetic resonance

MRI – Magnetic resonance imaging

NAV – Diaphragm navigator

$PaCO_2$ – Partial pressure of CO_2 in arterial blood

PaO_2 – Partial pressure of O_2 in arterial blood

$PetCO_2$ – Partial pressure of CO_2 in end-tidal (end exhaled) gas

$PETO_2$ – Partial pressure of O_2 in end-tidal (end exhaled) gas

PET – Positron emission tomography

RF – Radio-frequency

ROI – Region of interest

SD – Standard deviation

SNR – Signal-to-noise ratio

SPECT – Single-phaton emission computed tomography

XCA – X-ray coronary angiography

SD – Standard deviation

SPO2 – Blood oxygen saturation

ACKNOWLEDGEMENTS

I would like to express my gratitude for the mentorship of Prof. Rohan Dharmakumar. I am glad to have joined his group at its fast growing phase, which gave me multiple opportunities for being exposed to a wide spectrum of MRI research. My experiences have inspired me tremendously and built a solid foundation for innovative ways to tackle outstanding questions. I benefited hugely from all the support and countless discussions with Dr. Dharmakumar throughout the years of working on multiple projects and most importantly learned the mindset of passion and dedication for research. I also want to extend by gratitude to my committee co-chair Dr. Daniel Ennis, and members Dr. Peng Hu, Dr. Zhilin Qu, and Dr. Danny JJ Wang for their advice and guidance in my qualifying exam and for constructing this dissertation.

In addition, I would like to thank the BIRI family at Cedars Sinai Medical Center. The plentiful resources and brilliant coworkers at BIRI provided the perfect environment for me to find the paths through the dark roads of research. Special thanks go to all the members including but not limited to the faculties (Dr. Debiao Li, Dr. Damini Dey, Dr. Piotr Slomka, Dr. Behzad Sharif and Dr. Zhaoyang Fan), the fellow researchers (Dr. Ivan Cokic., Dr. David Chen, Zixin Deng, Dr. Avinash Kali, Dr. Qi Liu, Dr. Christopher Nguyen, Dr. Jianning Pang, Jaime Shaw, Dr.Yibin, Xie, Dr. Qi Yang and Zhengwei Zhou), and the support research staff (Dr. Richard Tang, Laura Smith, Ed Gill, Hernan Rios, Lawrence St. John, Johanna Kim, Amy Smith, Eileen Shinn, Christy Woo, Kimberly Okamoto, and Sabrina Sides).

My sincere thanks to the Siemens support team (Dr. Xiaoming Bi, Dr. Yutaka Natsuaki, and Dr. Gerhard Laub) for helping me with pulse sequence development. I would also like to thank the collaborators from Lawson Health Research Institute (Dr. Frank S. Prato, Jane Sykes, John

Butler) and University of Toronto (Dr. Joseph Fisher, Michael Klein, Olivia Sobczy) especially for all their help and support during the intense experiments, all of which have lead to important publications.

Last but not the least, I would like to extend my thanks to my family: my parents (Jesse Yang and Shirley Hsiao), my sister, my brother in law (Lisa Yang, Jason Yang) and my two lovely nieces (Tobi Yang and Bonnie Yang). Their unconditional supports carried me through the ups and downs in my research days and left me without worries for fully dedicating myself to the work.

BIOGRAPHICAL SKETCH

Education

Master of Science in Electrical Engineering, Northwestern University, Evanston, IL 2010

Bachelor of Engineering in Department of Photonics,

National Chiao-Tung University, Hsinchu, Taiwan 2008

Peer-Reviewed Journal Publications

1. **Yang HJ**, Tang RL, Cokic I, Klein M, Kali A, Sharif B, Smith L, Tang J, Tsaftaris S, Li D, Conte AH, Fisher J, Yumul R, Dharmakumar R. Assessment of Myocardial Reactivity to Controlled Hypercapnia with Free-Breathing T2-Prepared Cardiac Blood-Oxygen-Level-Dependent MR. Radiology, 2014, 272(2): 397-406.
2. **Yang HJ**, Sharif B, Pang J, Kali A, Bi X, Cokic I, Li D, Conte AH, Dharmakumar R. Free-Breathing, Motion-Corrected, Highly-Efficient Whole-Heart T2 Mapping at 3T with Hybrid Radial-Cartesian Trajectory. Magnetic Resonance in Medicine, 2015 (*Published Online Before Print*).
3. **Yang HJ***, Kali A*, Cokic I*, Yee R, Tang RL, Tighiouart M, Wang X, Jackman WM, Chugh SS, White JA, Dharmakumar R. Malignant Ventricular Arrhythmias in Patients with Chronic Myocardial Infarction and Predictive Value of Iron-Sensitive Cardiac Magnetic Resonance Imaging. Circulation: Cardiovascular Imaging, 2015 (*equal contribution).
4. Kali A*, Cokic I*, Wang X, Tang RL, **Yang HJ**, Thajudeen A, Shehata M, Amorn AM, Enzhao L, Stewart B, Bennett N, Harlev D, Tsaftaris SA, Jackman WM, Chugh SS, Dharmakumar R. Iron Deposition Following Chronic Myocardial Infarction as a Substrate for Cardiac Electrical Anomalies: Initial Findings in a Canine Model. PLoS One, 2013, 8(9): e73193 (*equal contribution)
5. Kali A, Cokic I, Tang RL, **Yang HJ**, Sharif B, Marban E, Li D, Berman D, Dharmakumar R. Determination of Location, Size and Transmurality of Chronic Myocardial Infarction without

Exogenous Contrast Media Using Cardiac Magnetic Resonance Imaging at 3T. Circulation: Cardiovascular Imaging, 2014, 7(3): 471-481.

6. Kali A*, Choi EY*, Sharif B, Kim YJ, Bi X, Spottiswoode B, Cokic I, **Yang HJ**, Tighiouart M, Li D, Berman DS, Choi BW, Chang HJ, Dharmakumar R. Native T1 Mapping at 3T can Characterize Chronic Myocardial Infarctions in Patients. JACC Cardiovascular Imaging, 2015 Sep;8(9):1019-30 (*equal contribution).
7. Zhou Z, Bi X, **Yang H**, Dharmakumar R, Arsanjani R, Wei J, Bairey Merz CN, Li D, Sharif B. First-pass myocardial perfusion imaging with reduced subendocardial dark-rim artifact using optimized Cartesian sampling. *Journal of Magnetic Resonance Imaging* 2016; In Press. DOI: 10.1002/jmri.25400
8. Kali A, **Yang HJ**, Cokic I, Tang RL, Sharif B, Dharmakumar R. Robustness of Native Myocardial T1 Maps at 3T for Chronic Infarct Characterization. Journal of Cardiovascular Magnetic Resonance, 2015
9. Yang HJ, Dey D, Sykes J, Klein M, Butler J, Kovacs MS, Sobczyk O, Sharif B, Bi X, Kali A, Cokic I, Tang RL, Yumul R, Conte AH, Tsaftaris SA, Tighiouart M, Li D, Slomka PJ, Berman DS, Prato FS, Fisher JA, Dharmakumar R. Arterial CO2 can Potentiate Myocardial Blood Flow to the Same Extent as Adenosine. (Submitted for Initial Review)
10. Yang HJ, Dey D, Sykes J, Butler J, Bi X, Sharif B, Kali A, Cokic I, Li D, Tsaftaris SA, Slomka P, Prato FS, Dharmakumar R. Fast, Heart-Rate Independent, Whole-Heart, Free-Breathing, Three-Dimensional, Quantitative Myocardial BOLD MRI at 3T with Simultaneous 13N-Ammonia PET Validation in Canines. JACC: Cardiovascular Imaging. 2016 (Submitted for Initial Review)
11. Kali A, Cokic, Tang R, Dohnalkova A, Kovarik L, Yang HJ, Andreas Kumar, Prato FS, Wood JC, Underhill D Marbán E, Dharmakumar R Persistent Microvascular Obstruction Following Myocardial Infarction Culminates in the Confluence of Ferric Iron Oxide Crystals, Proinflammatory Burden and Adverse Remodeling. Circulation: Cardiovascular Imaging (Under Editorial Revision)

Chapter 1: Introduction

1.1 Significance

Coronary Artery Disease (CAD) is the most common type of heart disease and the number one cause of death in the United States (1). Reliable detection and quantification of the ischemic volume associated with prognostically significant CAD are critically important in the clinical management of the disease (2,3). Ischemia testing is commonly used to assess the extent and severity of myocardial ischemia, which have been shown to provide incremental prognostic value over standard clinical variables across the spectrum of presentations of CAD (2,4,5).

1.2 Current State of Ischemia Testing

For many years, x-ray contrast angiography (XCA) has been used as gold standard for CAD evaluation. However, the determination of coronary artery stenosis on the basis of XCA or coronary CTA has proven to be a poor predictor of ischemic burden (6,7). While Fractional flow reserve (FFR), determined as the relative pressure differences across the stenotic coronary artery, has emerged as the new standard for determining clinically significant ischemia (FFR $\leq$0.75) (8-10), it is invasive, expensive, and exposes the patient to ionizing radiation. Direct measures of ischemic burden may be determined on the basis of SPECT, PET, CT perfusion, MCE, and first-pass perfusion MRI (FPP-MRI) (11-14). While SPECT and PET studies account for approximately 90% of the nearly 10-million myocardial ischemia-testing studies in the US (15), the sensitivity and specificity for both methods combined for the determination of severe ischemia is below 70% (16). CT perfusion, MCE and FPP-MRI are relatively newer approaches

that require the use of exogenous contrast media and intravenous pharmacological stress agent (adenosine), all carrying significant risks and side effects in certain patient populations (17).

An ideal test to assess for myocardial ischemia would be truly non-invasive and would have minimal potential risks and side effects; that is, in addition to avoiding the risks of cardiac catheterization, it would be free of ionizing radiation, exogenous contrast media, and intravenous stress-agents. Additionally, the strategy would provide physiological insight into the disease based on reliable measurements of impaired oxygen supply, and not from surrogate tests (wall motion, ECG changes, or contrast kinetics).

Although current clinical standards do not provide many of these benefits, a number of these requirements can be met by cardiac Blood-Oxygen-Level-Dependent (BOLD) Magnetic Resonance Imaging (MRI) (18-20). However, the widespread use of this approach is currently limited by inadequate accuracy, undesirable imaging confounders, and the need for intravenous stress, all of which pose considerable limitations in clinical practice. A highly efficient, robust, and accurate BOLD exam with minimum stress inducing side effects is hugely beneficial for the patients that are limited from the current medical standard methodologies.

1.3 Noninvasive, Ionizing Radiation Free, Non-Contrast-Enhanced Ischemia Testing with Myocardial BOLD MRI

BOLD (Blood-Oxygen-Level-Dependent) MRI, relies on endogenous contrast mechanism (changes in blood oxygen saturation, $\%O_2$) to identify ischemic territories. The intrinsic contrast derived on the basis of $\%O_2$ using MRI makes BOLD imaging free of exogenous contrast agent and ionizing radiation. Although FPP-MRI is another approach which enables the acquisition of

high resolution perfusion images without ionizing radiation, it requires infusion of gadolinium-based contrast agents, which are toxic to patients with late stage chronic kidney disease (CKD) (21-23). Given the comorbidity of CKD in patients with heart disease, FPP-MRI is estimated to be contraindicated in at least 1 million patients in the US(24-26). Importantly, late stage CKD patients who cannot undergo FPP-MRI are in great need of ischemia assessment since the risk of cardiac mortality is substantially elevated in this population(27,28). Thus, there is an unmet and growing need for accurate assessment of chronic MI without contrast agents in this patient population.

The potential benefits of BOLD MRI for detecting global or regional myocardial ischemia due to CAD were demonstrated by our group and others at least a decade ago (29-32). Although a number of pilot clinical studies have demonstrated the feasibility of using BOLD MRI for identifying clinically significant myocardial ischemia due to CAD, the method is currently limited by several technical and physiological challenges.

1.4 Major Challenges of Cardiac BOLD MRI

1.4.1 Technical Challenges

Although BOLD CMR has progressed significantly in the past 20 years, a number of technical challenges still limit its reliability, robustness and applicability in the clinical routines. Major technical challenges include:

- Limited imaging speed and coverage to accommodate the limited vasodilation time.
- Imaging confounders (T1 weighing, coil bias and heart rate dependency) degrade the BOLD sensitivity.

- 2D methods with multiple breath holds can lead to patient discomfort and slice mismatch.
- Limited sensitivity due to modest contrast to noise ratio (CNR), particularly at lower field strength (1.5T).
- Image artifacts (cardiac and respiratory motion; B0 and B1 field inhomogeneity) particularly at 3T leads to diminished imaging quality.
- Weighted images sacrifice the potential of quantitative evaluation of the BOLD effect (33).

In addition to the aforementioned technical limitations, another important component of of BOLD CMR exams are the need for vasodilation.

1.4.2 Physiological Challenges

When exercise stress testing is contraindicated (in nearly 50% of patients) (34), existing imaging modalities use pharmacologic stress agents such as adenosine to induce hyperemia. Although the stress agents can induce vasodilation for imaging purpose, the current stress methods rely on imaging within a short period of time (2-4 mins) with unpredictable and rapidly changing cardiac activities to capture the peak coronary vasodilatory state. The suboptimal imaging conditions are compensated by other modalities with lower spatial resolution, higher contrast to noise ratio and the use of contrast agents. Although several BOLD studies have shown promising results adopting similar approaches, such procedures are not optimal for BOLD CMR acquisitions. For BOLD acquisitions to be reliable, images need to be of high quality and should have sufficient image contrast. The current stress methods hold key challenges against BOLD MRI, which are:

- Unpredictable cardiac activity leading to motion artifacts, undesired confounders and cardiac phase mismatch during stress imaging.

- Marked changes in cardiac activity, which can lead to, increased oxygen consumption during image acquisition and decrease the BOLD response during hyperemia.
- Restricted peak vasodilatory duration during adenosine stress limits the spatial resolution resolution and coverage, and the reliability of BOLD images due to motion artifacts.

Thus, both technical and physiological challenges restrict the robustness and reliability of BOLD CMR in the clinical settings. A practical BOLD CMR technique would needs to overcome the limitations to accurately and rapidly identify the ischemic myocardium.

1.5 Specific Aims of This Dissertation

The overall aim of this dissertation is to improve the technical and physiological changes facing cardiac BOLD MRI in order to pave the path for effective clinical translation. To achieve this, we wish to first develop a suitable BOLD CMR sequence and validate it against gold standard PET perfusion; and second to develop novel vasodilation strategies which can enhance the reliability of cardiac BOLD exams.

1.5.1 Aim 1: To develop a time-efficient, confounder-corrected, free-breathing, quantitative, 3D myocardial BOLD MRI with full LV coverage at 3T and validate the approach against simultaneously acquired quantitative PET perfusion.

A Fast free breathing T2 mapping sequence tailored for BOLD CMR was developed and is described in n chapter 3. Chapter 3.1 presents the highly efficient T2 mapping platform. This technique utilizes motion-correction algorithm with contrast integration to achieve high imaging efficiency whole heart T2 mapping. The T2 accuracy and feasibility of the technique were tested with an animal model with acute MI. In chapter 3.2, a saturation-recovery pulse was added to further reduce scan time and eliminate confounding effects caused by heart rate changes leading

to bias in T2 estimation. The BOLD response from the proposed sequence is validated with simultaneously acquired ^{13}N-ammonia PET perfusion imaging.

1.5.2 Aim 2: To develop and test innovative vasodilation strategies that combine imaging, post-processing, and analysis methods for reliably and safely measuring myocardial BOLD response.

Chapter 4 and 5 summarize two different novel vasodilation strategies to improve imaging reliability and stress safety. Chapter 4 explores the use of Regadenoson (a newer and safer vasodilator) for cardiac BOLD exam. The delayed vasodilation effect of regadenoson was tested for more reliable stress imaging while enabling further insights into coronary dynamics (vasodilation and relaxation).

Chapter 5 explores the use of precisely targeted hypercapnia as a safer and repeatable vasodilator. The vasodilation effect was validated with quantitative PET perfusion and BOLD CMR. The study serves as a foundation for a more sophisticated paradigm design using repetitive hypercapnic stimulations.

Chapter 2: Background

2.1 Coronary Artery Disease

Coronary artery disease is the leading cause of death in the United States in both men and women. It is estimated that in excess of 16 million people are living with CAD in the US and more than one in three deaths are due to CAD and more than 1 million people are hospitalized each year. The most common form of CAD leads to the narrowing of the coronary arteries (stenosis) resulting in reduced blood flow and oxygen supplied to the heart muscle, causing myocardial ischemia – a condition where the oxygen demand of the myocardium is far in excess of the available supply (35). The presence of myocardial ischemia is an important risk factor for major adverse cardiac events (MACE: stroke, myocardial infarction, and death) (36,37). Appropriate early interventions (pharmacological, or medical therapy (OMT), angioplasty (PCI), coronary bypass (CABG)) that are guided by the extent and severity of ischemic burden associated with stable CAD may be instrumental in reducing the risk of MACE (4-6) . Hence a reliable, non-invasive, and repeatable method for determining the extent and severity of ischemia is invaluable in managing patients with CAD.

2.2 Assessment of CAD on the Basis of Coronary Function

Current CAD assessments evaluate either anatomy or function of the coronary arteries. Although coronary anatomy is an important indicator of CAD and is associated with coronary function under controlled conditions (Fig.2.1), the coronary function is a more direct way of probing the actual oxygen supply to the myocardium. Coronary function can also be disassociated with coronary anatomy in the presence of diffuse stenosis and arterial remodeling. (38)

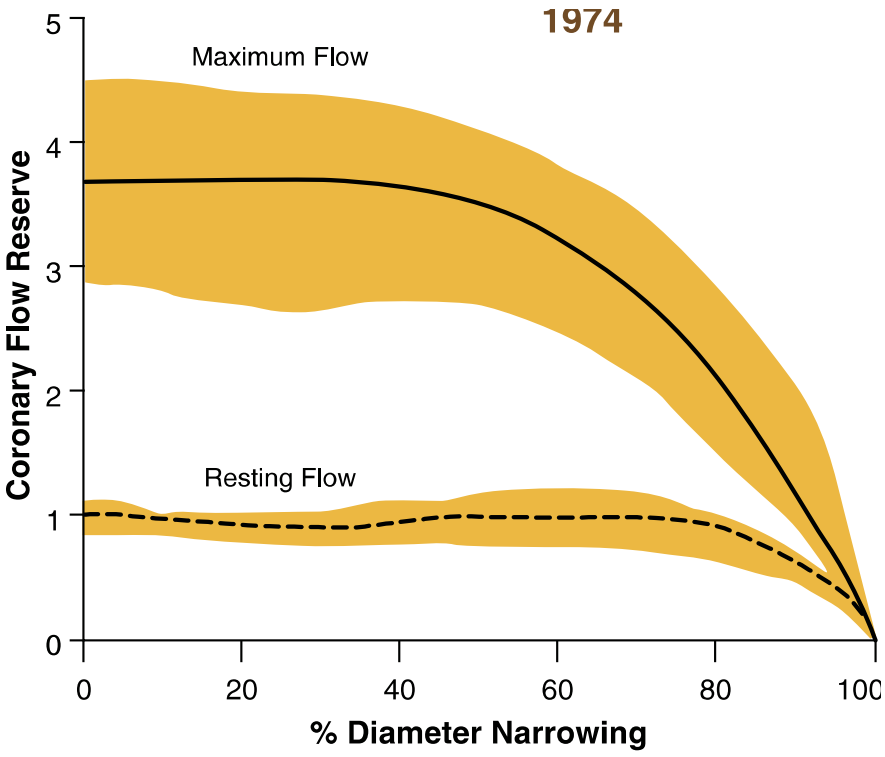

Figure 2.1 Relationship between coronary flow reserve and coronary stenosis level. The figure showed the effect of coronary narrowing on coronary flow reserve. The maximum flow is degraded when the stenosis level is higher than 50%. Adopted from (38)

In addition, measuring only anatomical stenosis in large coronary arteries is not sufficient to detect ischemia in the presents of coronary microvascular disease and limits the accuracy for evaluating myocardial ischemia. Recent studies have shown improved clinical outcome from functional assessments (Fig. 2.2) (8,9,39,40) and indicate functional measures offer superior guidance in the management of CAD.

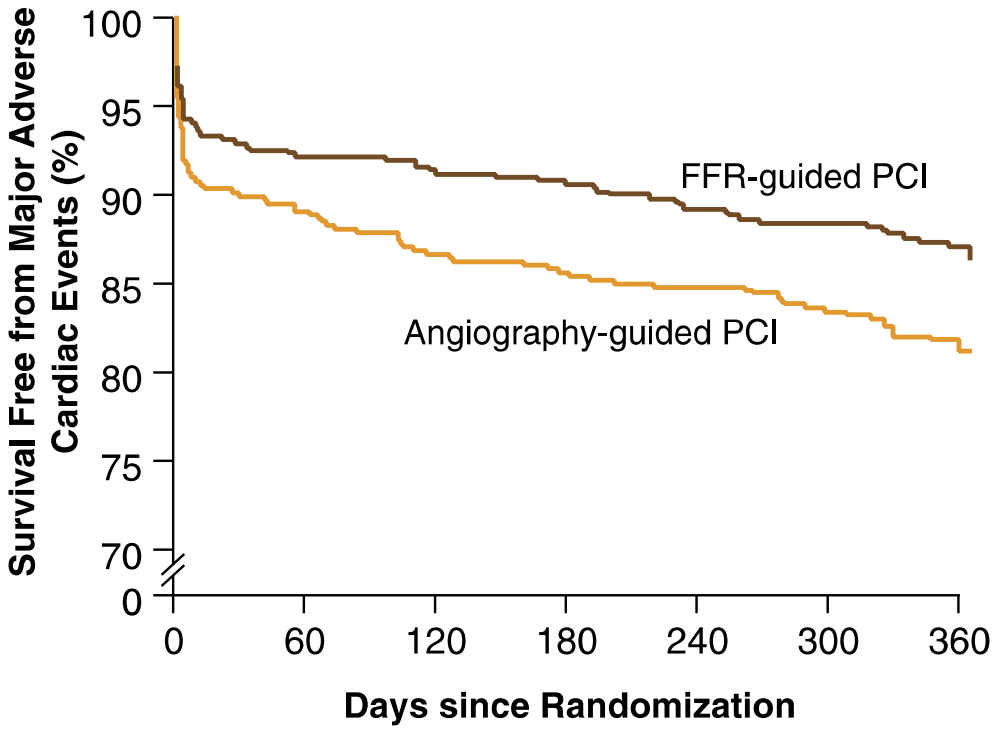

Fig2.2 Treatment outcome difference between Angiography-guided and FFR-guided PCI. FFR guided PCI showed significantly reduced ratio of major adverse events compare to anatomical angiography guided procedures. Adopted from (9)

The current gold standard of evaluating coronary function (FFR, XCA) are still invasive and the extra operational risk, patient discomfort and cost from the invasive procedures make it less suitable for patients with modest symptoms and lower CAD risk. The imaging-based ischemia tests serve as an effective noninvasive alternative for the patient population suspected of having CAD.

2.3 Imaging-based Ischemic Testing

Imaging-based ischemic testing investigates the vasodilatory capacity of coronary arteries using noninvasive imaging modalities and identify the coronary vessels that are affected by disease.

One of the most direct measurements of coronary vasodilation is through the monitoring of myocardial perfusion. Under vasodilatory stress, the normal coronary circulation will increase blood flow and oxygen supply to the myocardium. However, in the stenotic coronary arteries, the vessels lose the ability to dilate, which will lead to hypoperfusion or even ischemia. Imaging the difference of myocardial perfusion between rest and stress can identify the myocardial supplied by the affected arteries, which has significant diagnostic and prognostic values. In the past 20 years, considerable growth in Imaging-based cardiac stress testing because of the advancement in technology and the proven diagnostic values. The incidence of imaging based stress testing has increased to more than 85% in all stress exams and is considered a critical diagnostic tool in CAD management (41). Imaging-based ischemic testing can generally be defined in two steps: Step 1. Induction of cardiac stress resulting in coronary vasodilation. Step 2. Imaging myocardial perfusion changes induced by the stimulation and identifies the ischemic territories. Details of each step are discussed in the following sections.

2.3.1 Myocardial Perfusion Reserve (MPR) and Coronary Vasodilation

Coronary perfusion is a well-regulated physiologic phenomenon. Modulating myocardial blood flow is extremely important in balancing myocardial oxygenation. Because of the high (60~80%) myocardial oxygen extraction fraction in the left ventricle under regular condition (42), it is not possible to significantly increase O_2 consumption by increasing O_2 extraction. Consequently, increased oxygen demand is mainly met by the elevation of coronary blood flow (43). Healthy coronary arteries are capable of modulating the myocardial perfusion by 3-5 folds during maximal vasodilation. This myocardial perfusion reserve (MPR) provides a large buffer for extra oxygen demand. The vasodilation process is illustrated in the upper panel in fig 2.3. However, in coronary arteries affected by disease, such as with epicardial stenosis arising from

atherosclerosis, increase the coronary resistance and leads to the reduction of the vasodilation capability. This effect decreases the maximum myocardial blood flow during peak vasodilation and reduces the myocardial perfusion reserve (MPR) in the affected myocardium. (43) The property makes MPR a valuable feature of probing coronary health condition.

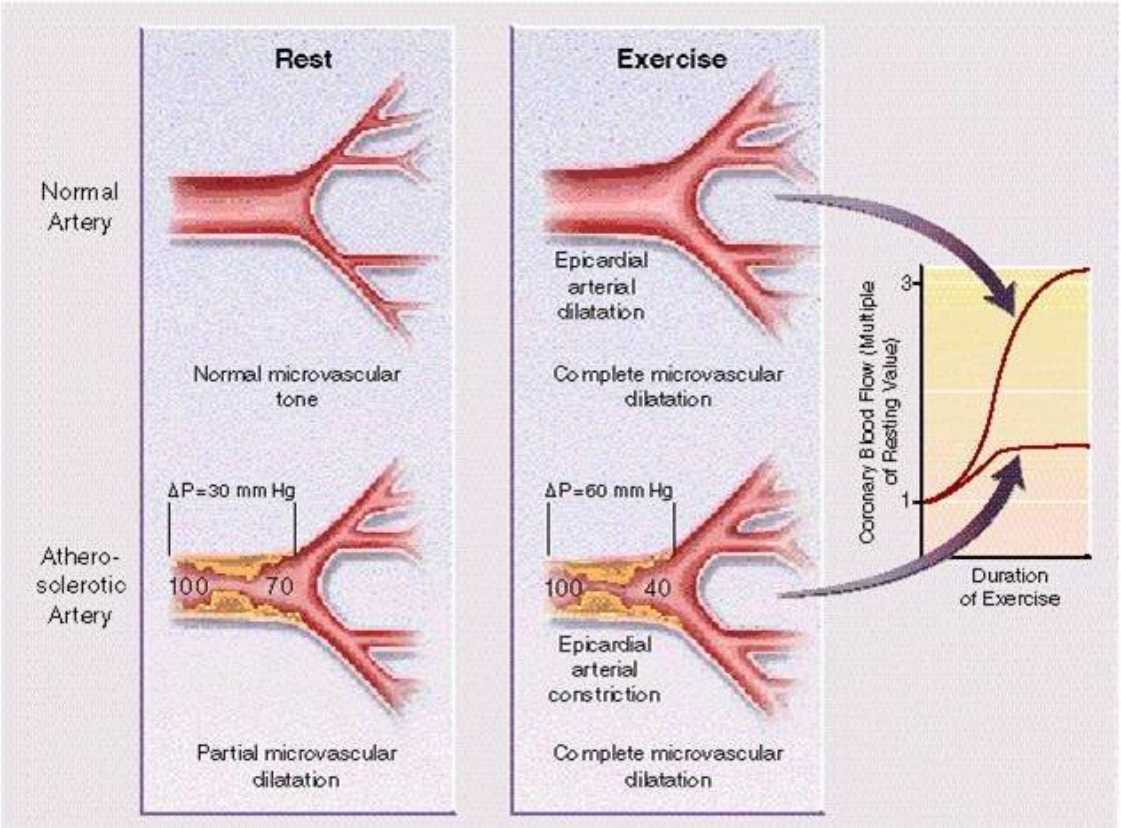

Fig. 2.3 Normal and diseased blood flow between rest and stress. Healthy and stenotic artery reaction to the increased oxygen demand during exercise. Artery stenosis reduce the maximum blood flow during exercise and reduce the blood flow reserve. Adopted from (44).

To probe MPR, various methods, including exercise, pharmacological agents and blood gas modulation are used to induce coronary vasodilation. In imaging studies, pharmacological stress is the most common way to induce peak vasodilation due to the ease of administration. Recent studies have used controlled hypercapnia and breathing maneuver to induce vasodilation for

identifying coronary arteries with significant stenosis (45,46). While each vasodilation approach has its own strengths and weaknesses, suitable stimulations should be selected to best accommodate the features of the applied ischemic testing modality. Comparisons of various methods used to induce coronary vasodilation are listed in table 2.1

Stress Methods	Mechanism	Oxygen Consumption During Stress	Cardiac Activity During Peak Vasodilation	Repeat Stimulation Capability
Exercise	Non-Pharmacological Intrinsic	Significantly Elevated	Very Unstable (Increased contractility)	Difficult to repeat (Patient condition)
Dobutamine	Pharmacological Inotropic	Significantly Elevated	Very Unstable (Increased contractility)	Unrepeatable (Dose Limitation)
Dipyridamole	Pharmacological Chronotropic+	Unhanged or slightly elevated	Unstable (Heart rate variation)	Unrepeatable (Long Half-Life)
Adenosine	Pharmacological Chronotropic+	Unhanged or slightly elevated	Unstable (Heart rate variation)	Unrepeatable (Dose Limitation)
Regadenoson	Pharmacological Chronotropic+	Unhanged or slightly elevated	Very Unstable (Heart rate variation)	Unrepeatable (Long Half-Life)
Hypercapnia	Non-Pharmacological Intrinsic	Unhanged or slightly elevated	Stable with small heart rate variation	Repeat stimulation with controlled hypercapnia

Table 2.1 Stress property comparisons between vasodilation methods. Different levels of oxygen consumption elevation, imaging stability and repeat stimulation capability during stress imaging makes the methods suitable for different imaging modalities.

2.3.2 Myocardial Perfusion Imaging (MPI)

After inducing vasodilation, measuring myocardial perfusion is the important next step for MPR evaluation. Myocardial perfusion can be imaged with several modalities, such as SPECT, PET, CT, ultrasound, and MRI, noninvasively. The imaging properties and contrast mechanisms are summarized in table 2.2 and each modality has its own strength and weakness and can be chosen to accommodate different clinical needs. Despite the differences between modalities, the majority of current MPI techniques utilize ionizing radiation and use exogenous contrast agents as surrogates of the blood and measure myocardial perfusion by monitoring contrast agent dynamics. These features induce extra risks besides the catheterization procedure and make MPI contraindicated in certain patient population; on the other hand, BOLD CMR is one of the new imaging modalities, which does not require the use of ionizing radiation and exogenous contrast agent. This provide BOLD CMR a preferable risk profile compare to the standard MPI approaches and make it suitable for the patients that need repeat measurements or are contraindicated to contrast agents.

MPI Modalities	Ionizing Radiation	Contrast Agent	Contrast Mechanism	Spatial Resolution
SPECT	Yes	Radioactive Isotopes	Myocardial tracer uptake	6-8 mm
PET	Yes	Radioactive Isotopes	Myocardial tracer uptake	3-5 mm

CTP	Yes	Iodinated	Contrast first passage	<1 mm
MCE	No	Microspheres	Microspheres replenishment	3-5 mm
FFP MRI	No	Gd-based	Contrast first passage	1-3 mm
BOLD MRI	No	No	Blood oxygenation level	1-3 mm
ASL MRI	No	No	Arterial Spin labeling	1-3 mm

Table 2.2 Summary of the MPI modalities.

2.4 Fundamentals of Blood-Oxygenation-Level-Dependent (BOLD) MRI

Image contrast permitting the detection of BOLD signal changes originate from nuclear relaxation of spins in a spatially heterogeneous magnetic fields that are determined by the oxygenation state of the red blood cells. The following sections summarize the key elements of nuclear magnetic relaxation theory and the foundations of BOLD image contrast.

2.4.1 Nuclear Magnetic Relaxation

Nuclear Magnetic Resonance (NMR) signal is generated from the interaction between unpaired protons (spins) in atoms and applied external magnetic fields. Among different elements, such as ^{1}H, ^{23}Na, and ^{31}P, hydrogen protons (^{1}H) in the water is the most used element for medical MRI due to the high water content in human bodies. When an ensemble of hydrogen protons is placed into a static external magnetic field (B_0), the spins will be aligned to the direction of B_0 and split into two energy states (up-state and down-state). At thermal equilibrium, the exceeded spin population in the up-state lead to a non-zero magnetic dipole moment (M_0) along the B_0

direction. However, the existence of M_0 is typically too small to be detected in steady magnetic systems. In order to generate measurable signal from M_0, a time-varying orthogonal magnetic field (B_1) with on resonance frequency $\omega_0 = \gamma B_0$ (γ is the Lamor frequency; γ=42.7MHz/T for ^{1}H) needs to be applied. The B_1 field can apply a torque to M_0 which can rotate the magnetization vector by a prescribed flip angle angle (α) depend on the amplitude and duration of the B_1 field. This process is called excitationof the spins. The excited M_0 will precess along the static field at ω_0. The tilted magnetization vector creates a rotating magnetic moment in the transverse plane (M_{xy}), which can be detected with an on resonance antenna. When B_1 is turned off, the longitudinal (M_z) and transverse components (M_{xy}) of the excited magnetization vector will relax back to the thermal equilibrium at a rate of T_1 and T_2, respectively.

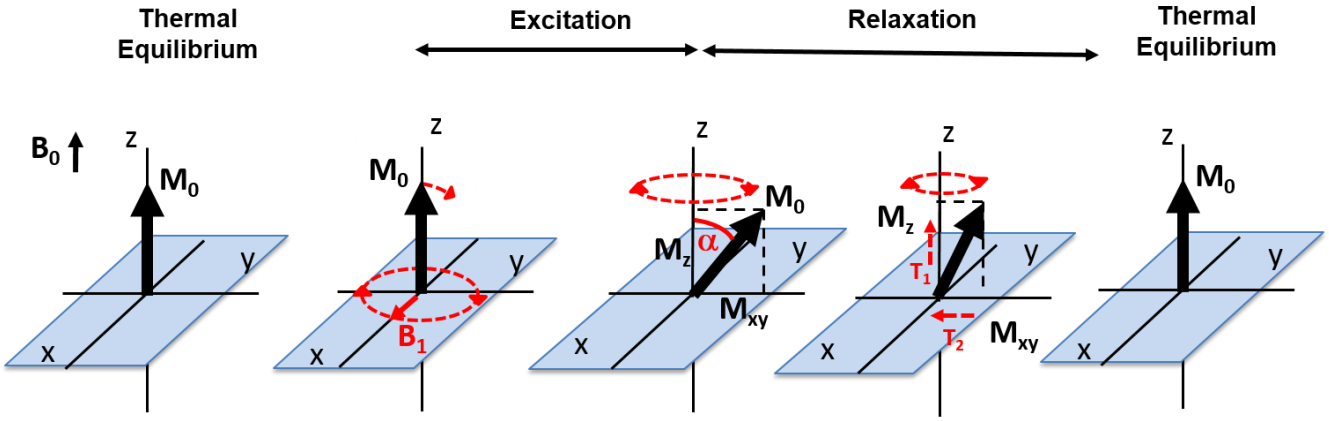

Fig 2.4 A cartoon representation of the spin excitation and relaxation process. M_0 is first excited with a B_1 field by α in the first half of the coordinates. In the second half of the coordinates, the magnetization slowly relaxes back to the thermal equilibrium with a rate of T1 in the longitudinal direction (M_z) and T2 in the transverse direction (M_{xy}).

This process is known as spin relaxation and can be described by the phenomenological Bloch equations (112):

$$\frac{dM_x}{dt} = \Delta\omega_{off} M_y - \frac{M_x}{T_2}$$

$$\frac{dM_y}{dt} = \Delta\omega_{off} M_x - \frac{M_y}{T_2}$$

$$\frac{dM_z}{dt} = \frac{M_0 - M_z}{T_1}$$

Where $\Delta\omega_{off}$ is the off resonance frequency of a spin and can be defined as $\Delta\omega_{off} = \omega_0 - \omega$

In a perfect on resonance environment where $\Delta\omega_{off} = 0$, we can derive the temporal representation of the relaxation process to be:

$$M_x(t) = M_x(0)e^{-\frac{t}{T_2}}$$

$$M_y(t) = M_y(0)e^{-\frac{t}{T_2}}$$

$$M_x(t) = M_z(0)e^{-\frac{t}{T_1}} + M_0(1 - e^{-\frac{t}{T_1}})$$

This simplified representation provides a general picture of the MRI contrast mechanisms and is important because:

- The measured MR signal is proportional to the transverse magnetization ($M_{xy} = M_x \hat{\imath} + M_y \hat{\jmath}$; where $\hat{\imath}$ and $\hat{\jmath}$ represent unit vectors in the x and y direction respectively), which is related to M_0, α, t, T_1 and T_2. By carefully choosing the imaging parameters (α, t), one will be able to generate MR signal and contrasts that is sensitive to specific MR parameters (M_0, T_1, and T_2).
- MR parameters, such as M_0, T_1 and T_2, are closely correlated to the surrounding environment of the spins (details will be provided in the following sections), which is often connected with physiological conditions. Probing the MR parameters can provide

important information on the micro and macro environment around the water molecules, which can reflect in different pathological features.

In practice, there are more complicated components that can influence the MR signal. Off resonance spins, modulations of the excitation and relaxation process can all impact the spins and generate different contrasts or artifacts. In this dissertation we will focus on the basic principles that are related to the blood oxygenation level sensitive parameters and discuss its application in the ischemic stress testing.

2.4.1.1 Longitudinal Relaxation

As mentioned earlier, the post-excitation longitudinal magnetization recovers to thermal equilibrium with a time constant T_1. The longitudinal relaxation is established by two processes, which are spontaneous emission and stimulated emission. In the biological environment, spontaneous emission is typically very slower, which makes the stimulated emission the dominant effect for longitudinal magnetization recovery. Stimulated emission occurs as the nuclei experience rapid changing magnetic fields that is close to the resonance frequency. In MRI, the origin of the fluctuating magnetic fields is typically caused by the rotation, translation and collision of the hydrogen nuclei to surrounding molecules. This effect makes T_1 sensitive to the magnetic property of the surrounding molecules and the mobility of the hydrogen itself.

2.4.1.2 Transverse Relaxation

The transverse component of the magnetization relaxes to the thermal equilibrium state with a relaxation constant T_2. Unlike the longitudinal magnetization, the transverse relaxation decays to zero in time. As discussed in the previous section, the transverse magnetizations are precessing against the B_0 direction in the x-y plane. This means the magnetization can be decomposed into

an amplitude term and a phase term and the total M_{xy} can be think of a complex superposition of the individual spins. When the bulk magnetic field is homogeneous, transverse relaxation is mainly composed from two mechanisms. (i) The energy transformation from spin-lattice relaxation as mentioned in the last section. The effect brings a spin back to the low energy state and reduce the transverse component; and (ii) the magnetization cancelation between the local incoherent spins caused by phase accumulation and dipolar interaction. Because of the second mechanism, T_2 is always shorter than T_1. The phase accumulation is strongly dependent on the local molecular environment and the spin mobility during the relaxation period. In this dissertation, we define the T_2 that is not affected by imperfect field perturbation as the intrinsic T_2 (T_2^{Intr}) of the spins. In the presents of field inhomogeneity; on the other hand, the local spins will be exposed to a range of different B_0 ($\Delta B = B_0$ max-B_0 min) and be precessing at a different frequency. This effect accelerates the dephasing process of the transvers magnetizations and shorten the transverse relaxation time. It is common practice in MRI literature to define the shorten relaxation constant as T_2* where

$$\frac{1}{T_2^*} = \frac{1}{T_2^{Intr}} + \gamma \Delta B$$

Fortunately, the magnetization dephasing caused by a slowly spatial varying static field inhomogeneity is possible to be recovered with the use of 180^o refocusing pulses. {ref Hahn; 1950; spin echo} The signal generated by reversing the accumulated phase from the inhomogeneous field is called spin echo (SE) and the refocusing process is demonstrated in figure 2.5.

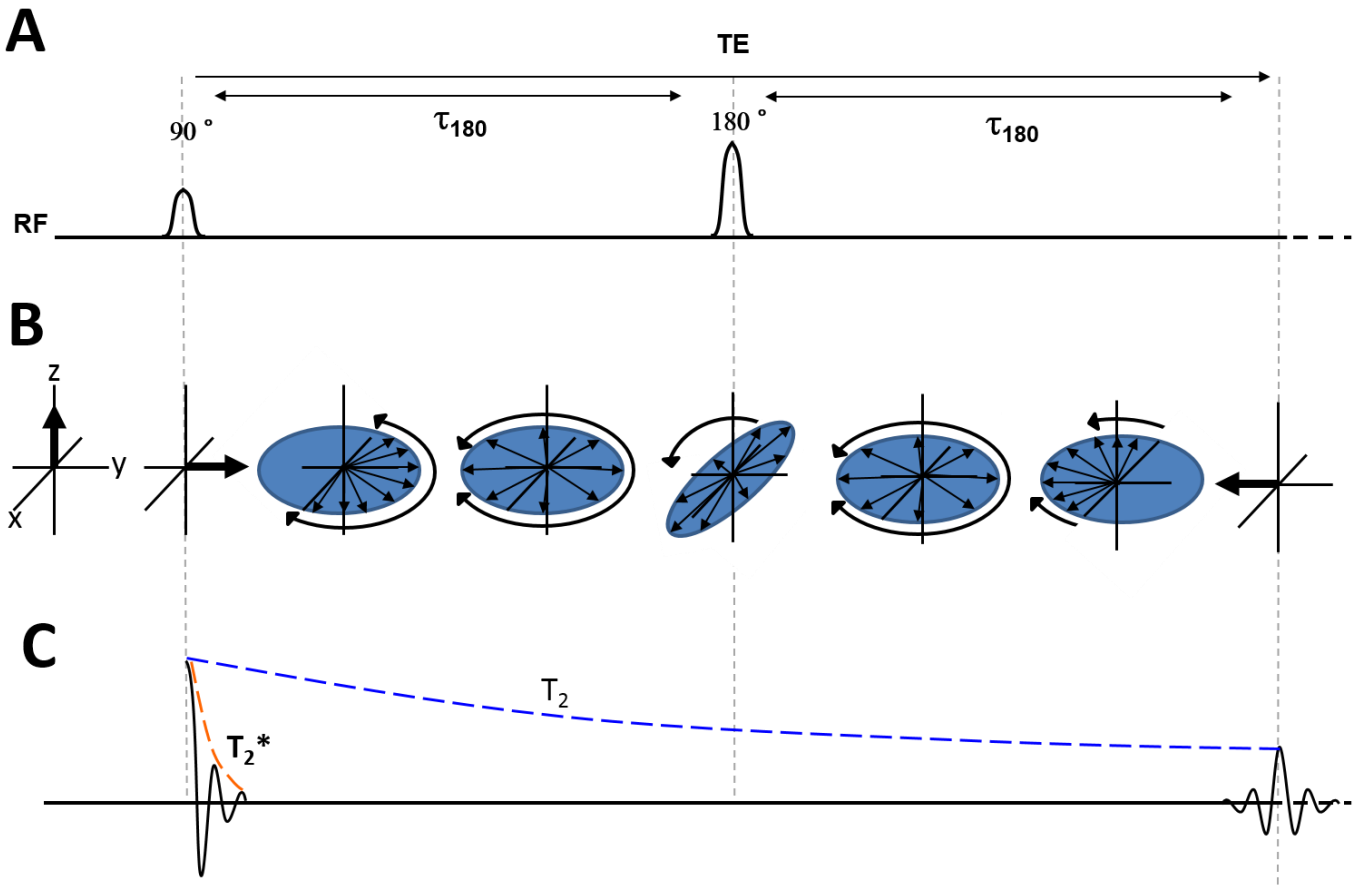

Fig 2.5 Spin echo formation and T_2 relaxation. (a) A 90° RF excitation pulse is followed by a 180° RF pulse that is applied at a time of τ_{180} after the 90° RF pulse. (b) Shows a schematic of spins losing coherence due to T_2 effects following the 90° RF pulse over the time period of τ_{180}. The 180° RF pulse reverses the direction of phase evolution to increase coherence over the next τ_{180}, forming an echo which peaks at time of 2 τ_{180} after the 90° RF pulse. (c) Shows the exponential decay of the echo peaks (blue curve) occurring over the period of 2 τ_{180}, the time constant of which is T_2, also shown is the T_2* decay curve (orange line). Note that spin-echo extends the time over which the transverse magnetization persists, without which T_2* decay would more rapidly dephase the transverse magnetization.*

As plotted in the figure, a 180^o pulse can reverse the phase accumulation by flipping the spin to precess in the opposite direction. In a slowly spatial varying field where spins do not move through different field offsets during the refocusing period (τ_{180}), the spins will experience identical field perturbation before and after the 180^o pulse and generates a perfect refocused

spins at t =2τ_{180}. This condition makes the spin echo $T_{2\ equals}$ to the intrinsic T_2 ($T_2^{SE} = T_2^{Intr}$). Nonetheless, in MRI, there are often sources of local magnetic field variations that produce fast spatial varying inhomogeneous fields. When spins diffuse through such inhomogeneous environment, the random phase accumulation leads to an enhanced spin dephasing. Even with the application of a refocusing pulse, due to the random motion of diffusion, the phase perturbation through the process is difficult to reproduce during the refocusing period. The effect, therefore, results in a further reduced apparent T_2 value compare to T_2^{intr}. The apparent T_2 under the influence of diffusion can be expressed by

$$\frac{1}{T_2^{SE}} = \frac{1}{T_2^{Intr}} + \frac{1}{T_2^{Diff}}$$

Where T_2^{Diff} is a function of refocusing time (τ_{180}), field variation components, molecular mobility resonance frequency and diffusion path. Substances with susceptibility shift from the water molecules are often the source of inducing local field variation. In the case of BOLD imaging, the susceptibility change of the deoxygenated hemoglobin makes a perfect source for local field perturbation and creates transvers relaxation differences in both refocused and non-refocused scenarios.

2.4.2 BOLD Contrast

Hemoglobin is the main component for oxygen transportation in the blood. It is composed of four heme groups surrounding a globin group. Each heme group contains an iron atom to bind with oxygen. When heme is not bound to oxygen, the iron(II) in the heme group is paramagnetic with 4 unpaired electrons in the 3D orbit. When a heme becomes oxygenated, oxygen molecules

bind to the iron and change the confirmation of the protein and rendering them diamagnetic (47,48). The process is plotted in figure 2.4.

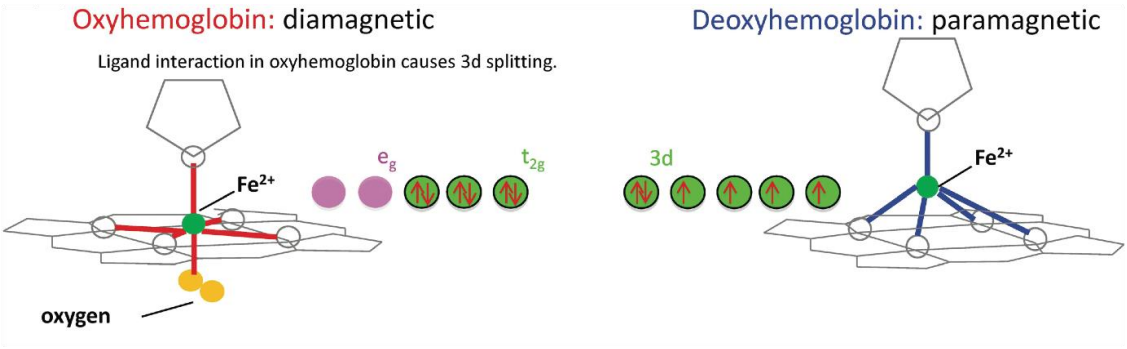

Fig.2.6 Molecule structure of deoxygenated and oxygenated hemoglobin. Binding oxygen to the heme group induces structural change of the molecules and turn transform the magnetization. Adopted from (48)

The capacity of the hemoglobin to alter magnetic susceptibility makes blood a magnetically inhomogeneous medium in which the susceptibility is strongly depend on the blood oxygen saturation ($\%O_2$). The susceptibility variation from deoxygenated hemoglobin creates local magnetic field inhomogeneity which cause a loss of phase-coherence among spins following radio-frequency (RF) excitation and reduce the capability of refocusing the transverse magnetization (in excess of spin-spin relaxation in the absence of field inhomogeneity), which leads to a shorter T2* and apparent T2 in the blood (49).

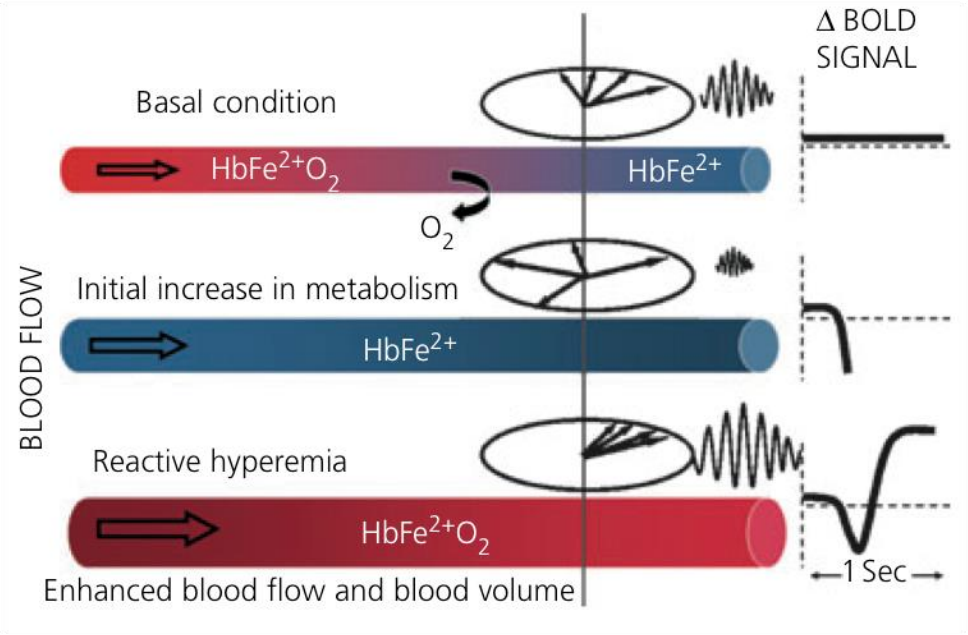

Fig. 2.7 BOLD signal changes from neural stimulations. Neural stimulation increases oxygen consumption, which reduce the blood oxygenation level in the local vessels and induce the increase in the blood flow. The blood oxygenation level affects the spin refocusing property and lead to BOLD signal changes. Adopted from (49)

The MR signal variation correspond to the blood oxygenation level, also known as Blood-Oxygenation-Level-Dependent (BOLD) signal, was first discovered by Dr. Ogawa in 1990 (50). Two years later, the effect was applied to human brains for the first time by two independent groups led by Dr. Ogawa (51) and Dr. Kwong (52). These studies built the foundation of functional MRI (fMRI) and opened the door for the modern cognitive and behavioral neuroscience. In the Brain, blood supply changes during neural stimulations and, as a secondary effect, modulates blood oxygenation (Fig.2.5). This phenomenon provides neuroscientist an in-direct tool to probe regional neuron activity through monitoring BOLD signal changes. On the other hand, the application of BOLD contrast in the heart provides an opportunity to assess the myocardial oxygenation directly. As mentioned in the previous chapters, myocardial ischemia is

an important indicator for CAD, which makes BOLD CMR a viable approach for CAD assessment.

2.5 BOLD contrast in the Myocardium

In the heart, nearly 90% of the blood volume is within the capillaries.(53) In the microcirculation, similar to the BOLD mechanism in the blood, field inhomogeneity induced by deoxygenated hemoglobin also influences the water molecules in the capillary bed with the interaction between the red blood cells and plasma and between the intravascular and extravascular spaces. Consequently, myocardial BOLD signal reflects the oxygenation level of the microcirculation and makes the BOLD signal sensitive to both the supply and demand of myocardial oxygen. During stress testing, vasodilators induced hyperemia in the healthy myocardium and the increased blood flow boosts oxygen supply in the capillary bed. When myocardial oxygen consumption stays the same, blood oxygenation level elevates substantially in the microcirculation (~30% (resting) vs. ~80% (hyperemic)); (54) on the other hand, myocardial blood flow in the myocardium subtended by stenotic coronary arteries do not respond to the stress agent results in unchanged or reduced oxygenation level and BOLD signal (Fig 2.6.). This difference allows for detecting coronary stenosis on the basis of regional myocardial BOLD signal variations.

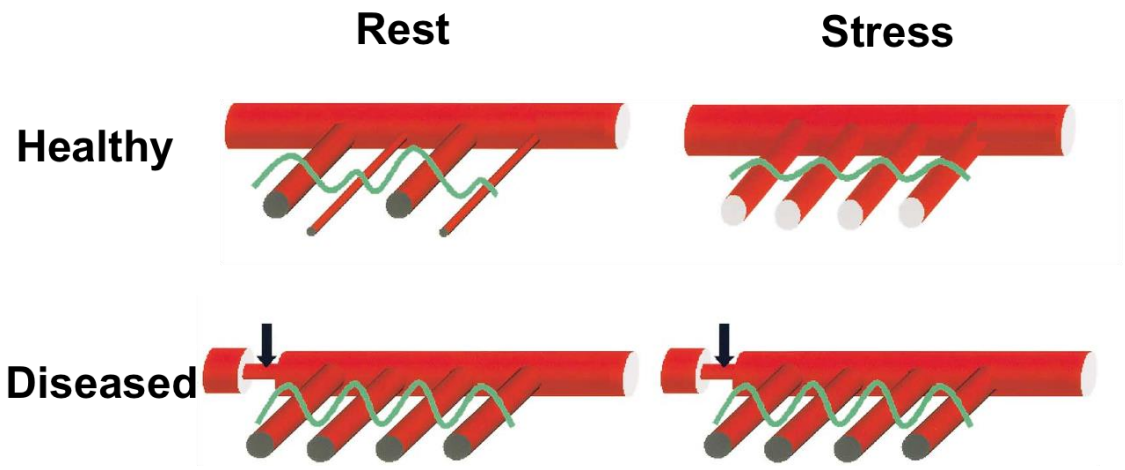

Fig. 2.8 Healthy and diseased coronary microcirculation under rest and stress. In healthy coronary arteries, vasodilation capability is reserved under rest condition and maintain the blood oxygenation level according to the myocardial oxygen demand. On the contrary, the vasodilation reserve is exhausted in the diseased arteries under rest condition to accommodate the impaired blood supply and loss the capability of further dilate the vessels under stress condition. This effect makes the oxygenation level difference between healthy and diseased myocardial territories and lead to the change in BOLD signal. Adopted from (54)

Although the BOLD contrast was originally developed for brain and became a game changer in neuroscience, imaging BOLD signal in brain is always a challenging task due to the limited BOLD contrast (1-3% signal elevation in the active regions) (50,52). To overcome the effect, various statistical algorithms have been developed to extract meaningful values from the signal that is buried in the noise level (35). Even with the success from sophisticated statistical testing, higher BOLD contrast is always desired in the BOLD experiments. Fortunately, important biophysical differences between the microcirculation in heart and brain enhance the applicability for BOLD ischemic testing. Specifically, the heart has a larger blood volume fraction than the brain (~10% vs. ~4%) and lower venous blood oxygen saturation (30% Vs. 60%)(55). This allows for a wider range of signal change with vasodilator-induced hyperemia in the myocardium compared to the brain, which provides greater BOLD sensitivity in the heart.

However, the challenge for myocardial BOLD CMR has been identifying oxygenation changes from confounding effects of imaging artifacts from motion (cardiac, respiratory and pulsatile blood flow), as well as, susceptibility difference between heart and lung interface.

2.5.1 Biophysics of BOLD Contrast

As BOLD contrast is originated from susceptibility changes of the red blood cells, susceptibility sensitive (T_2*-based) sequences are the most straightforward choices for BOLD imaging (56). Although T_2* yield high sensitivity against blood oxygenation level, it is also sensitive to bulk susceptibility artifacts (57), field inhomogeneity, and frequency shift from off resonance spins. These shortcomings are particularly prominent in the heart due to the heart-lung interface at high field scanners. The effects significantly reduce the intra- and inter-subject reproducibility and reliability of T_2*-based sequences. T2-based imaging is also sensitive to susceptibility variations as described in the previous sections. Because of the refocusing property, T_2 is less sensitive to the slow varying field variation generated from large vessels. Although this effect sacrifices the BOLD sensitivity and make T_2 less sensitive to blood oxygenation compare to T_2*, it also makes the T_2 contrast more specific to the oxygenation level of the capillary blood and microcirculation (Fig.2.7) (58).

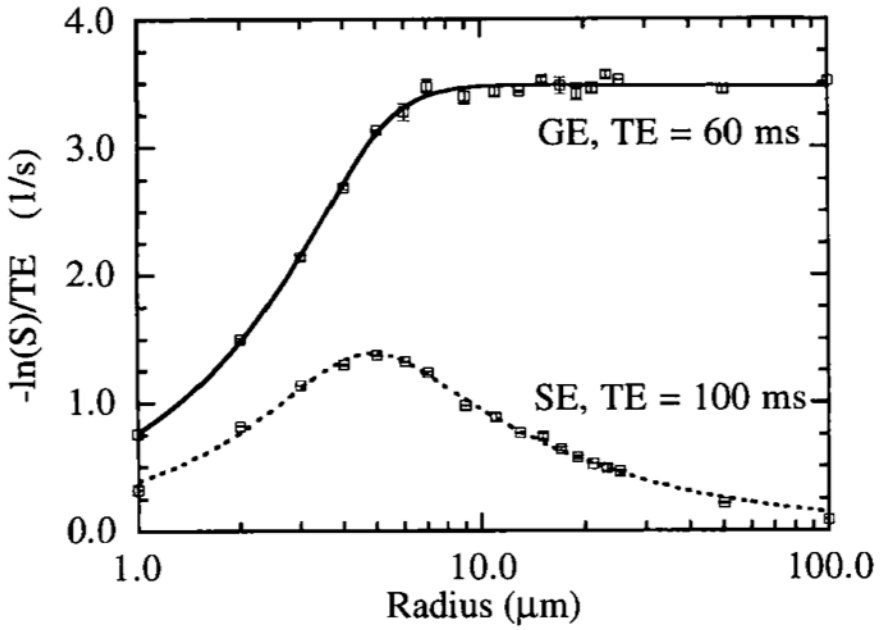

Fig.2.9 T_2(SE) and T_2(GE) BOLD sensitivity against vessel radius. ΔT_2 signal peaks for microvessels(5μm) and ΔT_2*signal peaks for macrovessels. Although ΔT_2* signal exceeds ΔT_2 signal at all radii, the targeted sensitivity for the capillary vessels makes T_2 more physiological relevant to myocardial ischemic testing. Adopted from (58)*

This effect makes T_2 more physiologically relevant to ischemic testing, especially because ~90% of the blood in the myocardium is in the capillaries. In addition, T_2 is also less sensitive to confounders such as temperature, and bulk field inhomogeneity, which makes it more reliable in the challenging cardiac enviroment (59).

More recently, a new approach utilizing the T_2-based contrast with balanced steady state signal free precession (bSSFP) was proposed to generate cardiac phase resolved BOLD images (60). Fine parameter selection of bSSFP sequence can increase T_2 contrast in the signal and create BOLD sensitivity. bSSFP sequences also provide a better tolerance to the inhomogeneous main magnetic field compared to T_2* images. However, strong bulk shift in B_0 in the myocardium,

which is not uncommon in high field scanners, can still lead to imaging artifacts and degrade image reliability.

2.5.2 Main Magnetic Field Strength

BOLD sensitivity is highly correlated with the field strength (B_0) because the field perturbation generated from paramagnetic hemoglobin ($\Delta B=\Delta\chi B_0$) increases proportionally with the B_0 (61). The effect increases BOLD sensitivity in the high field scanners and is prominent in both T_2* and T_2 BOLD contrasts(61,62) .

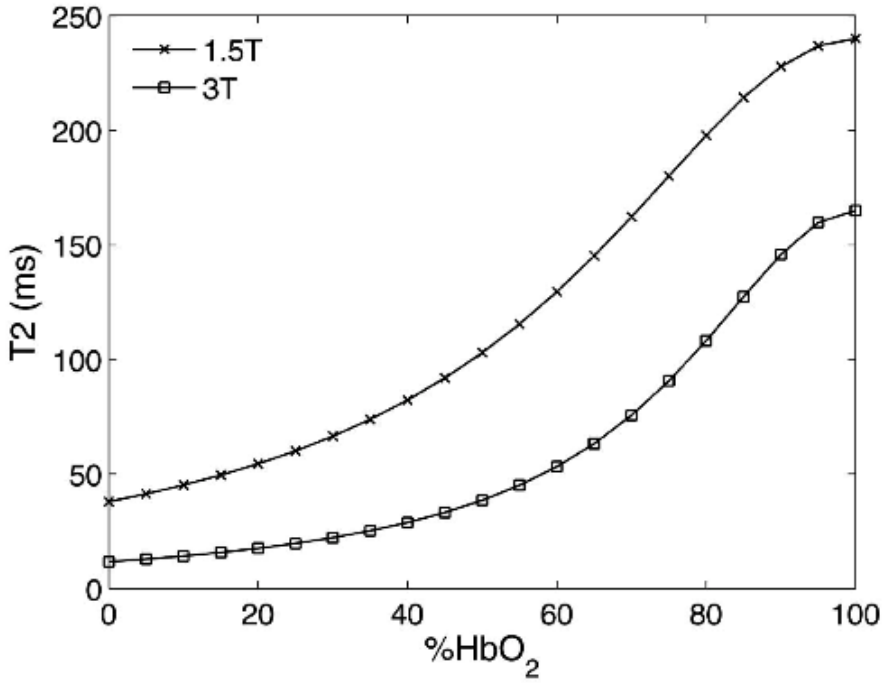

Fig 2.10 Simulated T_2 signal with different blood oxygenation level under 1.5T and 3T. Larger BOLD response is observed under 3T compare to 1.5T. adopted from (62)

However, the increased susceptibility difference also magnifies the imaging artifacts caused by tissue-air interface and main field inhomogeneity. T_2-based images, benefiting from the spin refocusing process, yield (20) more robust against to the off resonance spins compared to the T_2* sequences, which makes T_2 BOLD imaging more robust at higher magnetic fields. Moreover, in addition to the susceptibility disturbance, the higher field strength also influences the B_1 field homogeneity and T_1 of the tissue, which can induce additional confounders complicating the interpretation of BOLD signal changes.(20)

2.5.3 Quantitative BOLD

Given the image quality, fast image acquisition and short breath-hold duration (31,63), T2 weighted- images, such as T2-prepared bSSFP and T2-prepared GRE, have become popular among the choice of myocardial BOLD approaches that are available (20,64-67). Although the studies showed promising results in detecting CAD, confounders and imaging artifacts still limit the reliability and clinical applicability of the techniques, especially at 3T. Confounders, such as coil sensitivity, heart rate dependency and T1 contamination, from the weighted images can disturb the limited BOLD signal changes and diminish the acquisition reliability and accuracy. In contrast, quantitative T2 mapping can eliminate the confounders by acquiring absolute T2 values. Despite the advantages the current T2 mapping approaches offer, they are mostly limited by imaging speed, resolution, coverage and accuracy. Further technical advances and systematic evaluation are needed to enable robust clinical imaging.

2.5.4 Physiological Consequences of Vasodilatory Stress and its Relevance to BOLD CMR

Imaging under peak vasodilatory stress is particularly challenging for cardiac BOLD MR. Although FPP MRI is capable of acquiring single-shot images under cardiac stress using parallel

imaging and other acceleration methods, the use of gadolinium contrast ensures high CNR. In contrary, BOLD CMR has limited CNR, cannot easily adopt image acceleration strategies and thus requires long acquisitions. The current stress methods and protocols are mostly designed for the conventional imaging modalities, which can be problematic when applied to BOLD CMR for the following reasons:

- Elevated oxygen consumption and unpredictable cardiac activity during imaging acquisition.

Certain inotropic vasodilators, such as dobutamine, increase oxygen consumption with elevated myocardial contractility under vasodilation, which can degrade blood oxygenation changes and diminish the myocardial BOLD response. Chonotropic vasodilators, such as dyprimadole, adenosine and regadenoson, although ensure that myocardial oxygen consumption stays unchanged, are often accompanied by physiological modulations particularly at the initial phase of the stress (irregular cardiac motion, rapidly changing heart rate during acquisition, significantly shorter quiescent period available for data acquisition). These effects lead to motion artifacts and confound image contrast both of which can mask the BOLD response from the stress images. In addition, BOLD signal is also sensitive to the acquired cardiac phase (68)because of the differences in blood volume between systolic and diastolic states. Unstable cardiac activity often leads to cardiac phase mismatch between rest and stress images, which limit accurate estimation of BOLD response between rest and stress.

- 2D methods with multiple breath holds induce patient discomfort, slice mismatch and through-plane motion.

Majority of the current BOLD imaging sequences are 2D sequence that requires multiple breath holds. However, performing multiple breath holds under vasodilating stress condition is

challenging especially for patients with CAD. The physiological response during stress can also aggravate irregular breathing and cardiac motion, which can induce slice mismatch and through-plane motion in 2D acquisitions. These effects can cause regional signal variations and reduce the reliability of BOLD exams.

- Restricted duration for imaging during vasodilator stress.

Given the inherently lower CNR, BOLD imaging is more susceptible to noise and imaging artifacts. Since peak vasodilation is typically restricted to within 4 minutes, current BOLD approaches are not suitable for acquiring images at sufficient spatial resolution and spatial coverage with desireable SNR. In addition, unlike other perfusion imaging modalities, BOLD CMR does not require monitoring the temporal dynamics of contrast agents to derive arterial input function. The intrinsic contrast of deoxygenated hemoglobin, provides a unique opportunity to perform multiple acquisitions and achieve more reliable results. However, the short acquisition windows from the conventional stress methods only utilize images at single time point and makes cardiac BOLD imaging vulnerable for failure.

A stress method that is tailored for BOLD CMR can significantly improve the imaging reliability, applicability and safety for the BOLD ischemic exam and benefit patients by realizing a truly noninvasive, non-contrast, ionizing radiation free, rendering it highlight desirable because it is reliable and safe for one or multiple ischemia testing.

This dissertation aims to overcome the current limitations in cardiac BOLD MRI so that it can become a reliable diagnostic method in the characterization of ischemic heart disease.

Chapter 3 Technical Development for BOLD CMR

3.1 Fast, Free-Breathing, 3D Whole-Heart T2 Mapping at 3T with Application of Myocardial Edema Imaging in Acute Myocardial Infarction.

3.1.1 INTRODUCTION

Over the past decade, T_2-based cardiac MRI has evolved as an important tool for characterizing myocardial tissue. To date, numerous clinical and preclinical studies have shown that hyperintensity in T_2 cardiac MRI is associated with myocardial edema, which can be used to stage myocardial infarction (69), detect myocarditis (70), acute ischemia (71) and early transplant rejection (72). Conversely, hypointensity in T_2 MRI has been instrumental in examining intramyocardial hemorrhage (73), chronic iron overloading from ferritin cardiomyopathies (74) (75) and Blood-Oxygen-Level-Dependent (BOLD) MRI (31) (76).

Early approaches typically relied on T_2-weighted imaging (T_2-STIR(69), T_2-prep-SSFP (63,77), etc.), but these approaches have well recognized image artifacts from motion, stagnant/slow moving blood and coil bias (78). As T_2 mapping techniques with high SNR readouts have overcome many of the limitations (71,79,80) and an interest in quantitative tissue characterization became viable and of clinical interest, T_2 mapping has become the preferred means for examining myocardial T_2 changes. (81,82). Nonetheless, to date, T_2 mapping is typically prescribed as 2D breath-held acquisitions to cover the full left ventricle (LV), which takes approximately 10-15 minutes. While respiratory navigator-gated approaches have

overcome the discomfort associated with multiple breath holds, the concomitant reduction in scanning efficiency has been a limitation in decreasing the overall scan time to below 10 min (83,84).

In practice, long acquisition time and multiple breath holds impose significant limitations where whole-heart T_2 mapping could be of great value. For instance, in cases where myocardial edema may serve as a marker of acute ischemia in the management of chest pain in the emergency department (85,86), target patients find it difficult to tolerate multiple breath holds and long acquisition times within the scanner. Moreover, in cases where contrast-agent free cardiac stress testing with myocardial BOLD MRI may be valuable, long acquisition times (> 6minuts) do not permit whole heart T_2 mapping within the standard duration of adenosine infusion (87). The growing interest in T_2-based cardiac MRI for both of these applications could potentially be empowered by a fast, free-breathing T_2 mapping strategy.

Moreover, most T_2 mapping approaches are limited to 1.5T and prescribed with balanced steady-state free precession (bSSFP). Their robustness to image artifacts at 3.0T (banding, B_1 inhomogeneity, etc) continues to be problematic (88). A more pragmatic cardiac T_2 mapping approach should be time efficient (preferably < 6minutes) to accommodate cardiac stress testing with BOLD MRI; enable rapid edema assessment in a clinical environment without suspending breathing; and should enable reliable acquisitions at 3T with minimal or no image artifacts, while providing full LV coverage. A T_2 mapping technique that conforms to these desirable attributes could enhance rapid assimilation of T_2 imaging as part of time-sensitive and time-efficient clinical cardiac MRI protocols.

We hypothesized that a robust, time-efficient, 3D free-breathing T_2 mapping technique at 3.0T can be obtained through the combined use of (a) adiabatic RF pulses for B_1 insensitive T_2 preparation; (b) near 100% efficient navigator gating with affine motion correction to maximize efficiency of acquisition under free-breathing; and (c) stack-of-stars gradient-echo (GRE) readouts to eliminate banding artifacts associated with bSSFP readouts, without significant loss of SNR. We validated our approach in ex-vivo canine hearts and kidneys, in healthy human volunteers, and in canines subjected to reperfused acute myocardial infarction.

3.1.2 METHODS

Pulse sequence details and data acquisition, motion estimation and correction, and parameter estimation and heart rate corrections pertaining to the proposed imaging approach are described. The motion registration program was written in C using the Insight Toolkit. Image reconstruction and parameter fitting were performed offline using MATLAB (Mathworks, R2009a, MA, USA). All studies were performed on a 3.0 T clinical MRI system (MAGNETOM Verio®, Siemens Healthcare, Erlangen, Germany) and 32 channel matrix coils (16 anterior and 16 posterior) were used for data acquisition.

3.1.2.1 Pulse Sequence Details and Data Acquisition

A T_2 prepared GRE sequence was adapted for 3D T_2 mapping at 3.0 T. To minimize image artifacts from increased B_0 and B_1 inhomogeneities at 3T (89) and cardiac motion, an adiabatic T_2 preparation (2x BIREF-1) (90) was used. A schematic of the timing diagram is shown in Fig. 3.1 and imaging parameters for each experiment are described in the following section. Images were acquired every other heart beat for longitudinal magnetization recovery.

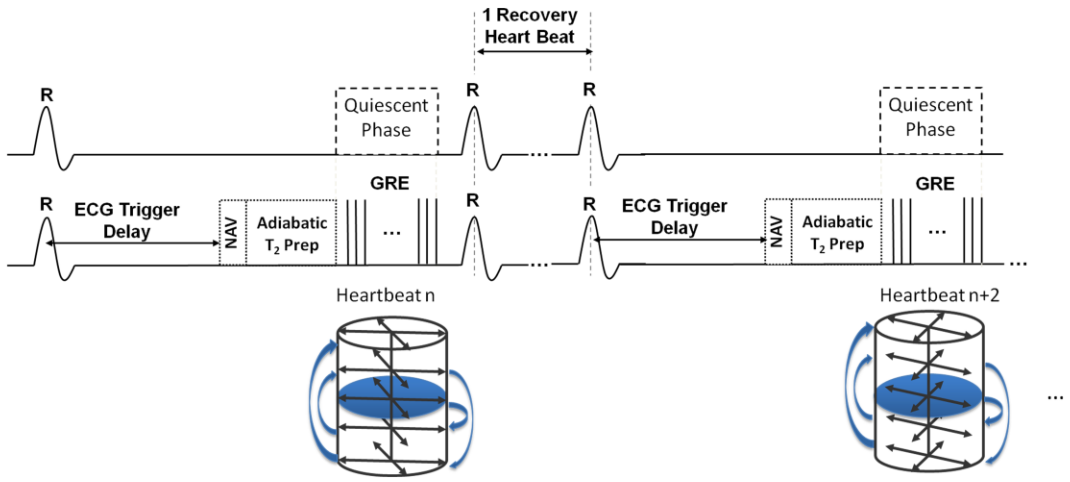

Fig. 3.1 Pulse sequence timing diagram

For the GRE readout, we used a stack of slices (along the long axis of the heart) with 144 evenly distributed radial lines to cover the 3D field of view. In each acquisition window (heart beat), a subset of 2-3 in-plane lines from all slices was acquired depending on the length of the quiescent period. In each subset, k-space lines were acquired in a slice-by-slice fashion. Centric reordering along the long axis of the heart was used to minimize T_1 recovery following T_2 preparation and the in-plane radial trajectory was ordered in an interleaved fashion to reduce the possibility of unevenly distributed data in each bin (details on bins below). For example, in a case where two in-plane radial lines A and B are acquired in each subset (A, B), the identity of the pair of radial lines conform to the sequence {(i, i+72)}, where i=1,72 and i is an integer. A representative acquisition scheme with 5 slices and 2 in-plane lines per heartbeat is shown in Fig. 3.1. GRE readout was trigged at the mid diastolic phase with appropriate trigger delay. A respiratory navigator signal at the lung-liver interface was continually acquired during the free breathing acquisitions without rejecting any data (91). The navigator module was played out before T_2

preparation to (a) avoid potential errors in binning from T_2 weighting of navigator signals at the different TEs; and (b) preserve the T_2 weighting by minimizing T_1 recovery prior to signal readout. In order to derive T_2 maps, the sequence was prescribed with three different T_2 preparation times (TE = 0, 24 and 55 ms).

3.1.2.2 Motion Estimation and Correction

Motion correction with 3D affine transforms, derived from the respiratory navigator signals, has been shown to reliably correct respiration-mediated motion of the heart (92,93). To maximize imaging efficiency (i.e., utilize all the data acquired during free breathing) the following steps were applied for motion-corrected T_2 mapping:

***Motion Estimation*:**

Binning: k-space lines were sorted into 4 bins based on the diaphragm position in which the end expiratory bin was assigned as the reference and the others were labeled as the target bins.

Data composition and respiratory phase-resolved image reconstruction: To reduce streaking artifact from undersampling of k-space, composite images were reconstructed by combining the data from all three TEs (within the same respiratory bin) followed by Gaussian smoothing. Representative images acquired at the different TEs for one of the respiratory bins and the effect of combining the images across the different TEs within the same bin are shown in Fig. 3.2A.

Motion Registration: A contour isolating the heart from rest of the anatomy was drawn manually using the 3D image set from the reference bin. The contours were then converted into a mask and applied to images in all respiratory bins. Processed 3D images from each target bin were iteratively registered to the reference bin using Insight Tool Kit (ww.itk.org) (94). Affine

transform matrices of each target bin were generated and stored for motion correction. Details of the registration process were previously described by Bhat et al (92).

Motion Correction and Image Reconstruction: k-space data in each respiratory bin were sorted back into independent TEs. After gridding, affine transform matrices were applied to the corresponding images in each respiratory bin and motion-corrected images were reconstructed independently for each TE by combining complex images from all bins. Motion estimation, correction and image reconstruction steps are summarized in Fig. 3.2B.

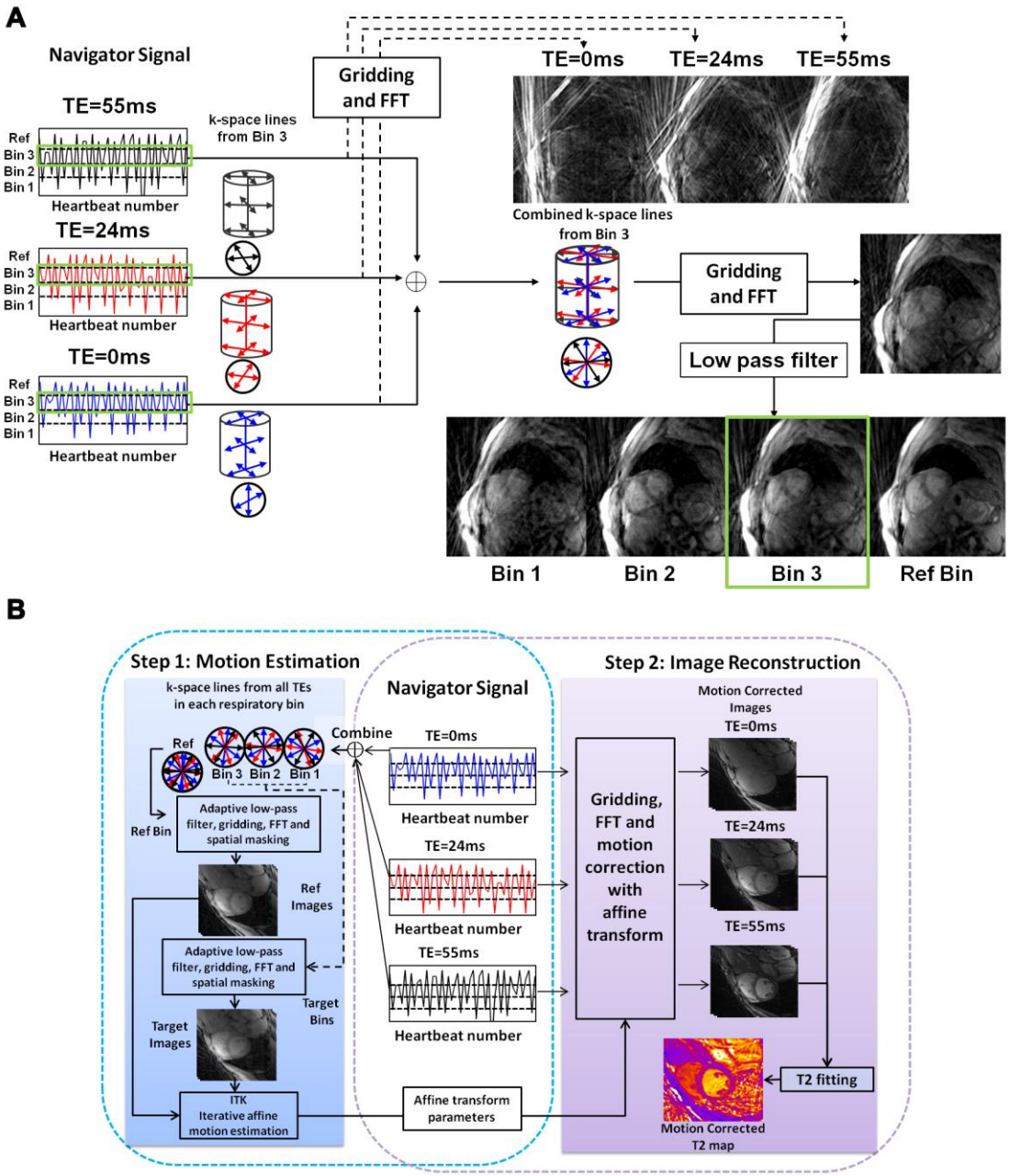

Fig. 3.2 Image reconstruction steps. Panel A shows a representative case of combining undersampled low-resolution images from a common respiratory phase from different TEs to arrive at composite data sets for each bin. This is shown for Bin 3 here. Similar steps are taken to arrive at data for Bins 1, 2 and reference bin (Ref Bin, end expiratory phase). Panel B shows the steps associated with motion correction (binning based on navigator signal, estimation of motion and image reconstruction) and parameter fitting. In essence, the k-space data is first combined with different TEs and separated into different respiratory bins based on the navigator signal. From each bin, a low-resolution composite image

representing different respiratory position was reconstructed. On the basis of the reference bin, the affine motion parameters of all other bins (target bins) were estimated with ITK and stored for motion correction. Finally, k-space data with different T_2 preparations were gridded independently and applied with corresponding affine transformation to yield motion-corrected images. Subsequently the pixel-wise fitting is performed using the images at different TEs to estimate T_2.

3.1.2.3 Parameter Fitting and Heart Rate Correction

Pixel-wise fitting of signal intensities at the 3 TEs to $a \exp(-b/\mathrm{TE})$ were performed with log-transformed linear least-squares fit , where a and b are fit parameters with $a = M_0$ (which includes proton density, coil sensitivity etc.) and $b = 1/T_2$. After the fitting for T_2, a heart rate correction was applied to compensate for imperfect T_1 recovery between magnetization preparations. To estimate true T_2, the T_2 estimates from mono-exponential fit ($T_2^{\dagger}$) were multiplied by $(1 + \alpha)$ (Refer to the heart rate correction derivation). □ was estimated from known values of T_1 (1100 ms) and T_2 (40 ms) of myocardium, data acquisition in every other heart beat, and $\Delta\mathrm{TE} = 27.5\ \mathrm{ms}\ (\text{the midpoint of TEs})$. Subsequently, heart rate corrected T_2 was calculated as $T_2^{\dagger} \cdot (1 + \alpha)$. If we estimate □ assuming T_2 = 40 ms and T_1 = 1200 ms at 3T, then the estimated errors in □ and the corresponding T_2 would be 0.08 ms and 3.2 ms (in cases of significant edema when the actual T_2 = 60 ms and T_1 = 1400 ms) (83,95).

Heart Rate Correction Derivation

In the centric encoding scheme, the longitudinal magnetization immediately following T_2 preparation of each heart beat can be written iteratively as

$$M_{T2+} = (M_0 + (M_{T2-} - M_0)E_1)\, E_{2TE}\,, \quad (1)$$

where M_{T2+} and M_{T2-} are longitudinal magnetizations following the T_2 preparations in the recent (M_{T2+}) and previous (M_{T2-}) heart beats, M_0 is magnetization at thermal equilibrium, E_1=exp(-RT/T_1) with RT = recovery time, and E_{2TE}= exp(-TE/T_2). Assuming heart rate is constant throughout the acquisition, M_{T2} term will reach a steady state after a few heart beats (i.e. $M_{T2+} = M_{T2-} = M_{T2}$) and (1) can be rearranged to get

$$M_{T2} = \frac{E_{2TE}M_0(1 - E_1)}{(1 - E_1E_{2TE})} \quad (2)$$

and the acquired signal can be expressed as

$$S_{TE} = GM_{T2} \quad (3)$$

G accounts for readout scheme, coil sensitivity, etc.

When RT >> T_1, $E_1 \sim 0$, R_2 (or $1/T_2$) can be derived with 2 measurements with different TEs using

$$\log\left(\frac{S_{TE1}}{S_{TE2}}\right) = \Delta TE\, R_2, \quad (4)$$

where $\Delta TE = TE1 - TE2$. However when RT is comparable to T_1, E_1 is not negligible and (2) has to be rewritten as

$$\log\left(\frac{S_{TE1}}{S_{TE2}}\right) = \Delta TE \cdot R_2^{\dagger}\,, \quad (5)$$

$$\text{where } R_2^{\dagger} = R_2(1 + \alpha)\,, \text{with } \alpha = \frac{\log(\frac{1 - E_1E_{2TE2}}{1 - E_1E_{2TE1}})}{R_2\Delta TE} \quad (6)$$

S_{TE1}, S_{TE2} are Image intensities corresponding to the first and second TE and αR_2 is the bias in R_2 estimated from fitting to a mono-exponential under the assumption of perfect T_1 recovery ($R_2^{\dagger}$). Hence the appropriate correction factor to estimate true T_2 is $(1 + \alpha)$; that is $T_2 = T_2^{\dagger}\ (1 + \alpha)$, where $T_2^{\dagger}$ is $1/R_2^{\dagger}$.

3.1.2.4 Validation Studies

Ex-vivo Studies

Three freshly excised canine hearts and kidneys were immersed in saline solution and imaged with the proposed method, 2D spin-echo and 2D T_2-prepared bSSFP sequences (with the same adiabatic T_2 preparation as in the proposed method) to assess T_2 accuracy. Proposed 3D sequence was prescribed covering the whole organ and 2D sequences were prescribed to match 3 separated partitions in the organs. Sequences were randomized with regard to order. Imaging parameters of the different sequences were as follows:

2D spin echo - TR = 5000 ms, TE = 6, 24, 58 ms, readout bandwidth (BW) = 300Hz/pixel and voxel size = 2.0 x 2.0 x 6.0 mm^3 interpolated to 1.0 x 1.0 x 3.0 mm^3.

Proposed 3D T_2 map - GRE readout with stack-of-stars trajectory, TR/TE = 3.4 ms/1.7 ms, flip angle (FA) = 15°, BW = 694 Hz/ pixel, 40 lines per heartbeat (simulated heart rate=60 beats/min), trigger pulse = 2, total projections = 144/slice, field-of-view (FOV) = 380x380 mm^2, matrix size =192x192x16, and voxel size = 2.0 x 2.0 x 6.0 mm^3 interpolated to 1.0 x 1.0 x 3.0 mm^3, T_2 preparation (as TEs) = 0, 24, 55ms. Gaussian apodization was used to increase SNR (96) .

2D T_2 maps with bSSFP readouts with Cartesian trajectory - TR/TE = 2.9 ms/1.1 ms, iPAT=2, partial Fourier = 3/4, FA = 35°, BW = 1184 Hz/ pixel, 86 lines per heartbeat (simulated rate 60/s), trigger pulse = 4, FOV = 288x360 mm^2, matrix size =154x192, and voxel size = 2.5 x 1.7 x 6.0 mm^3, T_2 preparation (as TEs) = 0, 24, 55ms.

3.1.2.5 Healthy Volunteer Studies

Healthy volunteers (n=10, 3 men, average age 30± 5) were recruited in accordance with the protocol that was reviewed and approved by the Institutional Review Board. Every participant was competent and provided written informed consent and had no history of coronary artery disease, abnormal cardiac rhythm and rate, kidney/liver disease, and were not contraindicated for cardiac MR exams (completed a detailed cardiac MRI questionnaire). All studies were performed on the same clinical MRI system used for ex vivo studies with subjects placed on the supine position. After whole heart shimming and localization, proposed free-breathing 3D T_2-prepared acquisitions were prescribed with whole LV coverage using 25% slice over-sampling and 32-48 radial lines per heartbeat triggered at approximately mid-diastole within a data acquisition window of 110-160 ms. A four-chamber cine scan was used to determine the quiescent period of the cardiac cycle. Navigator pulses were placed on the dome of the right hemidiaphragm. The data was reconstructed as described earlier to generate T_2 maps. For comparison purposes, images were also reconstructed without motion correction. Also, the standard 2D breath-held T_2-prepared bSSFP acquisitions were prescribed along representative short-axis slices that were matched to three slices centered at the level of mid ventricle within the 3D partitions. Imaging parameters and T_2-preparation schemes were the same as those used for

ex-vivo imaging. To minimize bias with respect to acquisition order, the acquisitions were randomized.

3.1.2.6 Canine Model of Acute Myocardial Infarction

Dogs (*n*= 10, 18–26 kg) were studied according to the protocols approved by the Institutional Animal Care and Use Committee. Animals were anesthetized, intubated and mechanically ventilated with 100% O_2 mixed with isoflurane (1.0-2.5%). Subsequently, the dogs underwent left thoracotomies and the left anterior descending artery was ligated at 1.0–1.5 cm from the bifurcation of the left main coronary artery for 3 hours followed by reperfusion. The dogs were allowed to recover for 4 days before imaging studies.

Prior to imaging, animals were fasted, sedated, anesthetized, intubated, and transferred to the scanner table and were mechanically ventilated via a pneumatic anesthesia ventilator. Subsequently, they were placed on the scanner table in the feet-first right-lateral position. The imaging protocol (localizations, cardiac shimming, and T_2-weighted acquisitions) and the scan parameters of proposed free-breathing 3D T_2-prepared acquisitions were the same as those used for the human studies except for the FOV, number of slices acquired, and acquisition window (95-140 ms) reduced to adjust for differences in cardiac dimension and heart rate. 2D breath-held T_2-prepared bSSFP acquisitions and phase-sensitive inversion recovery (PSIR) late-gadolinium-enhancement (LGE) acquisitions were prescribed with full left ventricle coverage comprising slices matched to the 3D partitions. PSIR LGE images were acquired 10 minutes after Gd-DTPA infusion (0.2 mmol/kg, gadoversetamide/Optimark, Mallinckrodt Inc., Hazelwood, MO), using non-selective inversion recovery preparation with GRE readout (TR/TE = 3.2/1.5 ms, FA = 20°, BW = 586 Hz/pixel, matrix = 96 × 192, in-plane resolution = 1.3 × 1.3 mm^2; and slice thickness

= 6.0 mm). A TI-scout sequence was used to find the optimal TI for nulling the healthy myocardium (240–270 ms).

3.1.2.7 Image Analysis and Statistics

All reconstructed T_2 maps were analyzed in cvi[42] (Circle Cardiovascular Imaging Inc., Calgary, AB, Canada). Images were imported into cvi[42] and endo- and epi-cardial contours were drawn to segment the myocardium for further T_2 analysis. In addition, all statistical analyses were performed in IBM SPSS (V21.0, NY, USA).

***Ex vivo Studies*:**

After segmenting the myocardium and parenchyma of the kidney, mean T_2 values of the organs determined from images acquired using 2D spin echo, 2D T_2-prepared bSSFP and 3D T_2-prepared (proposed) sequences were compared. Repeated measurements ANOVA tests were performed to examine whether the T_2 values were different between different sequences. Post-hoc comparison with Bonferroni correction was used if the null hypothesis was rejected.

***Human Studies*:**

The mean and coefficient-of-variation (COV) of myocardial T_2, as well as overall image quality scores of the T_2 maps generated using images from the (i) proposed 3D sequence with motion correction (3D FB MoCo), (ii) proposed 3D sequence without motion correction (3D FB Non-MoCo, using all respiratory phases), and (iii) 2D breath-held sequence (2D BH) were measured. Two independent, experienced observers who were blinded to the acquisition details evaluated image quality. All image quality assessments were based on the T_2 maps. Mean myocardial T_2 values were measured from the segmented myocardium and the COV of T_2 was calculated as the

quotient of the mean T_2 and the corresponding standard deviation. Image quality was graded as 1, poor (non assessable); 2, fair (mild to moderate artifacts); 3, good (minimal to mild artifacts); 4, excellent (minimal or no artifacts). Repeated measurements ANOVA tests (mean T_2 and COV in T_2) and Friedman test (image quality scores) were performed to examine whether the measures were different between the three techniques. Post-hoc comparison with Bonferroni correction was used if the null hypothesis was rejected.

***Canine Studies*:**

Following segmentation of the myocardium (as described earlier), remote myocardium was defined as the region showing no hyperintensity on LGE images. A reference region of interest was drawn in remote myocardium on both LGE images and copied onto the corresponding slice positions of 2D and 3D T_2 maps. Affected myocardium was defined as the hyperintense region with mean signal intensity at least 2 standard deviations (SDs) above that of the reference region of interest on both 2D and 3D T_2 maps (79). Only LGE positive imaging slices were included in the analysis. Regression analysis was performed between slice-matched 2D and 3D acquisitions for (a) mean T_2 values of remote and affected (edematous) myocardium; and (b) % edema volume, defined as the relative volume of affected myocardium to the total volume of the myocardium on a per-slice basis, for all animals. Bland-Altman analysis was performed to examine the limits of agreement and bias in mean T_2 and % edema volume between the proposed 3D approach and the 2D approach.

3.1.3 RESULTS

3.1.3.1 Ex vivo Studies

Representative T_2 maps obtained using 2D spin-echo and T_2-prep bSSFP acquisitions along with the proposed 3D acquisition (matched to the 2D slice) are shown in Fig. 3.3A. Mean T_2 values derived from each sequences are shown in Fig. 3.3B (2D spin-echo T_2 = 40.8±2.4 ms (heart), 52.4±0.5 ms (kidney) ms; 2D T_2-prep bSSFP T_2 = 42.4±1.6 (heart), 52.9±1.1 (kidney) ms; and proposed 3D sequence T_2 = 40.2±2.5 (Heart), 51.3±0.7 (kidney) ms). Relative to the "gold standard" T_2 values (2D spin-echo), T_2 values obtained with 2D T_2-prep bSSFP and 3D T_2-prep GRE were not different ($p = 0.7$ and $p=0.2$, respectively).

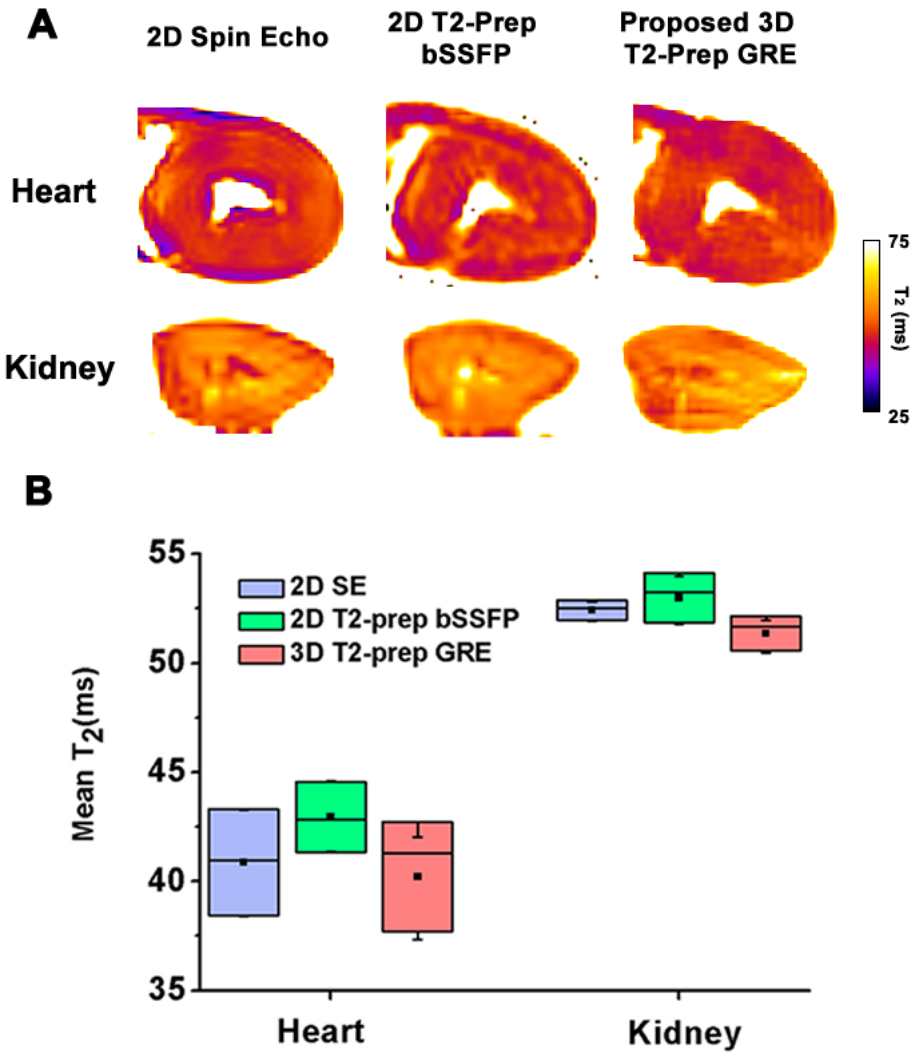

Fig. 3.3 Representative short-axis T_2 maps and box-plot of mean myocardial T_2 from explanted pig hearts obtained with 2D spin echo, 2D T_2-prep SSFP and 3D T_2-prep GRE acquisitions. (A)Slice-matched T_2 maps obtained at the level of mid ventricle from an explanted pig heart using the different T_2 approaches are shown. Mean T_2 values (B) between the approaches were not different.

3.1.3.2 Healthy Volunteers

Figure 3.4 shows representative slice-matched T_2-weighted images (Fig. 3.4A) and T_2 maps (Fig. 3.4B) obtained using 3D FB MoCo, 3D FB Non-MoCo, and 2D BH approaches. 2D BH and 3D FB MoCo images at the different TEs appeared to have comparable image quality, while image blurring from respiratory motion was evident in 3D FB Non-MoCo images and maps (arrows).

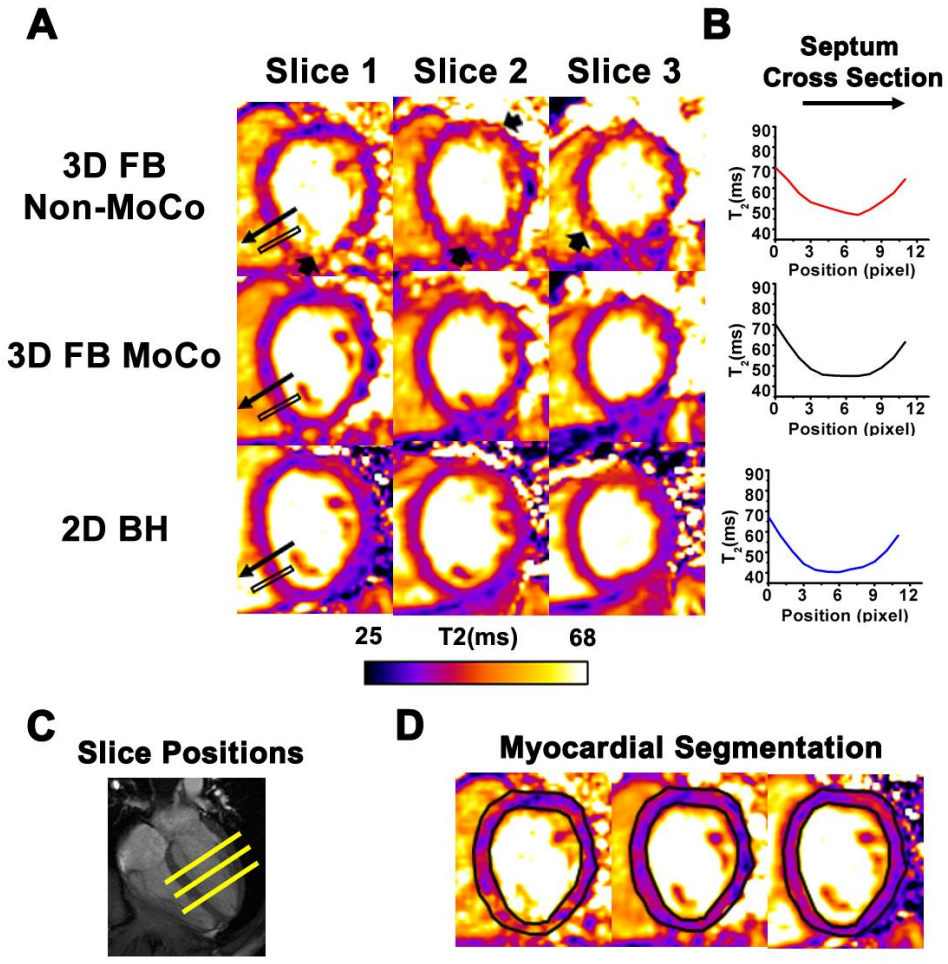

Fig. 3.4 Representative short-axis images and T_2 maps acquired from a healthy volunteer using 2D BH, 3D FB MoCo and 3D FB Non-MoCo approaches. T_2 maps reconstructed using weighted images from the different TEs at the basal, mid ventricle (Mid) and apical sections are shown. Note the loss of detail and variation in signal intensity in 3D FB Non-MoCo images (arrows), which is absent in 3D FB MoCo and 2D BH T_2 maps.

Quantitative measures of agreement between the methods are shown in Fig. 3.5 and collected in Table 1. 3D FB Non-MoCo showed significantly greater COV ($p<0.05$), longer T_2 values ($p<0.05$), and lower IQ ($p<0.05$) compared to 3D FB MoCo and 2D BH images and maps. Conversely, 2D BH and 3D FB MoCo approaches did not show differences in mean T_2 ($p=0.99$), COV T_2 ($p=0.74$), and IQ ($p=0.14$).

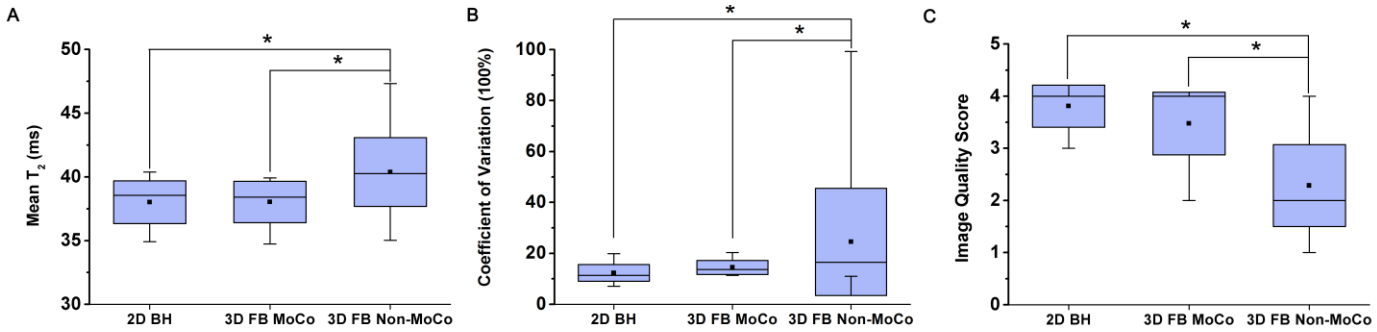

Fig. 3.5 Quantitative measures of mean T2 (A), COV T2 (B) and Image Quality scores (C) between 2D BH, 3D FB MoCo and 3D FB Non-MoCo approaches obtained from healthy volunteers. Across all measures, 2D BH and 3D FB MoCo approaches were not different but both were significantly different (represents p<0.05) from 3D FB Non-MoCo approach.*

3.1.3.3 Canines with Reperfused Acute Myocardial Infarction

Representative slice-matched images (Fig. 3.6A) and T_2-maps (Fig. 3.6B) obtained with the proposed 3D FB MoCo and 2D BH obtained on day 4 post-MI are shown. Corresponding LGE images are also shown for visual confirmation for the presence of infarction in the LAD territory. Edema (and infarction) was identified in 2-4 short-axis slices in each of the animals. Close correspondence between edematous territories in the slice-matched 2D BH and 3D FB T_2 maps, and the enhanced territories in LGE images was observed. T_2 values were significantly elevated in regions positive for LGE in both 2D BH and 3D FB T_2 maps. Linear regression analysis showed that the T_2 estimates (edematous and remote territories) and the % edema volume

measured from 2D BH and 3D FB MoCo T_2 maps were closely correlated (R^2 = 0.88,and 0.96, respectively. Both $p<0.05$). Bland-Altman plots of mean T_2 measures from edematous territories and remote myocardium and % Edema Volume were within the limits of agreement (bias in T_2 = 0.4 ms; bias in % Edema Volume = 0.9%). The edema and LGE positive territories (on per slices basis) agreed well (R^2 = 0.8, $p<0.05$) with the edema volume have a positive bias of 8% over LGE volume.

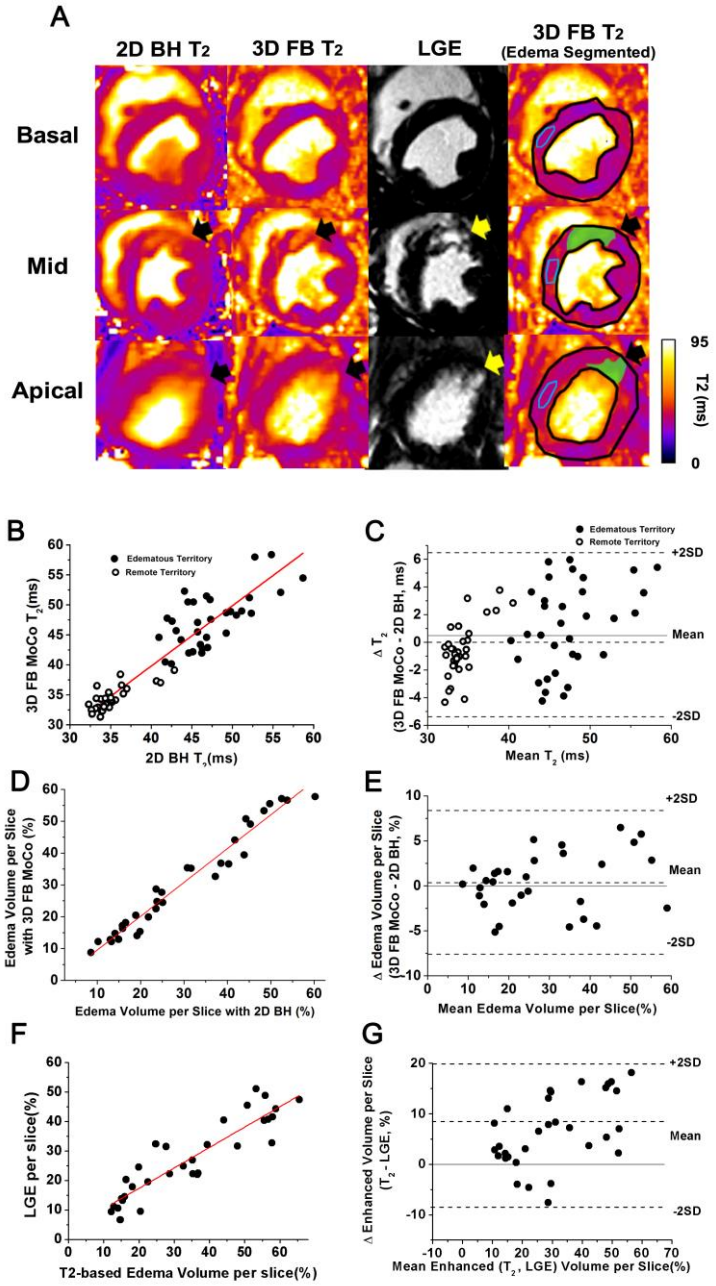

Fig. 3.6 Representative short-axis images obtained from a canine on day 4 post-MI and the statistical relations between 2D BH and 3D MoCo for T2 and Edema volume across all animals. (A) Slice-matched T2 maps from 2D BH and 3D FB MoCo, as well as LGE images obtained from a canine at the basal, mid ventricle (Mid) and apical sections are shown. Note the close correspondence between hyperintense

regions identified on 2D BH and 3D FB MoCo T2 maps (black arrows) and their relation to hyperintense regions in LGE images (yellow arrows). Also note that the 2D BH images are blurrier due to cardiac motion (due to single-shot acquisitions in the presence of high heart rates in canines with recent infarction), which is not the case with the proposed approach. (B) Linear regression analysis between T2 values (edematous territories and remote myocardium) of slice-matched 3D FB MoCo and 2D BH acquisitions and the corresponding Bland-Altman analysis are shown in panels B and C, respectively. Linear regression: y = 0.9 x – 3.4, where y = T2 from 3D FB MoCo and x = T2 from 2D BH acquisitions, with R2 = 0.88, p<0.05. Linear regression analysis between slice-matched 3D FB MoCo and 2D BH acquisitions for Edema volume and the corresponding Bland-Altman analysis are shown in panels D and E, respectively. Linear regression: y1 = 1.1 x1 -2.4, where y1 = Edema volume from 3D FB MoCo and x1 = Edema volume from 2D BH acquisitions, with R2 = 0.96, p<0.05.

3.1.4 DISCUSSION

In this study we successfully developed and tested a motion-corrected, free-breathing 3D T_2 mapping technique using GRE-based stack-of-stars acquisition at 3T that can be completed within 5 minutes. The accuracy of T_2 measures from motion-corrected reconstruction was examined in ex-vivo canine hearts and kidneys, healthy human volunteers, and controlled canine model of acute myocardial infarction, respectively. The results showed that compared to the commonly used T_2 mapping approach (2D acquisitions with multiple breath holds), the proposed 3D T_2 mapping strategy can reliably estimate T_2 values of the myocardium in health and disease. The proposed method is expected to be beneficial in patients who cannot tolerate suspension of breathing and in cases where the imaging exam needs to be completed with whole heart coverage within a short period of time. Hence the key features of the proposed approach (free-breathing, full LV coverage coverage and fast acquisitions) are expected to be particularly valuable in the management of chest pain in emergency department where myocardial edema may be used as a marker of ongoing ischemia (71) and for contrast-free cardiac stress testing using myocardial BOLD MRI(31,76) .

While the benefits of fast, free-breathing T_2 mapping of whole LV over the conventional multiple-breath-held T_2 mapping are clear, it is useful to contrast the proposed approach against previously proposed 3D T_2 mapping approaches. While navigator gated methods have shown low imaging efficiency and residual motion artifacts, different methods have been proposed to correct for respiratory motion and accelerate acquisition(83,97). In particular, the recent development by Heeswijk, et al.(97) has markedly reduced acquisition time. However, since their T_2 mapping approach is founded upon 3D high-resolution isotropic imaging, acquisition time continues to be near 20 minutes, which imposes limitations on its use for time sensitive applications discussed above.

In this study we utilized a 3D stack-of-stars sampling scheme for T_2 mapping, which lends some key benefits. First, at a heart rate of 60 beats/minute, with 48 projections acquired every other heartbeat, the total acquisition time for whole LV coverage is less than 5 minutes. Since the proposed approach does not restrict one to isotropic resolution, it provides the flexibility to control the resolution along the long axis, and hence imaging time, depending on the needs of the study. Second, the proposed approach allows for centric encoding, which reduces the T_1 dependency in T_2 maps (83). Finally, the proposed T_2 mapping strategy offers robust image quality at 3T since the proposed approach uses adiabatic T_2 preparation combined with GRE readouts to overcome image artifacts from B_1 and B_0 inhomogeneities at 3T. Although bSSFP readouts can provide significant signal-to-noise benefits over GRE, previous studies have shown insignificant differences in myocardial T_2 between the two readout sequences at 1.5T (98). Consistent with these studies, in the current study at 3T we observed comparable COV in myocardial T_2 between bSSFP and GRE readout schemes. Nonetheless both readout schemes have their limitations in extreme cases - GRE acquisitions can suffer from lower SNR and have

less homogeneous signal in large patients; and bSSFP readouts are prone to unavoidable banding artifacts.

The T_2 values measured under conditions of health in this study were comparable to the values previously reported in humans. Specifically, we found that the T_2 value of the healthy myocardium to be 37.7±2.0 ms vs. 38.5 ± 4.5 ms (83). Similar observations were made in animals with acute myocardial infarction as well (T_2 in the infarct zone from our study was 55.2±7.1 ms vs. 58.1 ± 6.9 ms (99) and T_2 in remote zone from our study was 36.7±3.5 ms vs. 41.1 ± 5.2 ms (99)). These favorable comparisons between our results and those reported in the literature further confirm that the proposed technique is a reliable method for measuring myocardial T_2 under conditions of health and disease.

Although not explored here, we anticipate that further shortening of scan time may be possible using parallel imaging techniques (100,101) and/or compressed sensing (102) schemes. However, to avoid potential "smoothing" artifacts observed in certain accelerated approaches and also to strictly examine the capability of motion correction, we did not consider any imaging acceleration techniques in the current study. Additional studies are necessary to examine the limits of imaging acceleration strategies within the constraints of reliable measurements of myocardial T_2.

There were some limitations in this study. First, while this study employed ex-vivo and in-vivo preparations of animals and healthy volunteers and showed that the proposed 3D approach can yield similar values of T_2 as 2D breath-held acquisitions, the sample size of the study is limited. Additional studies are required to assess the robustness of the method under various physiological conditions, particularly in human subjects with disease. Second, based on the

mono exponential model, 3 TEs are the minimum requirement for a least-squares linear-regression fitting of the logarithmically transformed data. To map the T_2 of the remote and affected myocardium, we set the latest TE to be 55ms, so as to achieve a reasonable dynamic range in signal intensities for the affected territory (which tends to have T_2~ 60ms) and still have sufficient in the remote myocardium (T_2 ~ 40 ms). Although additional TEs may improve robustness of T_2 fits **(103),** extra acquisition time associated with greater number of TEs can extend the study time beyond the demands of the key applications outlined earlier. Based on comparable results we obtained here in relation to past work (72,79,80,83,104), we expect that three TEs to be a good tradeoff between imaging speed and fidelity of myocardial T_2 fits under conditions of health and disease. Third, in this study we assumed that the prescribed slice positions between 2D and 3D acquisition are the same, which may not be the case. To minimize this error, the data in the reference bin was always acquired at end expiration. Also, given that 2D slice thickness and 3D partitions are similar (6 mm), we anticipate that any contributions from potential differences to be small. Moreover, we used only 4 bins to derive and correct for respiration-induced motion. Previous studies that employed affine motion correction on the raw data (92,105) used 6 bins to estimate respiration-mediated motion for coronary MR angiography. Finally, we estimated the correction term (□) based on known T_1 and T_2 values of the myocardium at 3T in health. Since T_1 and T_2 of the edematous myocardium can be greater than 30% and 50% of the normal myocardium (83,95), respectively, it is conceivable that α may not be accurately estimated on the basis of healthy myocardial T_1 and T_2 values. However, our calculations showed that even in the presence of significant edema (T_1 =1400ms, T_2=60ms), the estimated error in α determined using healthy T_1=1200ms and T_2=40ms values is within 8%,

which corresponds to a deviation in T_2 of 3.2 ms, which is comparable to the standard deviation of myocardial T_2.

Nonetheless, the results here suggest that the quality of motion correction based on the empirical binning at reduced resolution is adequate for reliable estimation of myocardial T_2 values under conditions of health and disease.

3.1.5 CONCLUSION

We developed and tested a free-breathing 3D T_2 mapping approach at 3T with respiratory motion correction, which can be performed within 5 minutes. The proposed approach yielded accurate estimates of myocardial T_2 in explanted canine hearts and kidneys, healthy human volunteers, and canines with reperfused acute myocardial infarction. Clinical studies are needed to validate the robustness of the proposed approach in patients.

3.2 Fast, Confounder-Corrected, Quantitative BOLD CMR at 3T with Simultaneous ^{13}N-Ammonia PET Validation in Canines

3.2.1 INTRODUCTION

Detection of impaired myocardial perfusion reserve is valuable in the clinical management of coronary artery disease (CAD) (106). While SPECT/PET imaging methods are the established standards for determining myocardial perfusion, the requisite need for ionizing radiation with these approaches have long instilled a desire for an alternate method that can be performed

without subjecting patients suspected of CAD to ionizing radiation. To this end, first-pass perfusion methods, particularly comprising of recent technical advances (107), have provided compelling evidence that it is possible to evaluate myocardial perfusion without radiotracers. However, first-pass perfusion requires gadolinium-based contrast agents, which is contraindicated in patients with late-stage chronic kidney disease. Moreover, there is a growing concern that GBCA can lead to chronic deposition of gadolinium within the myelin sheaths with unknown outcomes even in patients without renal insufficiency. Enabled by nearly two decades of technical advancements, growing body of clinical evidence now supports the notion that blood-oxygen-level-dependent CMR, a method which can aid in the assessment of myocardial perfusion without radiation and exogenous contrast agents, can be used to assess myocardial perfusion on the basis of differential changes in oxygen saturation between rest and vasodilator stress (18-20,76,108). Nonetheless further refinements of the BOLD CMR approach are necessary as the currently available variants are limited by (a) limited imaging speed and coverage to accommodate the stress protocols; (b) loss in BOLD sensitivity due to imaging confounders (T1 weighing, coil bias and heart rate dependency); (c) patient discomfort and inaccurate slice match between rest and stress from 2D acquisitions requiring multiple breath holds; and/or (d) imaging artifacts (cardiac and respiratory motion; B0 and B1 field inhomogeneity) particularly at 3T, where the myocardial BOLD sensitivity has been shown to be superior to that at 1.5T. These limitations can compromise diagnostic sensitivity of BOLD CMR resulting in inaccurate interpretation of myocardial perfusion between rest and stress.

To address these limitations, we developed a heart-rate independent, free-breathing 3D T2 mapping technique at 3T, which can be acquired with marked insensitivity to B0 and B1 inhomogeneities, along with near perfect imaging efficiency, to facilitate imaging coverage of

whole LV within 4 minutes. The proposed BOLD CMR approach was developed, tested and validated through computer simulations, ex-vivo studies, and in-vivo studies in canines with and without coronary stenosis with simultaneous acquisition of BOLD CMR and ^{13}N-ammonia PET in a clinical hybrid PET/MR system. A feasibility study was also performed to evaluate the capability of the proposed approach for examining myocardial BOLD response throughout the whole LV within the clinically accepted window of adenosine vasodilator stress in healthy human volunteers.

3.2.2 METHODS

All ex-vivo and in-vivo imaging studies in canines were performed in a whole-body PET/MR system (Biograph mMR, Siemens Healthcare, Erlangen, Germany). Human studies were performed in a 3T MRI system (Verio, Siemens Healthcare, Erlangen, Germany), which has similar MR imaging capabilities as the PET/MR system.

3.2.2.1 CMR Pulse Sequence Design and Motion-Corrected T2 Mapping with Near-Perfect Imaging Efficiency

An ECG-gated, heart-rate independent, free-breathing, 3D T2 mapping approach with whole-heart LV coverage, which minimizes the sensitivity to B0 and B1 inhomogeneities was implemented the PET/MR system. Adiabatic T2 preparation with spoiled gradient-echo (GRE) readout was used to minimize B0 and B1 artifacts, which are otherwise prominent at 3T(83). To improve imaging efficiency and enable data acquisition under free-breathing conditions, a motion correction platform with a hybrid Cartesian-radial trajectory was applied(109) that

permits near perfect imaging efficiency was used. To further increase acquisition speed and minimize the signal dependence on heart rate between rest and stress, a Saturation Recovery (SR) preparation was integrated with a constant saturation recovery time (T_{SR}) time to reset longitudinal magnetization every heartbeat (110). To minimize any potential confounding effects associated with differences in T1 recovery following T2 preparation under rest and stress (111), data was collected and centrically encoded in the through-plane direction. Images were acquired with 3 incremental T2-prepation times (TE=0, 24, 55ms) and T2 maps were reconstructed using a custom-written Matlab (The Mathworks, Natick, Massachusetts) script. Sequence diagram and reconstruction flowchart are shown in Figure 3.7.

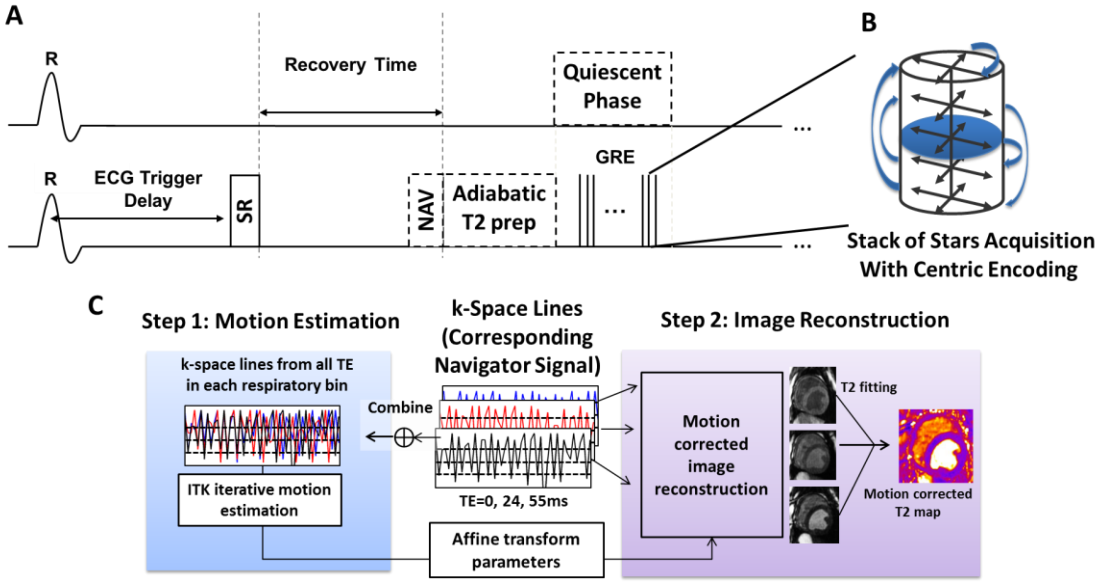

Fig. 3.7: Heart-Rate Independent 3D T2 Mapping Based BOLD CMR: Timing diagram, data acquisition and motion-corrected image reconstruction. The timing diagram and data encoding strategy are illustrated in Panels A and B. In Panel A, a standard T2 preparation scheme was replaced with a T2 preparation scheme composed of composite adiabatic RF pulses and spoiled gradient echo readout (in place of the typical balanced steady-state free precession readout) to minimize B1 and B0 artifacts at 3T. A SR preparation was added to eliminate the signal dependence on heart rate between segmented readouts and navigator pulses were added to monitor the respiratory motion during acquisition. Panel B

shows the centric encoding scheme with hybrid trajectory, to ensure optimal T2 weighting. The sequence was designed to permit T2 mapping with 3 different T2 preparation times for T2 fitting. Panel C shows the motion correction algorithm used (109). Raw data with different T2 weightings are first combined and binned based on the navigator signal to generate anatomical images from different respiratory phases. The respiratory motion is estimated from the anatomical images and applied to the raw data to reconstruct motion-corrected T2 maps using a log-transformed linear least-squares fit as previously described used (109).

Raw data acquired during free breathing was separated into 4 respiratory bins with the navigator signal to estimate respiratory motion. Data acquired from all TEs (in each bin) was combined to generate composite anatomical images and reduce the streaking artifact from under-sampling. Corresponding affine transform parameters from each respiratory bin were estimated using iterative registration of the composite images. These motion estimates were applied to data in each bin and motion-corrected images were reconstructed with different TEs. The signal intensities from the images were fitted pixel-wise to a mono-exponential model to derive motion corrected T2 values. The proposed sequence is designed to acquire a 2x2x6 mm^3 3D whole heart images under 4 minutes.

Computer Simulations and Ex-vivo study

Computer simulations employing Bloch equations (112), with parameters corresponding to commercially available 2D T2 mapping sequence and the proposed 3D T2 mapping approach, with and without SR preparation were performed to assess the dependence of heart rate on T2. Simulation parameters included myocardial relaxation times T2 = 47.5 ms and T1 = 1157 ms (104)at 3 T. The transverse magnetization (Mxy) of the center of the k-space was used as the image contrast for each image and was fitted for quantitative T2.

To validate the simulation findings and to experimentally determine the influence of heart rate on T2 maps, freshly excised canine hearts (n=3) were immersed in saline solution and individually scanned using a head coil with i) a commercially available 2D T2 mapping sequence(84), ii) the proposed 3D method *without* SR preparation and iii) proposed 3D sequence (which includes SR preparation) by artificially imposing heart rates of 40 – 110 beats/min (bpm) in increments of 10 bpm. 3D sequences were prescribed with full LV coverage and 2D sequences were prescribed to the matched 3D partitions. Heart rates were chosen to capture the typically observed heart rate changes between conditions of rest and adenosine stress (113). To minimize bias, prescription the order of the sequences were randomized. Details of the sequences are provided as the following:

BOLD CMR Imaging Parameters

Proposed 3D T_2 map: GRE readout with stack-of-stars trajectory, TR/TE = 3.0 ms/1.5 ms, flip angle (FA) = 15°, BW = 1100 Hz/ pixel, 32 lines per heartbeat, trigger pulse = 1, total projections = 144/slice, field-of-view (FOV) = 380x380x84 mm^3, with 14% slice oversampling, matrix size =192x192x16, and voxel size = 2.0 x 2.0 x 6.0 mm^3 interpolated to 1.0 x 1.0 x 3.0 mm^3, T_2 preparation (as TEs) = 0, 24, 55ms, SR recovery time= 130ms. Gaussian apodization was used to increase SNR (114) .

2D T_2 maps with bSSFP readouts with Cartesian trajectory: TR/TE = 2.9 ms/1.1 ms, iPAT=2, partial Fourier = 3/4, FA = 35°, BW = 1184 Hz/ pixel, 86 lines per heartbeat (simulated rate 60/s), trigger pulse = 5, FOV = 288x360 mm^2, matrix size =154x192, and voxel size = 2.5 x 1.7 x 6.0 mm^3, T_2 preparation (as TEs) = 0, 24, 55ms.

Cine bSSFP: Cine acquisitions were prescribed in short-axis before stenosis induction and post stenosis dispensation with the scan parameters: TR/TE = 3.0/1.5 ms, FA = 50°, BW = 1300

Hz/pixel, matrix = 96 × 192, in-plane resolution = 1.9 × 2.5 mm^2; slice thickness = 6.0 mm; and 2 fold tGRAPA).

LGE: Phase-sensitive inversion recovery (PSIR) late-gadolinium-enhancement (LGE) acquisitions were prescribed rule out infarctions. PSIR LGE images were acquired 10 minutes after Gd-DTPA infusion (0.2 mmol/kg, gadoversetamide/Optimark, Mallinckrodt Inc., Hazelwood, MO), using non-selective inversion recovery preparation with GRE readout (TR/TE = 3.2/1.5 ms, FA = 20°, BW = 586 Hz/pixel, matrix = 96 × 192, in-plane resolution = 1.3 × 1.3 mm^2; and slice thickness = 6.0 mm). A TI-scout sequence was used to find the optimal TI for nulling the healthy myocardium (240–270 ms).

3.2.2.2 Validation Studies in Animals: BOLD CMR with Simultaneous ^{13}N Ammonia PET

Animal Model & Preparation:

Two groups of dogs were studied: (a) Healthy animals (*Group Intact*, n=10) and (b) animals with coronary stenosis (*Group Stenosis*, n=10). For the stenosis studies, animals were implanted with occluders to artifically induce LAD stenosis, as previously described(45). Prior to imaging, animals were fasted (18 hours), sedated, anesthetized with propofol (2.0-5.0 mg/kg,IV), intubated, moved to the scanner table and ventilated (Model 2002 Halowell EMC, MA, USA). ECG, heart rate and blood pressure were monitored throughout the studies. Anesthesia was maintained with a continuous infusion of low-dose propofol (0.03-0.1 mg/kg/min, IV) during imaging to minimize confounding effects of anesthesia on the heart. In *Group Stenosis*, imaging was performed after establishing non-flow limiting stenosis at rest (absence of visually evident ST-elevation at rest). Moreover, cine CMR was acquired to ensure that following the release of the LAD stenosis, wall motion abnormalities or edema (115) were absent. All studies were

terminated with LGE CMR to rule out myocardial infarction. Imaging parameters are presented as the following:

Imaging Protocols:

In all studies, ^{13}N-ammonia PET and BOLD CMR images were acquired simultaneously in the same scanner. PET images were acquired in 3-dimensional (3D) list mode using ^{13}N-ammonia (200 MBq, IV bolus (3-5 s) followed by 10 cc saline flush) as the blood flow tracer. Prior to each PET scan, anatomical MR images were acquired to correct for photon attenuation. Attenuation correction was performed using segmentation of images obtained with a 2-point Dixon MR imaging pulse sequence, which has been shown to be effective for cardiac studies(116,117). Data acquisition spanned over 10 minutes and began a few seconds before the ^{13}N-ammonia injection. A time delay was introduced between the sequential PET acquisitions at each physiological condition to ensure sufficient decay of each ^{13}N-ammonia dose (5 half lives, ~50 minutes). BOLD CMR images were acquired with the proposed 3D sequence under each physiological condition immediately after the ^{13}N-ammonia injection. BOLD images were acquired with the same parameters described in the ex-vivo studies. 3D whole-heart BOLD images were consistently acquired within 4 minutes depending on the heart rate. To investigate the influence of HR on BOLD sensitivity, conventional 2D T2 mapping was performed on a single mid-ventricular slice in the intact animals and was randomized with respect to the acquisition order (i.e., before or after 3D acquisitions). In *Group Intact*, images were acquired during adenosine infusion (140 μg/kg/min, IV) and at rest to investigate the Myocardial Perfusion Reserve (MPR) and Myocardial BOLD Response (MBR). Specifically, under adenosine, image acquisitions were prescribed following 2 minutes of adenosine infusion. In *Group Stenosis*, images were acquired at rest and under adenosine after inducing LAD coronary

stenosis. Other aspects of the imaging protocol implemented in *Group Stenosis* were similar to that implemented in *Group Intact.* A schematic representation of the sequential execution of the study protocols is provided in Figure3.8. All stenosis scans were terminated with late gadolinium enhancement (LGE) imaging to rule out infarctions. Once the imaging studies were completed, animals were euthanized.

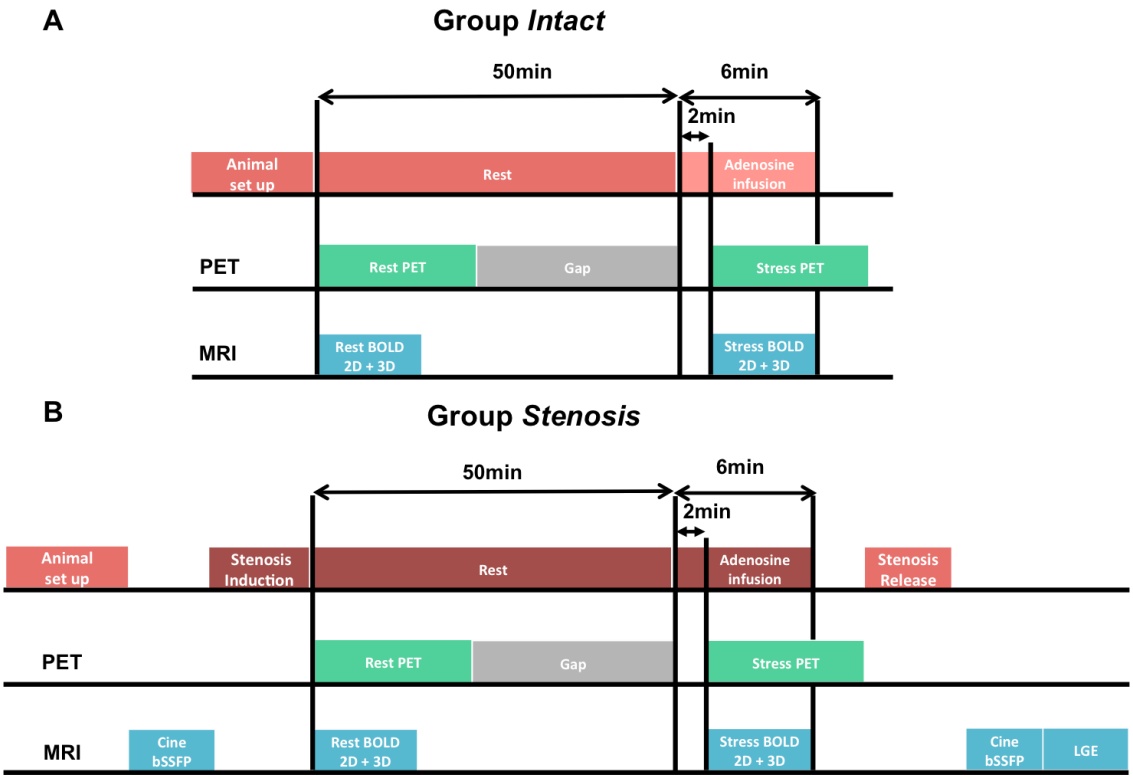

Fig. 3.8 Chronological order of image acquisition in Group intact (A), and Group Stenosis (B). In all studies, simultaneous PET and BOLD CMR images were acquired under rest and stress with an at least 50 minutes separation to avoid isotope cross talk. In group stenosis, Cine images were acquired before the stenosis induction and following the release of the stenosis to probe the motion abnormality and signal elevation and rule out myocardial edema. LGE images were also acquired after cine images to rule out myocardial infarction.

3.2.2.3 Whole Heart BOLD Response in Healthy Human Subjects During Adenosine-Mediated Coronary Vasodilatation: A Feasibility Study

10 Healthy volunteers (7 men, average age 35± 8) without any history of CAD and other cardiovascular abnormality were recruited in accordance with the protocol that was reviewed and approved by the Institutional Review Board of Cedars-Sinai Medical Center. Subjects were placed in the supine position, and after scouting and whole heart shimming, proposed sequence was prescribed under rest and 2 minutes after the start of adenosine infusion (140 μg/kg/min, IV; total infusion time 6 minutes). Imaging parameters, including the SR and T_2-preparation schemes, were the same as those used for animal studies. In subjects with significant fat deposition, water excitation pulses were used to suppress fat signal (118).

Image Analysis

All CMR images were analyzed with ImageJ (version 1.46, NIH, Bethesda, MA, USA).

Ex-vivo Images

Regions of interest (ROIs) drawn within the myocardium of mid ventricular slices (Figure 3.9A) were used to measure T2 from images acquired with the different sequences under variable heart rates. Mean T2 values at the various heart rates were used as the dependence of T2 on heart rate.

Ammonia PET

All ^{13}N-ammonia PET images were processed by an experienced technologist as previously described (119). Myocardial perfusion (in units of ml/min/g) and Myocardial Perfusion Reserve (MPR) were quantified automatically from the PET data using the automated QPET software (Cedars-Sinai Medical Center, Los Angeles, CA, USA) (119). In *Group Stenosis*, myocardial segments with perfusion defects were identified on the basis of stress-rest change analysis in

QPET software (119,120). The segments identified with perfusion deficit were labeled as 'Affected' and those without perfusion defects were labeled as 'Remote' segments.

BOLD CMR

Epicardial and endocardial contours were traced on T2 maps to delineate the myocardium and were subsequently segmented according to the AHA 16-segment model. Mean myocardial T2 values under rest and stress were measured for each segment. *Myocardial BOLD responses (MBR)*, defined as T2 at stress normalized by the T2 at rest ($MBR = T_2^{Stress}/T_2^{Rest}$) for each segment was computed. This was determined in both group of animals (*Intact* and *Stenosis*) and compared against segmental MPR from ^{13}N-ammonia PET. In *Group Intact*, MBRs were computed from the T2 maps of mid-ventricular slices acquired using proposed (MBR_{Porp}) matched to the conventional 2D T2 maps (MBR_{Conv}). To determine the influence of heart rate fluctuations between rest and stress ($\Delta HR = HR^{Stress} - MBR^{Rest}$) on BOLD contrast was computed as *Loss of Apparent MBR* = 100% x *(*$MBR_{Prop} - MBR_{Conv}$) and regressed against □HR. For stenosis studies, MBR of the affected segments (identified on the basis of ^{13}N-ammonia PET analysis (119,120)) were compared against the MPR of the remote segments. A similar analysis was performed in human subjects to determine MBR.

Statistical Analysis

For ex-vivo studies, the conventional 2D T2 maps at HR= 60 bpm were labeled as baseline. T2 measurements at different fixed heart rates were compared to the baseline values using two-way measurements ANOVA for each sequence. A *post-hoc* comparison with Bonferroni correction was used if the null hypothesis was rejected. For the intact animal studies, paired student's t-tests were used to compare myocardial perfusion and myocardial T2 values between rest and stress.

Linear mixed models were used to examine data trends between the MBR and MPR. Linear regression between *Loss of Apparent BOLD Contrast* and ΔHR was performed to investigate the influence of heart rate changes on BOLD response. For the stenosis studies, MPR from the Affected and Remote segments from all animals were compared using student's t-test with Bonferroni correction. The same test was used to examine the difference in the simultaneously acquired MBR. In human studies, segmental T2 values between rest and stress were compared using a paired student's-t test; and a student's t test was use to test whether MBR> 1. All values are reported as mean ± SD (unless stated otherwise) and statistical significance was established for $p<0.05$. All statistical analysis was performed in IBM SPSS (V21.0, NY, USA).

3.2.3 RESULTS

3.2.3.1 Computer Simulations and Ex-vivo Study

Figure 3.9 shows the results from computer simulations and the ex-vivo studies. Simulated and experimental mean myocardial T2 measured under artificially modulated heart rates are compared in panel A. Simulations showed a clear trend of decreasing T2 values with increasing heart rates, which was not evident with the proposed sequence. Experimental T2 values measured from ROIs placed within the mid-ventricular slices (Fig. 3.9B), confirmed the predictions of computer simulations. The dynamic range of the estimated T2s through out different heart rates are significantly reduced from the proposed sequences compare to the other methods (1.0ms (Proposed) vs. 2.9ms (without SR) vs. 3.9ms (2D) , all $p<0.05$) . A representative set of mid-ventricular short-axis T2 maps acquired with the different T2 mapping strategies at different fixed heart rates is presented in panel C. Images acquired with conventional 2D T2 mapping and proposed T2 mapping without SR preparation showed a trend

with decreasing T2 as heart rates increases. Among these two T2 mapping methods, significantly lower T2 values were observed at HR= 100 bpm (45.1±1.7 ms (2D) vs 42.2±1.7 ms (without SR), both $p<0.05$) and 110 bpm (44.2±1.6 (2D) vs 41.6±1.7 (without SR), both $p<0.05$), compared to at HR=60bpm (2D: 47.6±2.1; without SR: 43.9±2.0). In contrary, images acquired with the proposed T2 mapping (with SR preparation) showed practically no sensitivity to HR. In particular, the T2 values acquired with the proposed approach did not differ from T2 estimates obtained using conventional 2D T2 and 3D T2 maps without SR preparation at a HR of 60 mmHg ($p=1$, for all).

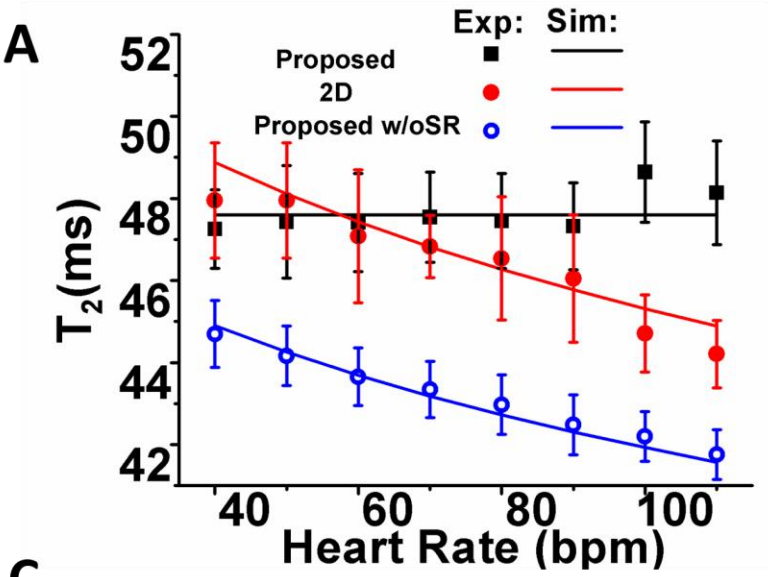

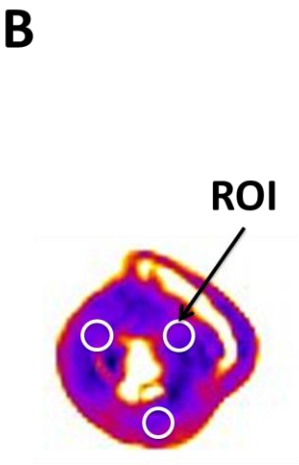

C

HR (Beats/Min)	40	60	100
Proposed sequence	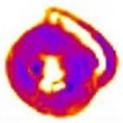	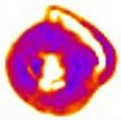	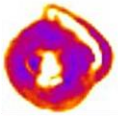
Myocardial T2(ms)	47.5±2.5	47.8±2.5	48.5±2.7
Proposed sequence without SR prep	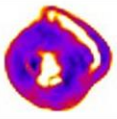	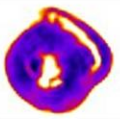	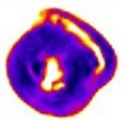
Myocardial T2(ms)	44.6±2.3 *	43.7±2.0 *	41.6±1.7 *
Conventional 2D Sequence	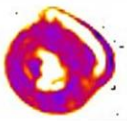	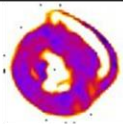	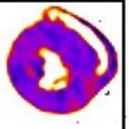
Myocardial T2(ms)	48.3±1.9	47.5±2.1	44.2±1.6 *

Fig. 3.9: T2 dependence on heart rate as determined from computer simulations and ex-vivo studies. In Panel A, the theoretically expected dependence of T2 on heart rate for the conventional 2D, 3D T2 mapping without (proposed w/o SR) and with SR preparation (proposed) are shown as solid lines. In addition, experimentally measured T2 values from ex-vivo hearts at the different artificially modulated heart rates are also shown. In Panel B, T2 maps acquired using the different T2 mapping approaches of a representative mid-ventricular slice image is shown. In Panel C, representative ROIs used for the analysis are identified for reference. Diminishing T2 values with increasing heart rates, as observed in conventional 2D T2 maps and 3D T2 maps without SR preparation were markedly reduced with the

*proposed 3D T2 mapping approach. All images showed consistent image quality and similar T2 distribution. * denotes $p<0.05$*

3.2.3.2 Animal Studies

The dependence of *Loss of Apparent MBR* on □HR is shown in Figure 3.10. Panel A shows a representative set of slice-matched rest and stress mid-ventricular images obtained with the proposed and conventional 2D sequences. In this particular example, a HR increase of 26 bpm under adenosine stress led to a 9% increase in MBR with the proposed approach, while a 1% decrease in MBR with the conventional 2D T2 mapping approach. PET measurements of the MBF in the same animal are shown in panel B. The corresponding global MPR in this animal was 2.45, which demonstrates the presence of marked vasodilation that is detected by the proposed method but not captured by conventional 2D T2 mapping approach. Panel C shows significant correlation between the *Loss of Apparent MBR* and □HR ($R=0.7$; $p<0.05$), which indicates that the larger the heart rate change under vasodilator stress (compared to at rest), the greater the *Loss of Apparent MBR* in T2 maps that are uncorrected for heart rates.

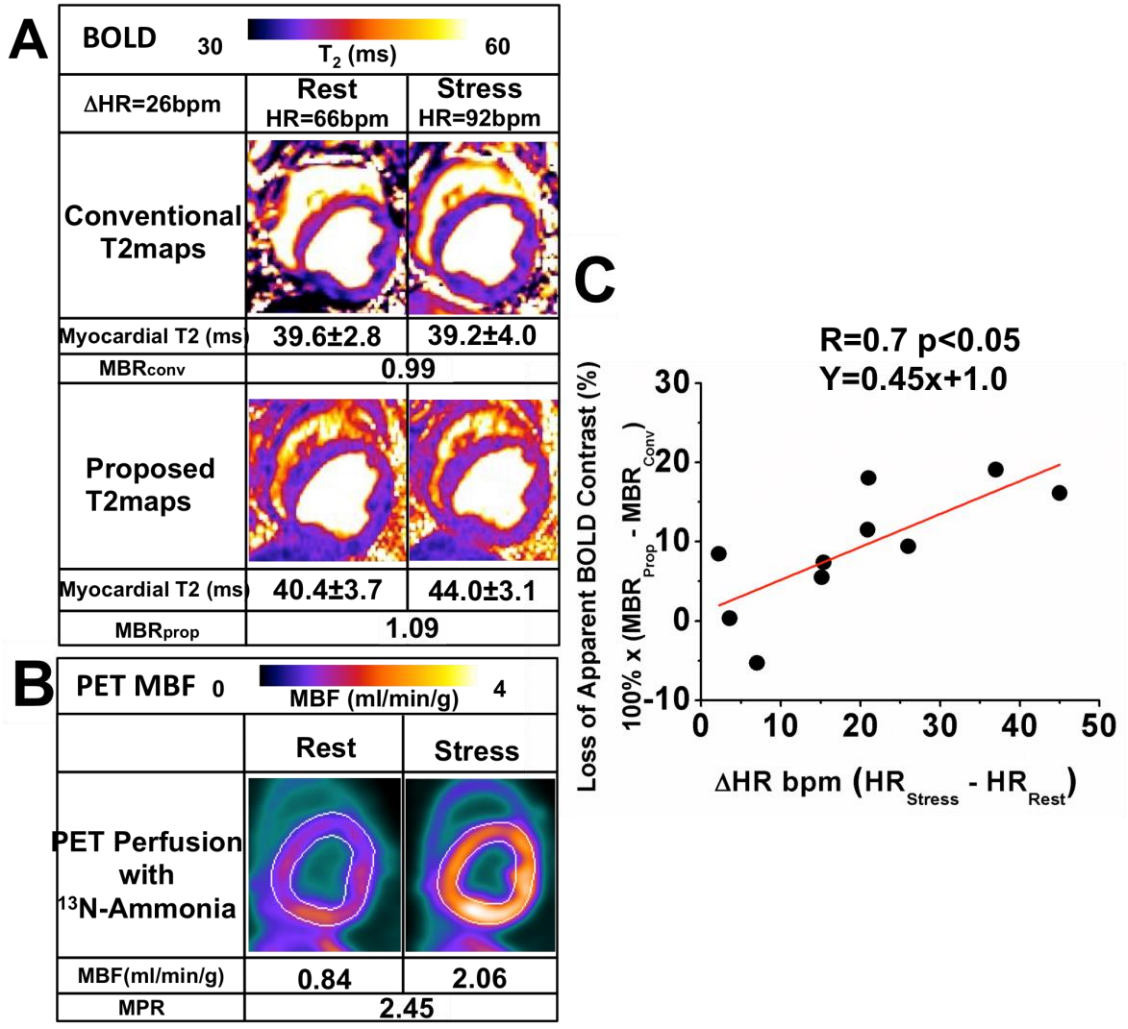

Fig. 3.10 Dependence of MBR Sensitivity on Heart Rate Differences Between Rest and Vasodilator Stress. Representative rest and stress T2 maps of a mid-ventricular slice obtained with conventional and proposed T2 mapping methods are shown in panel A. Myocardial T2 under stress with the proposed T2 mapping approach is much higher than the T2 at rest, but T2 under stress is reduced in the conventional images compared to rest. Panel B shows the experimentally observed relationship between Loss of Apparent MBR in conventional images and HR increases under vasodilator stress. A strong correlation was observed between Loss of Apparent MBR and ΔHR.

MBR and MPR in dogs without coronary stenosis following adenosine administration were consistently higher than at rest. Figure 3.11 shows representative sets of short-axis T2 maps depicting BOLD response (Fig 3.11A) and ^{13}N-ammonia PET perfusion (Fig 3.11C) acquired

under rest and adenosine stress. Corresponding bull's eye plots derived from segmental intensities are shown in Fig 3.11B and 3.11D, for BOLD CMR and ^{13}N-ammonia PET. Mean myocardial BOLD responses from segmental intensities were: 19±8% (BOLD CMR) and 2.5±0.4 (^{13}N-ammonia PET MPR).

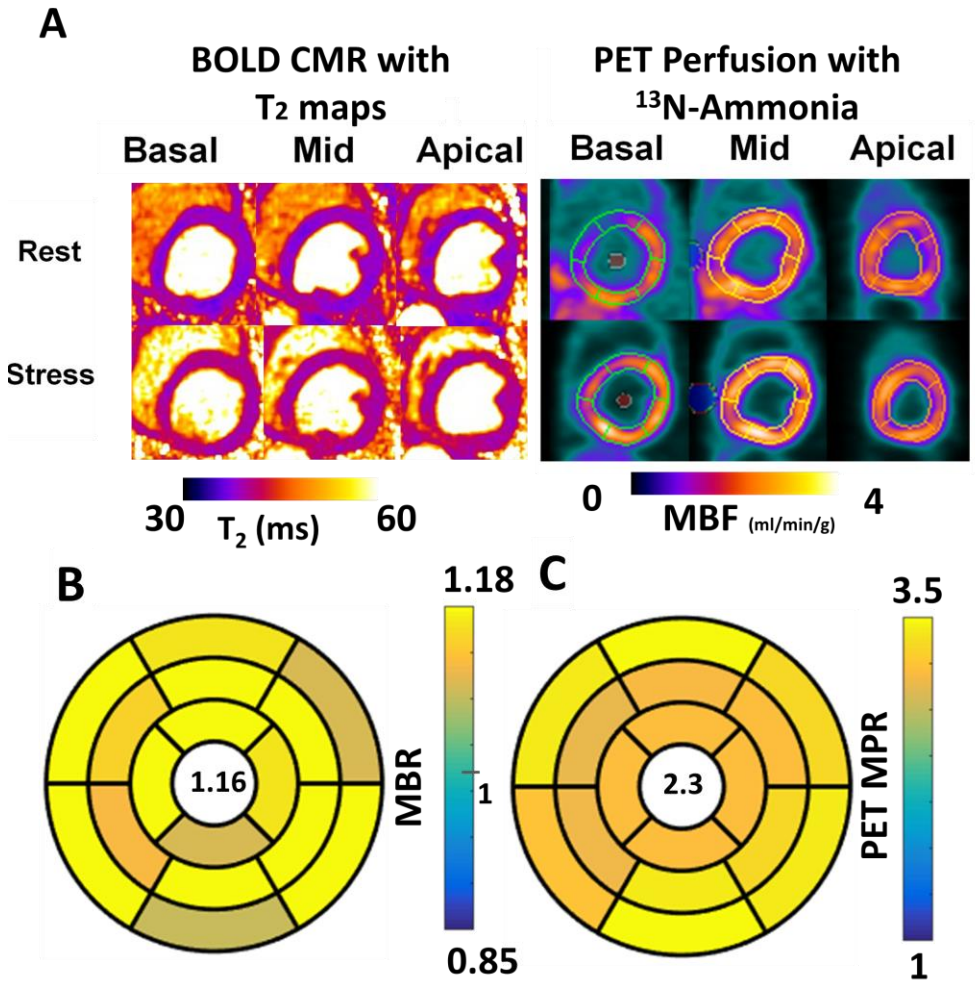

Fig. 3.11 3D T2 maps and 13N-ammonia PET at rest and under adenosine stress in canines without coronary stenosis. Representative basal, mid, and apical short-axis images of BOLD CMR with the proposed 3D T2 mapping approach and PET perfusion images with 13N-ammonia are shown in Panel A. From images acquired using both modalities, significant signal elevation can be observed in the stress

images compare to the corresponding rest images. Corresponding bull's eye plots are shown in Panels B and C, respectively. For this representative case, mean BOLD response of 16% and PET MPR of 2.3 were evident.

Absolute mean myocardial T2 and ^{13}N-ammonia PET perfusion values at rest and adenosine stress are shown in figure 3.12A and 3.12B, respectively. BOLD response and MPR from each segment are compared in Fig. 3.12C. ^{13}N-ammonia PET perfusion values were significantly higher under adenosine stress than at rest (0.8±0.1 ml/mg/min (rest) vs. 2.0±0.9 ml/mg/min (stress); $p<0.05$). The corresponding mean MPR was significantly larger than 2.0 (MPR: 2.6±0.3;refer to Fig. 3.12B). A similar trend was observed with T2 measurements, where myocardial T2 was significantly higher during adenosine stress (38.5±1.0 ms (rest) vs. 44.4±3.1 ms (stress), $p<0.05$; refer Fig. 3.12A) with a mean myocardial BOLD response of 19±8%. The segmental correlation between myocardial BOLD response and ^{13}N-ammonia PET MP was good ($R=0.7$; $p<0.05$).

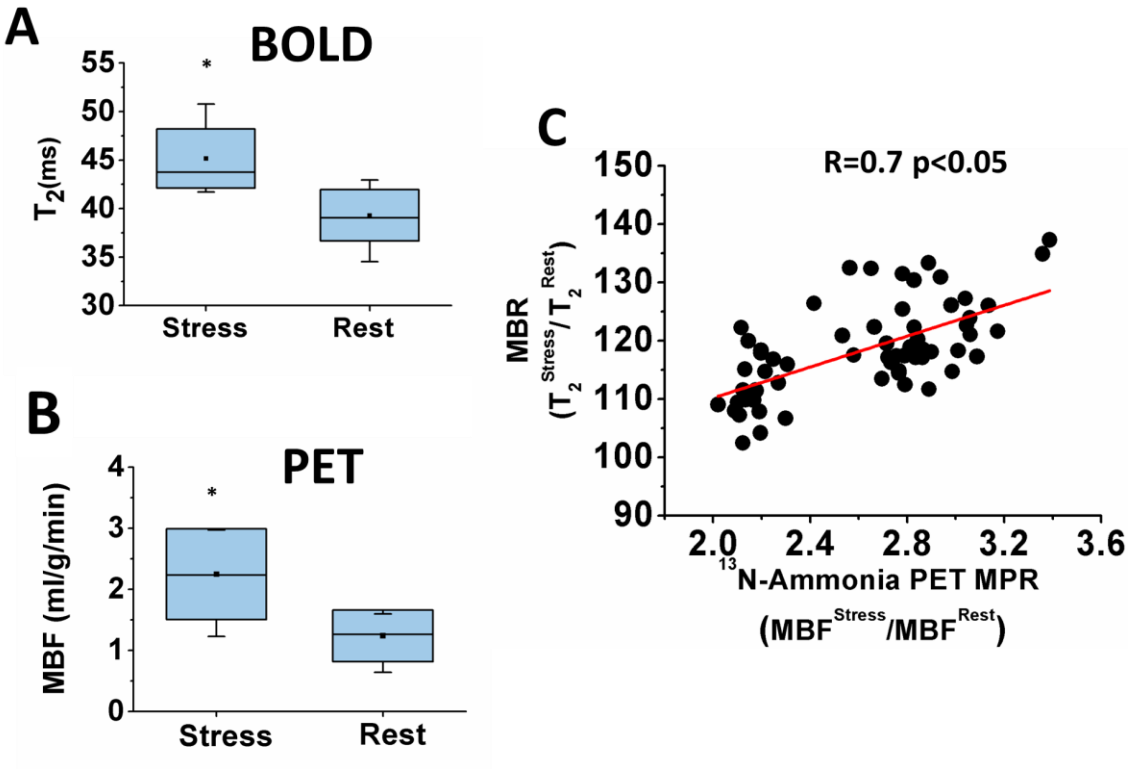

*Fig. 3.12: Mean BOLD Response and 13N-Ammonia PET Perfusion in Canines without Coronary Stenosis. Panel A shows a box plot with higher mean myocardial T2 values under adenosine adenosine stress compared to rest. Similar trend is observed with 13N-Ammonia PET perfusion measurements in Panel B. Panel C shows a scatter plot showing between BOLD response and 13N-Ammonia PET MPR. Linear regression analysis (line of best fit in red) shows good correlation between BOLD response and 13N-Ammonia PET MPR. * denotes p<0.05*

In *Group Stenosis*, a representative set of short-axis T2 maps depicting BOLD response and the corresponding rest and stress ^{13}N-ammonia PET perfusion in a dog with LAD stenosis are shown in Fig. 3.13 A and D, respectively. T2 maps acquired under adenosine showed a significant reduction in T2 is in the LAD territories of mid ventricular and apical slices, which is consistent with the reduced MBF in the ^{13}N-ammonia PET. Polar plots of MBR and MPR are shown in in Fig. 3.13 B and Fig. 3.13 E, respectively, which show reduced MBR and MPR consistent with a LAD coronary stenosis. Box plots of MBR and MPR in the remote and affected segments are

shown in Fig. 3.13 C and Fig. 3.13 F, respectively. Mean MBR and MPR of the affected territories were significantly lower than the remote territories ((MBR: 1.09 ± 0.04 (remote) vs. 1.00±0.03 (affected), $p<0.05$); and MPR: 2.5±1.7 (remote) vs. 1.4±1.0 (affected), $p<0.05$).

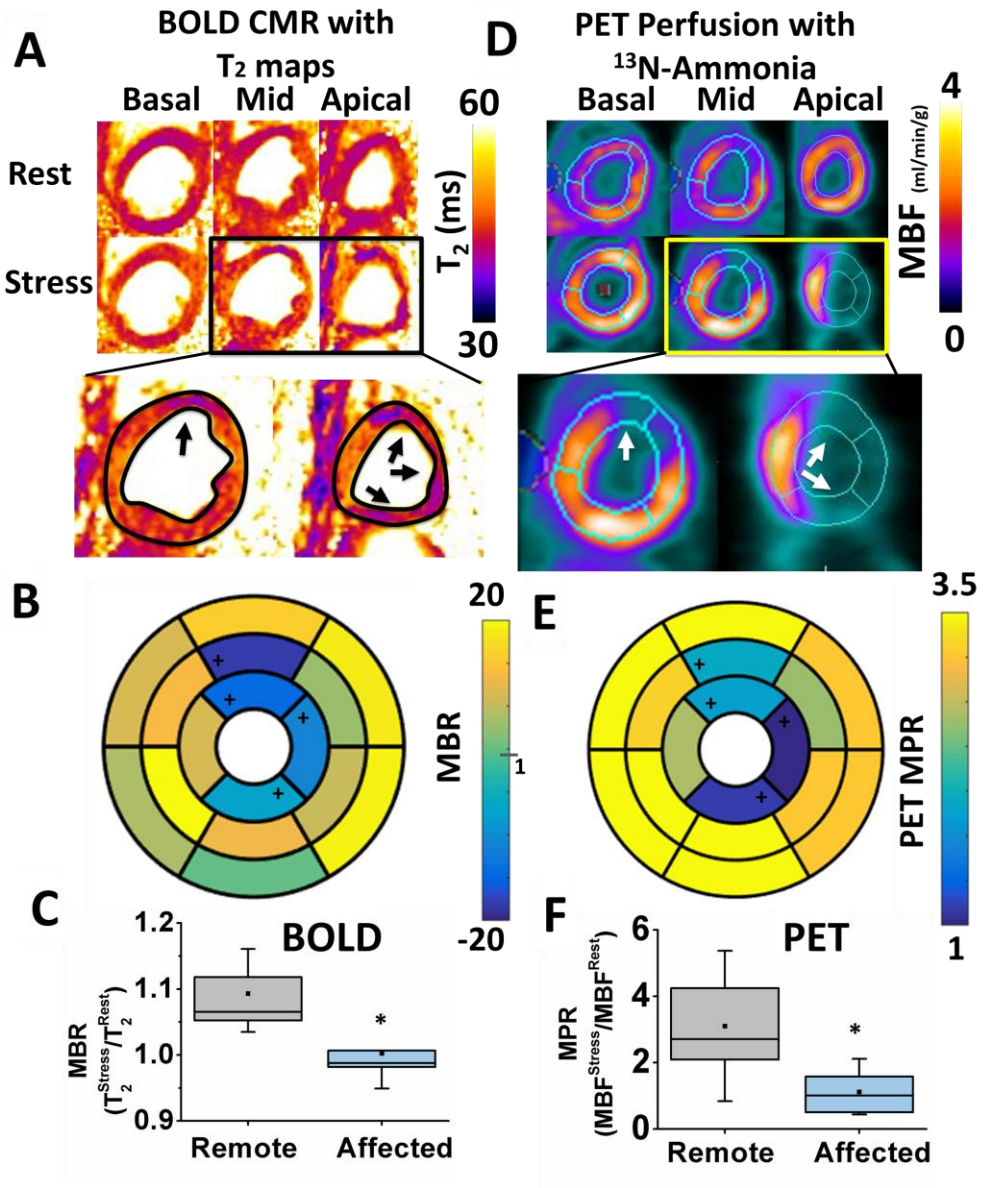

Fig. 3.13: 3D T2 maps and 13N-ammonia PET at rest and under adenosine stress in canines with LAD coronary stenosis. Panel A shows representative basal, mid, and apical short-axis T2 maps at rest and under stress from a canine with LAD coronary stenosis. Panel D shows the corresponding quantitative myocardial blood flow (MBF) maps determined from 13N-ammonia PET. Note the close correspondence

*in the MBF distribution and T2 maps, particularly under adenosine stress. Specifically, the remote territories on PET images showed increased T2 values on T2 maps acquired under adenosine. Conversely, the affected territories on PET images (anterior wall corresponding to LAD territory; white arrows in zoomed-in images) showed markedly diminished increase in T2 (black arrows in zoomed-in images) compared to remote segments. Corresponding polar maps for BOLD and PET are shown in Panels B and E, respectively. Affected segments identified with change analysis from QPET are labeled with '+' in the polar maps. Both BOLD Response and PET MPR showed significantly lower values in the affected territories compare to the remote segments (Panels C and F, respectively). * denotes p<0.05.*

3.2.3.3 Human Studies

Every stress and rest scans were completed within 4 minutes. Consistent with canine studies, significant increases in myocardial T2 was observed during stress compared to rest (44.5±2.8ms (rest) vs. 49.1±5.8ms (stress); $p<0.05$). Mean MBR across subjects was significantly larger than 1 (mean MBR=1.10± 0.08; $p<0.05$). Representative short axis-images from a healthy volunteer along with a corresponding polar map representation of MBR are shown in Figs. 3.14A and 3.14B, respectively. All three images showed visually discernable increases in T2 during stress compared to at rest.

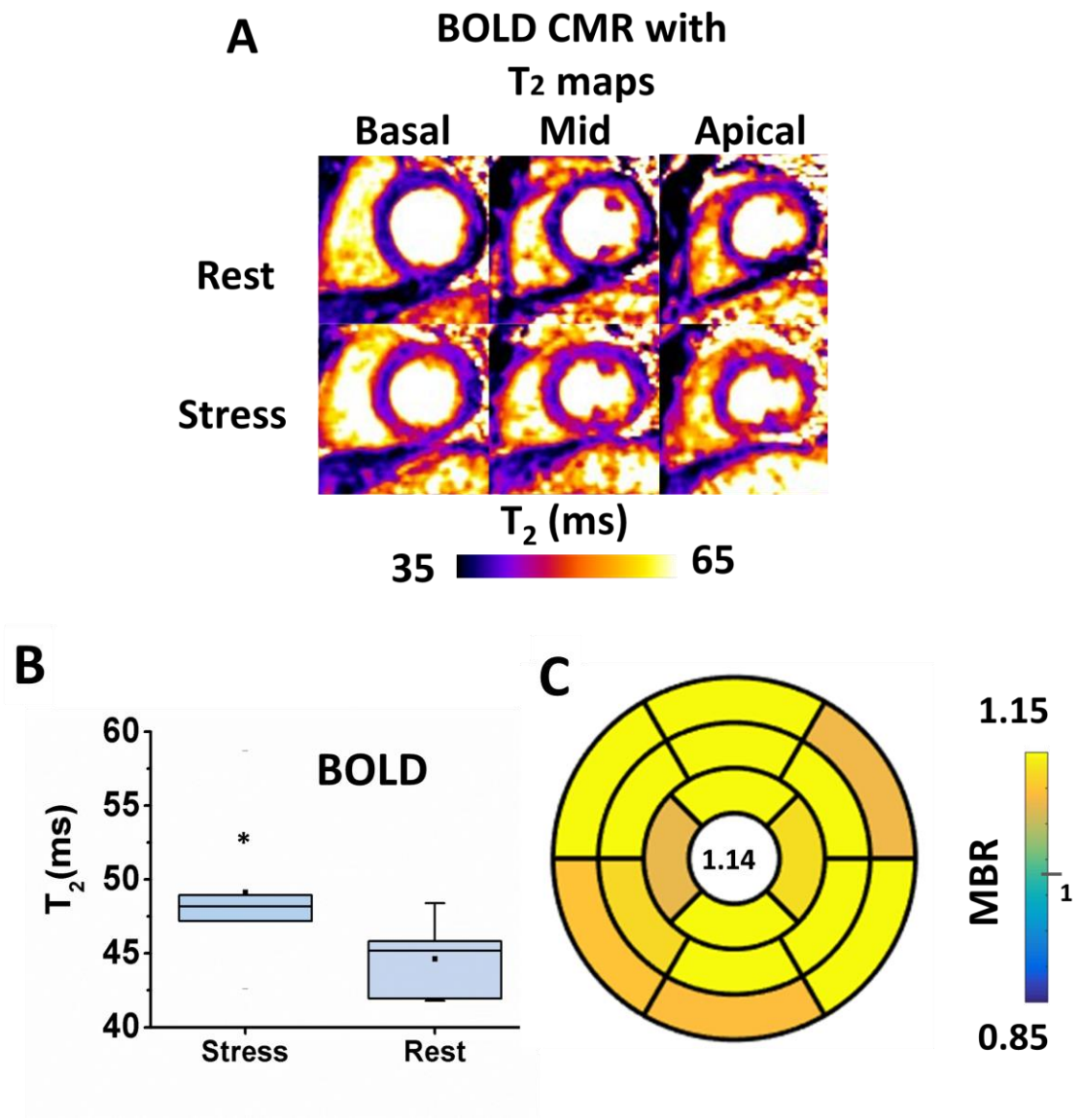

Fig.3.14 Heart-Rate Independent 3D T2 mapping at Rest and Under Adenosine Stress in Healthy Human Subjects. Panel A shows representative short-axis T2 maps from rest and stress. An increased myocardial T2 corresponding to hyperemia can be observed across all slices. Panel B shows box plots of myocardial T2 values across animals at rest and under stress. Panel C shows a polar map of MBR for the case in panel A, which show a relatively homogenous MBR across the segments that are greater than 1.

3.2.4 DISCUSSION

A non-contrast-enhanced, radiation-free, imaging approach which can be used to reliably detect the presence of hypoperfused myocardial territories could be valuable in ischemia testing in patients with compromised kidney function. Over the past two decades BOLD CMR has made substantial advancements towards filling this role. However, the most commonly employed T2-based BOLD CMR methods have well-known limitations. Specifically, they offer limited spatial coverage during vasodilator stress, are confounded by heart-rate variations between rest and stress acquisitions, and have not yet been directly validated against gold-standard PET-perfusion measurements under identical physiological conditions. Our work developed, tested and validated a new T2-based BOLD CMR approach at 3T to overcome these key imitations. This led us to demonstrate for the first time a quantitative BOLD CMR approach which (a) permits full LV coverage within the duration of adenosine stress under free-breathing conditions; (b) ensures preservation of BOLD sensitivity independent of heart-rate variations between rest and stress; and (c) is validated in vivo against ^{13}N-ammonia PET-based myocardial perfusion under identical physiological conditions.

Our studies relied on computer simulations, ex-vivo imaging, in-vivo imaging in canines with and without coronary stenosis and early demonstration of feasibility in healthy human subjects. The proposed method was compared against established (84) 2D T2 mapping approach and the proposed method without the SR preparation. Computer simulations and ex-vivo studies demonstrated a clear dependence of T2 on artificially modulated heart rates that were not evident with the proposed approach. By using a SR preparation, the proposed method ensured that the longitudinal signal recovery begins from zero during each of the segmented readouts, hence removing the variability associated with longitudinal signal recovery, which is highly dependent

on heart rates. This dependence of HR on T2 has important implications for BOLD CMR. As shown in Fig. 3.10, T2 mapping methods that are sensitive to HR can underestimate the expected BOLD response and the magnitude of this underestimation is proportional to □HR. Effectively, this underestimation in T2 counters the vasodilator mediated increase in T2 leading to a diminished and unreliable apparent BOLD response, which may partly account for the large scatter typically observed between T2-based BOLD CMR and perfusion studies in the literature.

These variations might also lead to incorrect estimation of myocardial oxygen extraction fraction (OEF) (33) and confound the BOLD interpretations. The proposed T2 method helps to overcome these limitations. Previous studies have recognized these limitations and have attempted to correct for signal measurements using fixed model parameters that are often variable between subjects and imaging conditions (19), which can lead to further misinterpretations. BOLD sensitive balanced steady state freee precessing (bSSFP) sequence is another way of reducing the heart rate dependency by reaching the steady state(121,122). However, other limitations, such as off resonance artifacts, long breath hold duration and single slice 2D acquisitions, still limited its applicability. The proposed method provides fast 3D free breathing acquisition capability while eliminating the HR and T1 dependency. Although SR preparation methods are often limited by SNR, in our 3D implementation, we did not find this to be the case as the proposed approach showed comparable standard deviation in T2 in the myocardium (1.16±0.12 ms (proposed) vs. 1.25±0.35 ms (conventional approach), p=0.3).

We were able to consistently acquire complete data sets within 4 minutes during adenosine infusion for whole-heart T2 mapping with similar spatial resolution of 2D T2 maps. Our data showed that the T2 values of the healthy myocardium measured at rest using the proposed approach were in good agreement with previous reports in the literature (123,124).

Simultaneously acquired T2 and ^{13}N-ammonia PET data, which were used to estimate MBR and MPR, respectively, were highly correlated. In the presence of LAD stenosis, consistent with the findings from ^{13}N-ammonia PET MPR, we observed marked reduction in MBR in the affected territories compared to remote territories. Collectively these findings support that the measures of MBR based on the proposed approach and MPR provide similar information with respect to myocardial perfusion and can be used to improve the identification of myocardial territories subtended by coronary arteries with non-flow limiting stenosis. Further, our studies in healthy human subjects demonstrated the feasibility of the proposed approach for consistently generating artifact-minimized, whole-heart T2 maps from free-breathing acquisitions at rest and standard duration of peak adenosine stress (i.e., within 4 minutes). Although the MBR estimates in human subjects were not validated with PET MPR, the observed mean MBR of 10% in human subjects is comparable to that observed in animals.

Study Limitations

The present study was performed in animal models and healthy human subjects, which offer well-controlled environments compared to the clinical setting. While we were able to consistently acquire whole-heart T2 maps within acceptable window of adenosine stress and eliminate heart-rate dependency, along with marked reductions in B0 and B1 inhomogeneities, rapid heart rate changes during the acquisition may be challenging. Although this may be addressed using strategies similar to arrhythmia rejection approaches previously employed in other settings, this was not investigated here. These investigations would require patient studies.

3.2.5 CONCLUSION

To overcome the key limitations in cardiac BOLD CMR, we developed, tested, and validated a new 3D T2 mapping approach. The proposed approach offers the capability to acquire artifact-minimized, quantitative, whole-heart, BOLD images under free-breathing conditions during peak adenosine stress with no loss in sensitivity from heart rate changes between rest and stress. Patient studies are necessary for clinical translation.

Chapter 4 BOLD CMR Based on Pharmacokinetics of Regadenoson

4.1 Towards Reliable BOLD CMR Using Late Effects of Regadenoson

4.1.1 INTRODUCTION

The number of cardiac patients with chronic kidney disease is on the rise. Assessment of ischemic heart disease in these patients requires a non-contrast-enhanced, high-resolution, imaging approaches to evaluate the presence of perfusion anomalies. Myocardial BOLD MRI has the capacity to fill that unmet need. Over the past two decades myocardial BOLD MRI has seen major technical advancements and a number of clinical validation studies. However, the reliability of BOLD MRI remains a key weakness for its widespread adoption for routine clinical use. To date, most of the technical developments have addressed improvements in imaging speed, coverage and reducing image artifacts at rest. However, image artifacts from unpredictable cardiac motion during stress can lead to significant deterioration of image quality, which can confound/mask the BOLD signal changes during stress. Since the FDA approval in 2008, Regadenoson (Gilead Sciences Inc) has become a popular stress agent and is currently used in ~70% of the pharmacological stress in the US owing to its improving patient tolerability and ease of administration. Studies have also shown that regadenoson can prolong the coronary vasodilation to 8-10 minutes, but to date no studies have quantified the myocardial blood flow (MBF) during the late phase of vasodilation. We hypothesized that (a) stress BOLD MRI performed at ~10 minutes can markedly improve the reliability for detecting myocardial hyperemia; and (b) that myocardial perfusion reserve remains significantly greater than 2.0 (a

meaningful hyperemic state for ischemic testing) following regadenoson injection. We studied this using a canine model in a hybrid PET/MR system, which is capable of reporting BOLD signal changes (from MRI) and quantitative blood flow changes (from ^{13}N-ammonia PET) in the heart.

4.1.2 METHODS

Healthy mongrel dogs (n=7) were studied in a state-of-the-art PET-MR system (Biograph mMR, Siemens Healthcare, Germany). After scouting and whole-heart shimming, BOLD images were acquired with 2D T_2 maps at rest simultaneously with dynamic ^{13}N-ammonia PET. Following a 40-min gap to ensure sufficient decay of radiotracer, a bolus injection of regadenoson (2.5 μg/kg) was administrated. T_2 maps were acquired 2 mins and 10 mins post regadenoson administration (p.r.a) to investigate the mean BOLD response and reliability of the BOLD response. To quantify the extent of myocardial hyperemia 10 mins p.r.a, another dynamic ^{13}N-ammonia PET was also acquired. Mean and standard deviation (σ) of myocardial T_2 were measured from images acquired at rest and at 2 mins and 10 mins p.r.a.. *Myocardial BOLD Response* (indexed as T_2(stress)/T_2(rest)) and *Myocardial BOLD Variability* (indexed as σT_2(stress)/σT_2(rest)) and were computed at 2 mins and 10 mins p.r.a, respectively to assess mean BOLD response and the reliability of BOLD response. MR-based attenuation corrected PET images were analyzed in standard fashion with commercially available qPET software and were matched to the corresponding BOLD imaging slices to determine myocardial perfusion reserve (MPR) at 10 minutes p.r.a and regressed against *Myocardial BOLD Response*.

4.1.3 RESULTS

A box-plot of observed *Myocardial BOLD Variability* at 2-mins and 10-mins p.r.a (and at rest, for reference), along with representative mid-ventricular, short-axis, T_2 maps corresponding to the different conditions are shown in Fig. 4.1. Note the extensive image artifacts present in the representative T_2 map at 2 min (from the intense heart-rate variability during acquisition), which is absent in the T_2 maps acquired at rest and 10-mins p.r.a. Relative to 2-min p.r.a, *Myocardial BOLD Variability* was significantly larger at 2-min p.r.a (1.6±0.9) compared to 10-mins p.r.a (1.0±0.3) and at rest (1.0); $p<0.05$ for both. Average reduction in *Myocardial BOLD Variability* between 2-min and 10-mins p.r.a was 0.6±1.2.

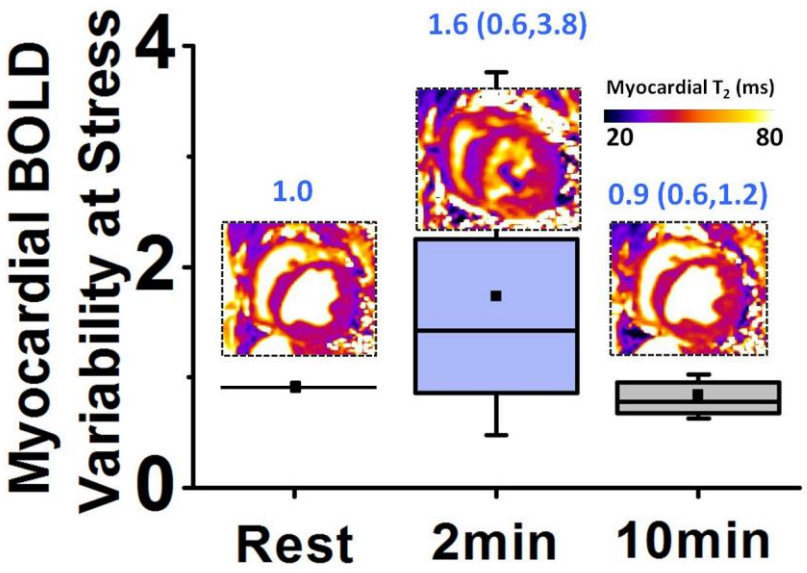

Figure 4.1. Myocardial BOLD Variability at Stress Relative to Rest. Box-plot of Myocardial BOLD Variability and representative images at rest and from 2 and 10 min p.r.a are shown. Large Myocardial BOLD Variability is observed at 2 mins p.r.a. compared to rest and is markedly reduced at 10 mins p.r.a.

Representative ^{13}N-ammonia PET images of MBF at rest and 10-mins p.r.a are shown in Fig. 4.2A. MBF at 10 min (1.8±0.9 ml/g/min) was significantly higher than at rest (0.6±0.3ml/g/min), $p<0.05$ (Fig. 4.2B). Mean MPR from PET at 10-min p.r.a was significantly larger than 2.0 (3.0±0.6, $p<0.05$). BOLD images corresponding to the PET images in Fig. 4.2A are shown in Fig. 4.2C. Myocardial T_2 at 10-min p.r.a (40.4±1.7ms) was significantly higher than at rest (37.1±2.0ms), $p<0.05$ (Fig. 4.2D). Mean *Myocardial BOLD Response* at 10-min p.r.a was significantly higher than 1.0 (1.09±0.04<0.05). Strong correlation between PET MPR and *Myocardial BOLD Response* was observed ($R=0.7$, $p<0.05$); Refer to Fig. 4.2E.

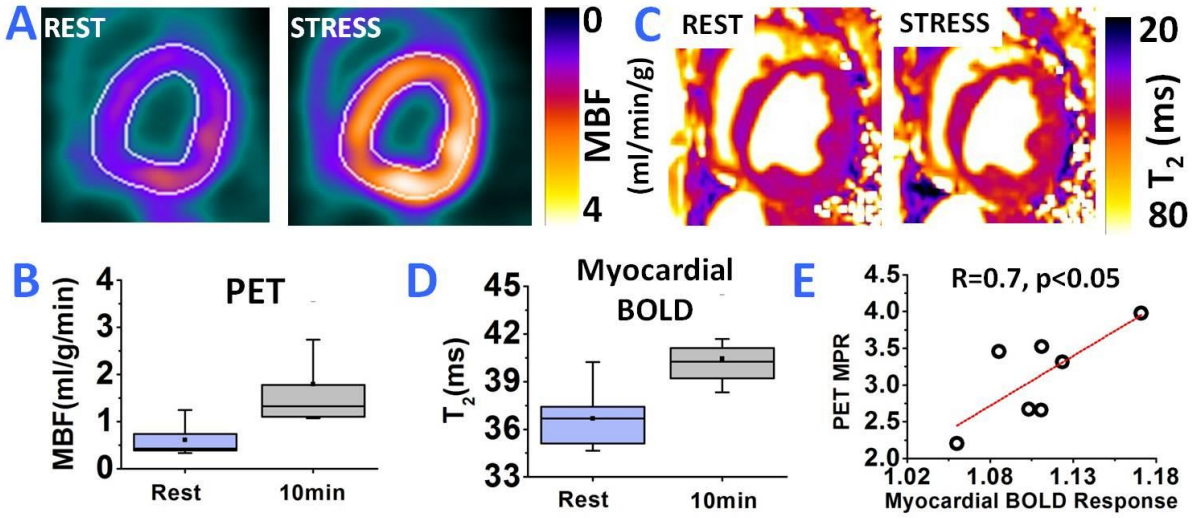

Figure 4.2. ^{13}N-Ammonia PET Myocardial Blood Flow and BOLD. Both PET and BOLD images showed significant increase in MBF and BOLD response, at 10 mins p.r.a. compared to rest (A-D). Results from regression analysis showed good correlation between PET myocardial perfusion reserve (MBF(stress)/MBF(rest)) and Myocardial BOLD Response($R=0.7$, $p<0.05$; panel E).

4.1.4 CONCLUSIONS

Myocardial BOLD images acquired at 10-mins p.r.a were free of image artifacts typically observed in images acquired at 2-min p.r.a. MPR values at 10-mins p.r.a were significantly higher than 2.0 and were strongly correlated with the Myocardial BOLD Response. These data suggest that delayed BOLD acquisition following regadenoson administration can be a practical strategy for increasing the reliability of cardiac BOLD MRI for cardiac stress testing. The clinical utility of this approach remains to be evaluated in human subjects.

4.2 Improving the Reliability of Myocardial BOLD CMR through Characterization of Coronary Relaxation Following Regadenoson Injection

4.2.1 INTRODUCTION:

Over the past two decades BOLD CMR has seen major progress in technical developments and advanced by a number of clinical validation studies. However, the reliability of BOLD CMR remains a key weakness for its widespread adoption for routine clinical use. Although technical developments as presented in our previous work have significantly improved imaging speed, coverage and helped to reduce imaging confounders, the unstable physiological conditions during vasodilator stress leads to significant variations in the BOLD measurements. Specifically, irregular cardiac motion, rapidly changing heart rate during acquisition and significantly shorter quiescent period contribute to motion artifacts, cardiac phase mismatch between rest and stress image, all of which lead to deterioration of BOLD images. This invariably masks the observed BOLD responses during stress and can diminish the reliability of the data interpretation.

Coronary Relaxation Dynamics in the Presence of Regadenoson:

Since the FDA approval in 2008, Regadenoson (Lexiscan,Gilead Sciences Inc.) has become a popular stress agent and rapidly grown to capture nearly 70% (125) of the pharmacological stress market in the US owing to its specificity to A_{2A} adenosine receptor (improving patient tolerability) and ease of administration (bolus injection rather than continuous infusion). However, a rapidly changing cardiac motion (fig 4.3 A) post regadenoson administration can affect the conventional single time point BOLD imaging strategy in 2 ways: (i). irregular motion can leading to motion artifacts, can degrade image quality and result inb cardiac phase mismatch (fig4.3 B),(126); and (ii). heart rate differences between rest to stress can confound the measured BOLD signal and mask the BOLD response.

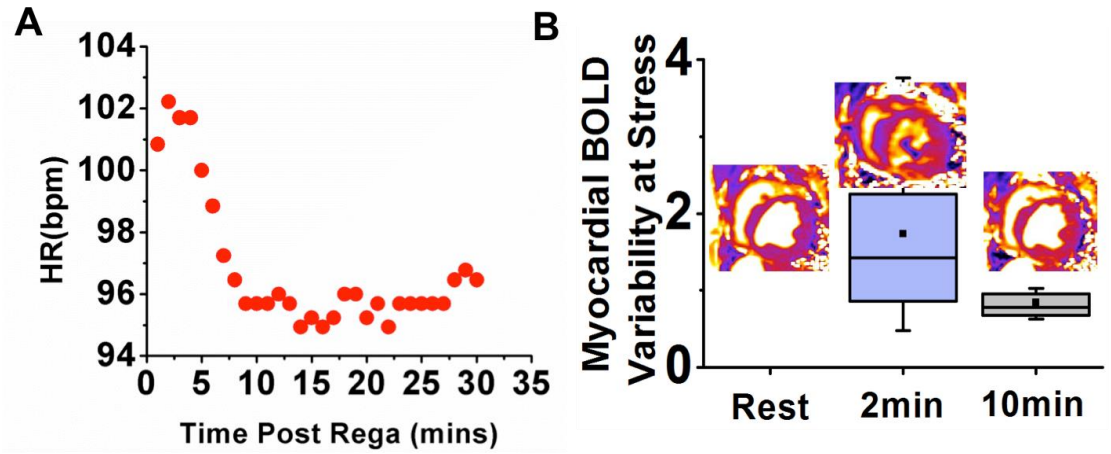

Fig 4.3 Heat-rate response and the BOLD image quality influence by different imaging time points. Significant heartrate variation is observed in an animal for the first 5 minutes after regadenosine administration(A). The affected BOLD image quality due to imperfect imaging condition(B).

Although advanced MR technical development as mentioned in chapter 3 can overcome part of the challenges, the unpredictable cardiac motion can still undermine the robustness of the image quality and prolong the scan time. An alternative method is proposed in chapter 4.1 to acquire

stress images at a delayed time point, which can provide a stable imaging condition and improve the scan reliability (126). However, it can also potentially decrease the sensitivity of detecting disease as the imaging is performed well after peak vasodilation.

In this study, we hypothesize that continuous monitoring of the myocardial BOLD signal after regadenoson administration can improve the robustness of BOLD response extraction while preserving the sensitivity of peak vasodilation. To achieve this, we propose a multiple measurement strategy to investigate the coronary dynamic after regadenoson administration and reduce the influence on the BOLD response from artifacts in a single image. We applied a mono-exponential decay model to extract the coronary dynamic parameters (CDPs), and derive the maximum BOLD response to compare with the conventional single time point method.

We studied healthy human volunteers, intact dogs and dogs with chronic myocardial infarction to evaluate the capability of BOLD CMR for characterizing the coronary dynamics. In the healthy subjects, global CDPs were extracted to show the feasibility of the method and the increased BOLD sensitivity. In the pathologic cases, CDPs were compared between remote and affected territories in segmental and pixel wise fashions to evaluate the capability of detecting abnormal myocardial territories.

4.2.2 METHODS

BOLD images were acquired at different time points before and after regadenoson administration to sample the rest and stress images, respectively. After bolus regadenoson injection, multiple stress images were acquired to sample the coronary dynamics curve for 30 minutes. All stress images were registered to the rest images with a non-rigid motion correction algorithm (127) to

correct for motion-induced miss match between acquisitions. Motion corrected images were used to extract the CDPs throughout the stress period using a mono-exponential model (128) ($T_2(t)= T_{2o}+\Delta T_{2max} \exp(-t/\tau)$). A flow chart of the experimental setup is depicted in Fig4.4

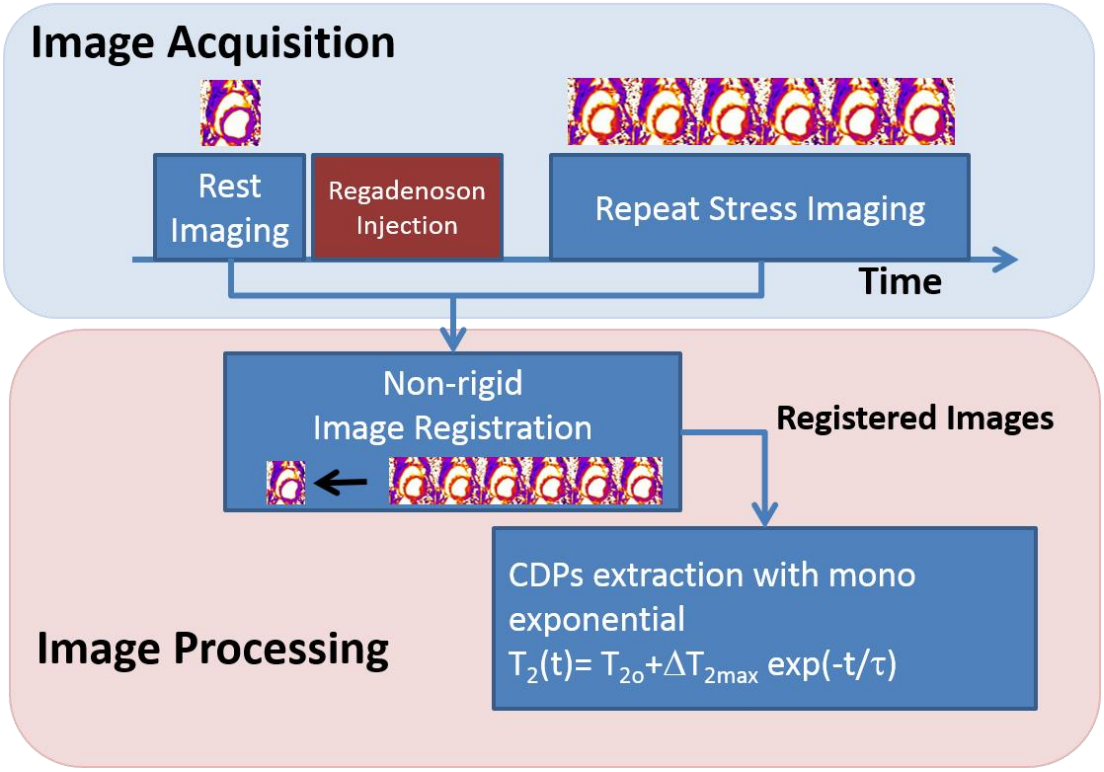

Fig4.4 Experimental flow chart. Rest BOLD images were acquired before Regadenoson administration and repeat BOLD acquisitions starting from 2 minutes post the bolus regadenoson injection were performed. Images were acquired every 1-5 minutes for 30 minutes. The stress images were registered to the rest image using a non-rigid motion correction algorithm (127). The motion corrected images were used to fit the coronary dynamics parameters with a mono-exponential model.

In healthy volunteers and intact dogs, global CDPs were extracted from the myocardium. Maximum BOLD response was derived with CDPs ($MBR_{CDP}= \Delta T_{2max} / T_{2o}$ x 100%) and compared with conventional myocardial BOLD response (MBR), which was derived as the T_2 elevation from rest to 2 minutes after regadenoson administration ($MBR_{conv}= [(Stress T_2^{2min} /Rest T_2) -1)$ x 100%]. In the animals with coronary impairment, CDPs were measured in segmental

and pixel-wise manner. Pixel-wised CDPs between remote and affected territories were segmented using SVMs to investigate the capability of separating diseased myocardium from the remote regions. In addition, CDPs were derived from subsets of BOLD images with different starting time points to probe the optimized setup of detecting affected territories. Details of each step are described in the following sections

Experimental Subjects and animal preparation:

We studied healthy human volunteers (n=6), intact dogs (n=7) and dogs with chronic infarctions (n=1). During imaging studies in animals, all animals were mechanically ventilated and anesthetized with propofol. In the dog with chronic infarction, the animal underwent an open chest ischemia reperfusion protocol (3 hours of ischemia followed by reperfusion), followed by 8-week recovery prior to imaging.

Image acquisition:

Human studies were performed on a 3.0 T clinical MRI system (MAGNETOM Verio®, Siemens Healthcare, Erlangen, Germany) and the animals were studied on a 3T whole body PET MR system (Biograph mMR, Siemens Healthcare, Erlangen, Germany). In all subjects, BOLD images were acquired with a commercially available 2D T2 mapping sequence {Giri, 2009 #820}. In all studies, after localization and shimming, rest BOLD images were acquired under baseline followed by a bolus regadenoson injection. Post regadenoson administration, BOLD CMR images were acquired between 2 to 30 minutes after regadenoson injection with an interval of 1-5 minutes depend on the physiological and imaging condition. In the animal with chronic infarction, simultaneous ^{13}N ammonia PET images were acquired at 2 minutes post regadenoson administration to validate the hyperemic response from regadenoson. In addition, LGE images

were acquired to identify the infarcted territories after all BOLD acquisitions were completed. Block representations of imaging protocols are illustrated in figure 4.5. Imaging parameters are listed as the following:

T2 mapping: TR/TE = 2.9 ms/1.1 ms, iPAT=2, partial Fourier = 3/4, FA = 35°, BW = 1184 Hz/ pixel, 86 lines per heartbeat (simulated rate 60/s), trigger pulse = 4, FOV = 288x360 mm^2, matrix size =154x192, and voxel size = 2.5 x 1.7 x 6.0 mm^3, T_2 preparation (as TEs) = 0, 24, 55ms.

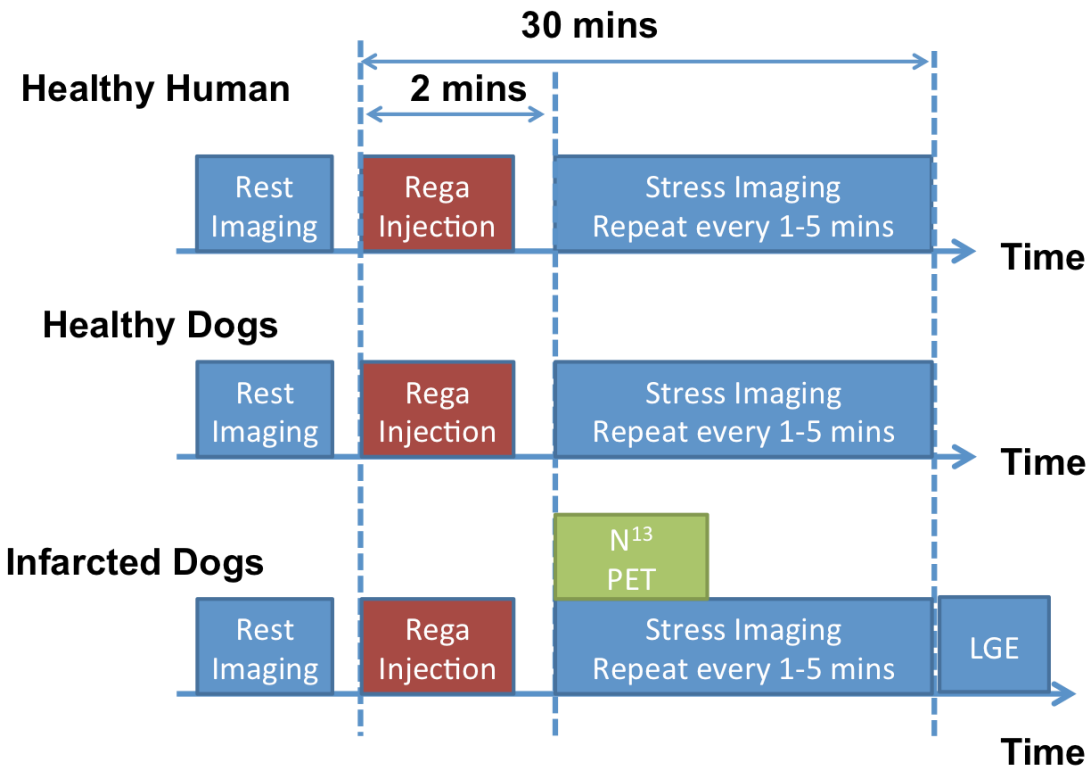

Fig. 4.5 Chronical order of image acquisition for each imaging group.

Late Gadolinium Enhancement (LGE): PSIR LGE images were acquired 10 minutes after Gd-DTPA infusion (0.2 mmol/kg, gadoversetamide/Optimark, Mallinckrodt Inc., Hazelwood, MO), using non-selective inversion recovery preparation with GRE readout (TR/TE = 3.2/1.5 ms, FA

= 20°, BW = 586 Hz/pixel, matrix = 96 × 192, in-plane resolution = 1.3 × 1.3 mm^2; and slice thickness = 6.0 mm). A TI-scout sequence was used to find the optimal TI for nulling the healthy myocardium (240–270 ms).

Image Processing:

The series of BOLD images acquired post regadenoson administration were aligned using the advanced normalization tools (ANTS: http://www.picsl.upenn.edu/ANTS) software. Rest images were used as the reference for registration. For each subject, ANTS utilized a cross-correlation-based symmetric diffeomorphic transformation between the reference image and the target images to minimize image differences. The representative effect of image registration is presented in fig. 4.6.

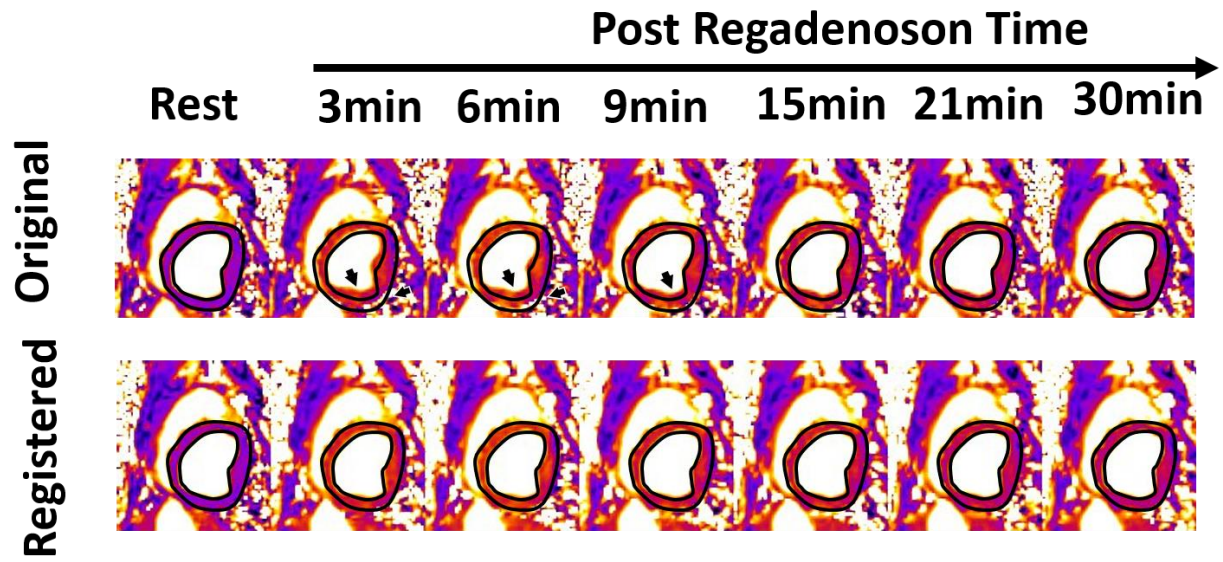

Fig. 4.6 Effect of the non-rigid motion correction algorithm. Contour mismatch (black arrows) from the original images are successfully registered to the rest image after motion correction.

Aligned images were used to fit CDPs on a pixel-by-pixel basis in the myocardial ROI. In all studies, a mono exponential model $T_2(t)= T_{2o}+\Delta T_{2max} \exp(-t/\tau)$ (128) was used to represent the BOLD signal modulation post regadenoson injection and extract CDP maps from BOLD images of the whole period(T_{2o} = baseline T_2, ms; ΔT_{2max} = Maximum BOLD stimulation amplitude, ms; τ= coronary relaxation time constant, min). The rest images were set to be the fully decayed to baseline BOLD signal at 2 hours after regadenoson injection in the dynamic curve fitting (129). In the diseased animal, CDPs were fitted with different starting time points (2mins, 5mins and 10 mins) to investigate the influence decreased sampling of data points close to the peak vasodilation.

Image analysis:

In the studies performed in healthy volunteers and animals, global myocardial CDPs were extracted to investigate the feasibility of probing BOLD response. Myocardium was segmented with epi- and endocardial contours. Global myocardial CDPs were measured and compared with the conventional single time point T2 response between Rest and Stress. In the studies with coronary impairment, infarcted territories were identified using LGE images with remote + 5 SD criteria as previously described (fig. 4.7).

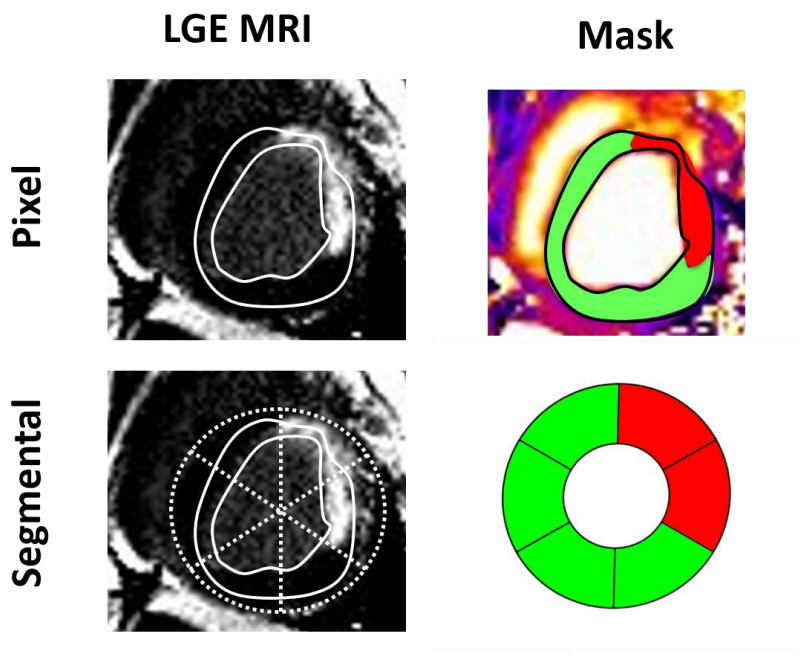

Fig. 4.7 Infarcted territories identified from LGE images. Pixel-wise and segmental masks of infarcted territories identified with +5SD standard are presented. Remote territories are labeled with green and affected territories are labeled with red.

The capability of identifying the affected myocardium on the CDPs was examined using cross validation of support vector machines (SVMs) (fig. 4.8) and compared with the conventional single time point T2 based classification. The analysis was first performed in a pixel-wised fashion and compared in on the basis of standard AHA segmentation (fig. 4.7).

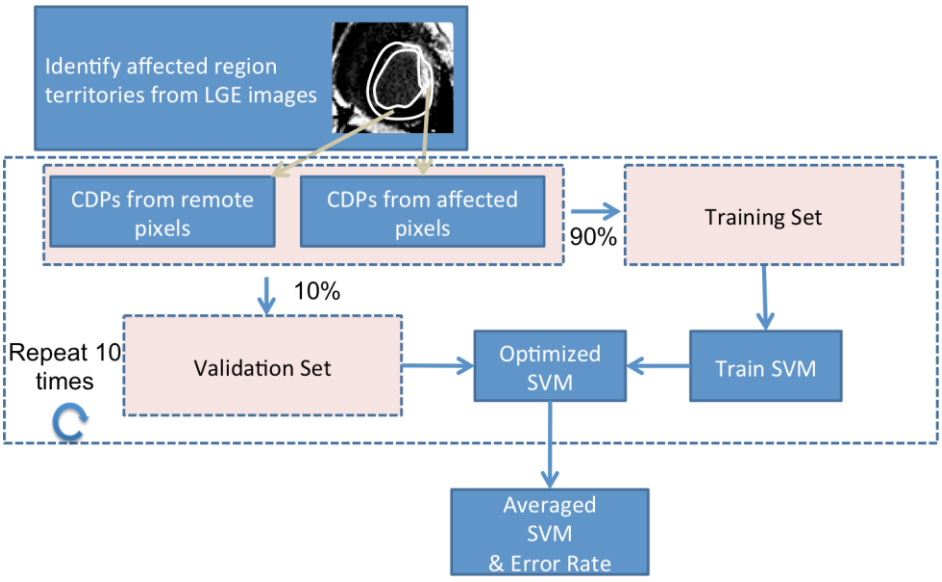

Fig.4.8 Flow chart of the SVM cross validation process for evaluating the disease separation capability of the CDPs. The myocardial pixels were labeled using LGE images before the SVM training. Myocardial CDPs are separated into 10 subgroups in which 9 groups will be used to train an SVM. The SMV is used to segment the last group to test the segmentation accuracy and examine the disease identification capability from the CDPs. The process is repeated for 10 times to cross validate the whole dataset.

In addition, simultaneously acquired quantitative PET images were used to derive myocardial perfusion reserve (MPR) with a clinical validated software (QPET, Cedars-Sinai Medical Center, Los Angeles) and to validate the reduced MPR in the infarcted myocardium.

4.2.3 RESULTS

4.2.3.1 Coronary Dynamics in Health

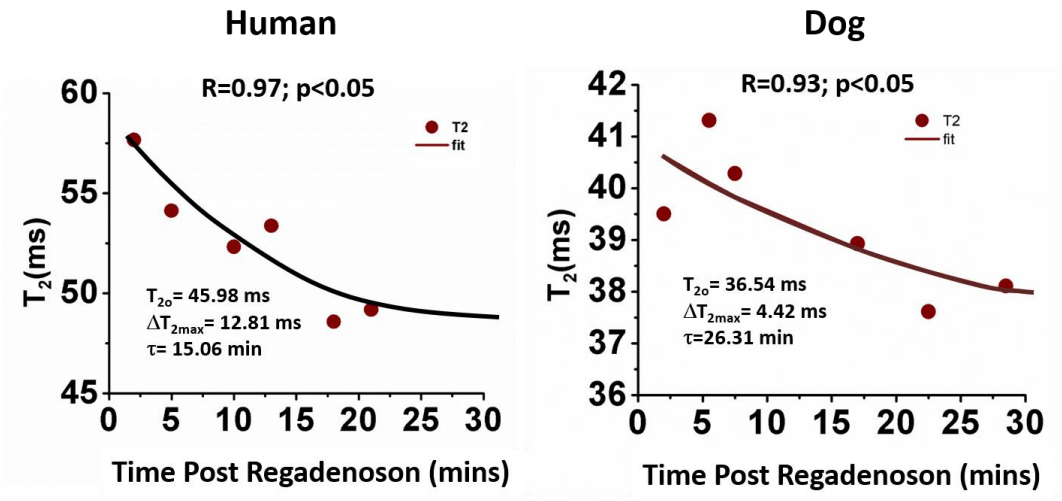

Fig. 4.9 Representative CDP curves of a human volunteer and a healthy dog. High R values present the good representation from the CDP model.

A representative set of temporal resolved BOLD signal and the fitted CDP curve from a healthy human subject and an intact dog is presented in Figure 4.9. Representative data showed high Pearson correlation (R) values to the exponential fit (Human: R=0.97, Dog: R=0.93). Fitted CDPs of the healthy studies are presented in table 1.

Parameters	T_{2o} (ms)	ΔT_{2max} (ms)	τ (min)	R	MBR_{CDP} (%)	MBR_{con}(%)
Dogs	34.6 ± 2.1	8.6±3.6	38.5 ± 28.0	0.97±0.06	25.8±9.2	10.1±3.4
Human	44.2 ± 6.7	14.7± 5.8	35.6 ± 28.8	0.92±0.02	26.5±16.1	12.0±5.4

Table 4 1 CDPs from humans and healthy animals. The fitted parameters are comparable between human and animal and are in the physiological range compare to the values reported in the literatures.

High R-values demonstrated the model is suitable to reports on the dynamics of the BOLD signal. CDPs are comparable between human and dogs and are in reasonable physiological

ranges (79,129). In addition, the mean MBR_{CDP} (ΔT_{2max} / T_{2o} x 100%) was significantly larger than the mean MBR_{con}, which indicates the recovered (magnified) BOLD sensitivity from the CDP extraction. The MBR_{CDP} correlated with the conventional single time point MBR with a linear regression model is shown in figure 10.

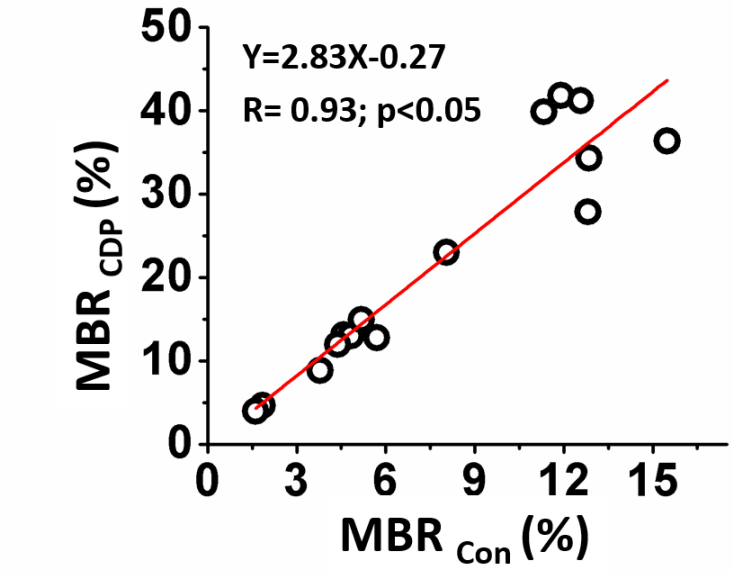

Fig. 4.10 Linear regression between MBR_{CDP} and MBR_{con}. The regression shows MBR_{CDP} is significantly correlated with the conventional MBR but the MBR_{CDP} shows significantly larger amplitude compared to MBR_{con}.

The MBR_{CDP} was strongly correlated with MBR_{con} (R=0.93; p<0.05). The regression also shows a slope significantly larger than 1 (Y=2.83X-0.27), which indicates the increased BOLD sensitivity with the extracted CDPs compared to the conventional approach.

4.2.3.2 Coronary Dynamics in an Animal with Myocardial Infarction

The masks of infarcted territories are first compared with ^{13}N -Ammonia PET to validate the perfusion deficit in the affected region.

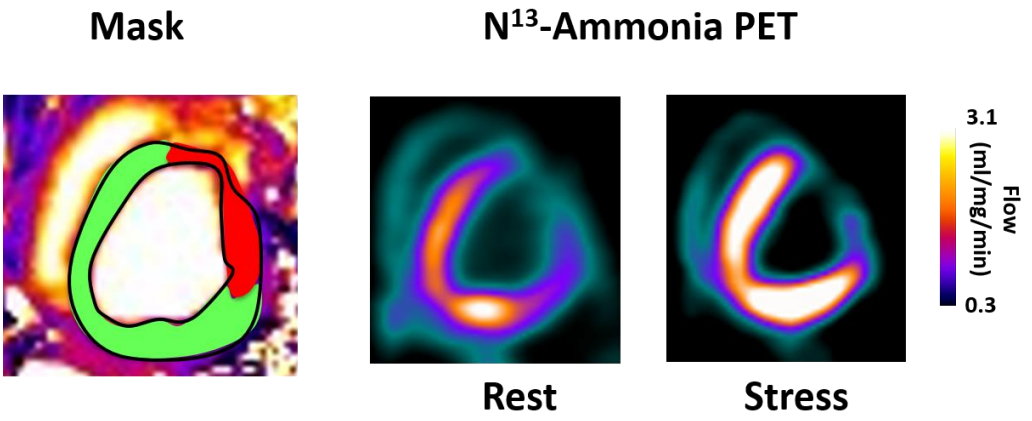

Fig. 4.11. Mask of the infarcted territory identified by LGE (red) and the corresponding ^{13}N -ammonia PET images. Excellent agreement between the infarcted territories and the perfusion deficit shows the reduced blood supply in the affected myocardium.

Fig. 4.11 presents strong spatial correspondence between infarcted territories from LGE and perfusion deficit from ^{13}N -Ammonia PET images. Both rest and stress myocardial blood flow were significantly reduced in the affected region and significant lower myocardial perfusion reserve was derived in the infarcted territories (MPR=1.9) compared to the remote myocardium (MPR=3.7). BOLD signal from the remote and affected regions were separated using the affected mask and fitted with the CDP model. The BOLD signal dynamic curve correspond to the remote and affected myocardium are presented in fig. 4.12.

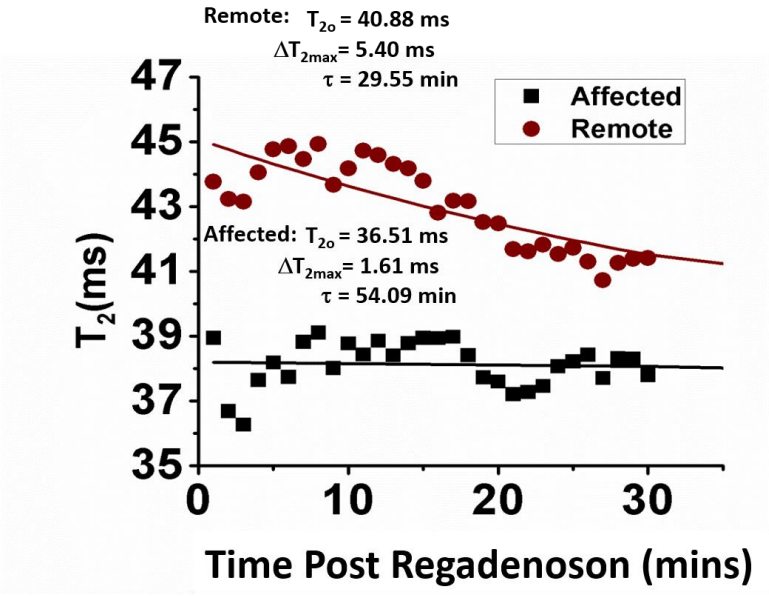

Fig 4.12 Representative BOLD signal dynamics curves extracted from the infarcted animal. Fitted curves are significantly different from remote and affected regions. Obvious reduction on ΔT_{2max} in the affected curve reflected the reduced perfusion reserve in the infarcted territory.

Remote and affected area showed significant differences in BOLD signal dynamics, particularly in the maximum T2 response (ΔT_{2max}) and coronary relaxation time constant (τ) (Remote: ΔT_{2max} =5.4ms, τ=29.6min vs. affected: ΔT_{2max} =1.6ms, τ=54.09min). Significantly lower maximal amplitude of vasodilation and longer relaxation time in the affected region demonstrated the abnormal coronary dynamics in the infarcted region.

CDPs were fitted with different starting time points to assess the effect of sampling after peak vasodilation and to optimize the capability to accurately assess disease. Representative curves fitted from 2, 5 and 10 minutes post-regadenoson injection are presented in fig 4.13.

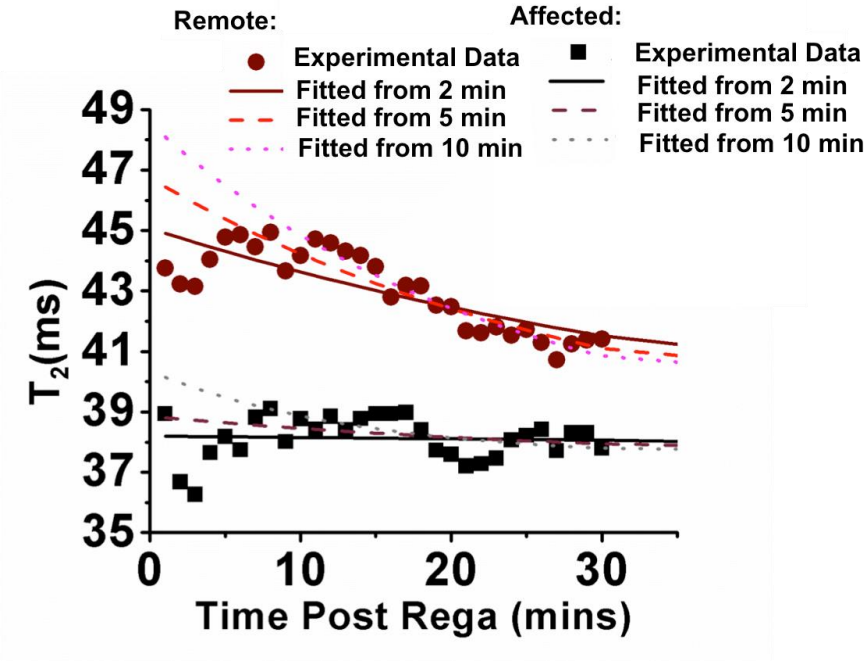

Fig. 4.13 Representative CDP curves fitted from different starting time points. Curves were fitted from BOLD sampled from remote (red) and affected (black) territories. The measured data are represented in circle and square and the fitted data are presented in lines.

Fig. 4.13 shows the fitted curves with different starting time points. While the curves shifted among different fitting conditions, the remote and affected curves were clearly separated in all fitted curves. The capability of the derived CDPs in separating the affected and remote myocardium was evaluated in segmental (fig.4.14) and pixel-wise (fig 4.15) fashion. The linear supporting vectors were presented in the CDP scatter plots (panel A-C) to investigate the seperability of the parameters and compared with the conventional single time point T2 values (panel D).

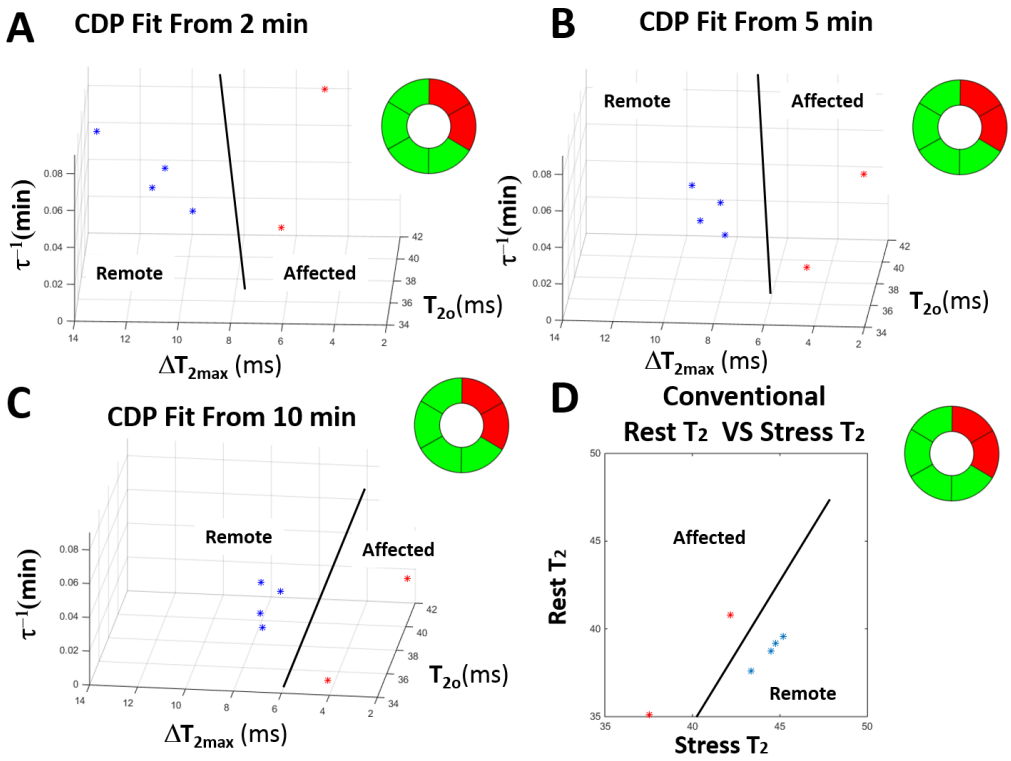

Fig 4.14 Segmental evaluation of the remote and affected territories. CDPs derived from different starting time points are plotted in the scatter plots(A-C) and labeled as remote (blue dots) and affected segments (red dots). Infarcted segments were successfully identified from all CDPs and T2 values. Larger margins from the derived SVM are shown in CDPs from 2 and 5 minutes compare to the 10 minutes and the conventional single time point approach.

Figure 4. 14 shows the segmental CDPs from an infarcted dog. CDPs fitted from starting 2min(A), 5min (B) and 10 min(C) post regadenoson administration are plotted with scatter plot and compared with conventional single time point BOLD signal (D). Affected segments identified from each parameter are labeled with polar plots and presented in the corresponding panel. All CDPs and conventional measures show the capability of separating the remote and affected segments. SVMs from each data sets were derived to investigate the separability between remote and affected segments. Post regadenoson measurement after 2min and 5 min CDPs showed greater margin from SVM compare to the conventional single time point

measurements. The effect demonstrated the possible increased sensitivity of disease identification with multiple measurement and coronary physiological information from the whole vasodilation period. Pixel-wise analysis from the same animal are presented in figure 4.15.

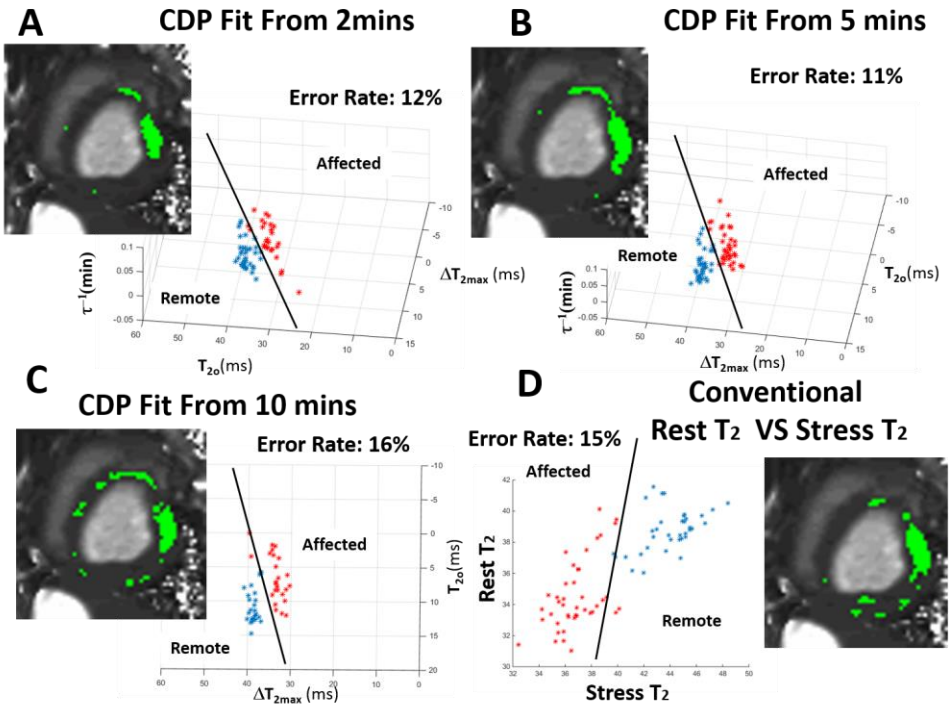

Fig 4.15. Pixel-wised evaluation of the remote and affected myocardium. CDPs derived from different starting time points (A:2min, B:5min and C:10 min) are plotted in the scatter plots and compared with the conventional single time point T2 values (D). The pixels are labeled as remote (blue dots) and affected (red dots) with different colors. Affected pixels identified by the averaged SVMs were displayed in the corresponding panel and highlighted with green. Lowest error rate and best accuracy on disease identification was achieved with the 5min CDPs.

Pixels from remote and affected area are clustered within each group in all CDP scatter plots. Averaged SVMs trained with 10-fold cross validation are presented in the plots and classification error rates were measured to assess the capability of classifying the affected pixels. The affected pixels detected by the averaged SVMs are also presented and highlighted (green) in each panel. CDPs fitted from 2 minutes and 5 minutes post regadenoson showed higher accuracy compared

to the conventional method while 10 minute CDPs presented slightly lower measures. Among all measurements, 5 mins CDPs showed the best classification property and lowest error rates in both segmental and pixel-wise analysis. In addition, acquiring stress images at a delayed time point is also favorable for providing more robust image quality as discussed in chapter 4.1, which enables a more sensitive and robust BOLD study.

4.2.4 DISCUSSION

In this study, coronary dynamics following regadenoson injection was assessed in dogs and humans with repeatedly acquired BOLD CMR. In healthy subjects, CDPs were extracted and the fitted parameters were closely correlated to the conventional single time point BOLD response. Maximum BOLD response extracted from CDPs showed the possible increased BOLD sensitivity relative to the conventional single time point MBR calculation. In the infracted dog, CDPs derived from 5 minutes post regadenoson showed the maximum capacity for classifying remote and affected myocardium in both segmental and pixel-wise analysis.

4.2.4.1 Increased Robustness of BOLD CMR with CDP Estimation

Reliability of BOLD images and the robustness of BOLD response are currently the key barriers for the clinical adoption of BOLD CMR. The capability to repeatedly sample the BOLD signal reduces the susceptibility to imaging and physiological noise compared to the standard single acquisition, which helps increase the robustness of the exams. This is enabled by the capability of regadenoson and is ideally suited for BOLD exam for two reasons: (A) due to the significant heart rate elevation and unstable cardiac motion at the initial phase (3-5min) (129) post injection,

imaging artifacts can significantly confound the BOLD signals. The capability of bypassing this unpredictable period with repeated measured BOLD CMR is ideal for extracting BOLD signal changes; and (B) The second phase of pharmacological half-life of regadenoson is ~30 minutes (130). The time scale is ideal for BOLD CMR acquisitions to sample the coronary activity post-regadenoson administration.

4.2.4.2 Valued-Added Benefits of Characterizing Coronary Dynamics

In the conventional stress exams, due to the limitation of perfusion imaging methods (typically aimed to capture the first-passage of the contrast agent), coronary reactivity (response) is only evaluated at a single time point (i.e., at peak vasodilation). Notably, the conventional noninvasive perfusion exams, such as SPECT, PET and first pass perfusion MRI, are usually based on imaging contrast agent dynamics. These approaches are not suitable for repeat measurements due to the dose of contrast agent, radiation and contrast washout speed. Although, peak MPR assessed with these methods provide important information in evaluating coronary function, a noninvasive way of determining the complete dynamics of the coronary arteries following regadenoson has the capacity to provide more information. For example, it provides the temporal dimension to study the actual condition of the coronary arteries, which is currently not available. Such a method can offer opportunities to assess time-dependent coronary relaxation and myocardial perfusion in patients experiencing coronary vasospasms.

We used a mono-exponential model as a first-order approximation to model the pharmacodynamics (128) of regadenoson mediating coronary relaxation. The extracted CDPs from the healthy subjects are in accordance with previously reported values (79) (131). In the animal with chronic MI, the CDPs were significantly different in the infarcted segments from the normal values. The difference showed the abnormal coronary reactivity in the affected

myocardium compared to the remote myocardium to be consistent with the expectation that there would be no or little dynamical response in a regions supplied by a culprit artery that caused an infarction.

4.2.4.3 Future directions

In this proof-of-concept study, BOLD images were acquired with a commercially available 2D T2 map, which is susceptible to the confounders as mentioned in the previous chapters. The 3D free-breathing HR independent sequence that was developed in earlier (Chapter 3) would be a desirable tool to rapidly acquire whole-heart BOLD signals and eliminate confounders from the vasodilatory stress.

Furthermore, the repeat measurement strategy can be used to further accelerate the imaging acquisition by exploring the temporal sparsity. While this study fitted the coronary dynamics with a mono-exponential model, a more sophisticated model (128) may provide an improved fitting for the BOLD signal dynamics. Although the current study showed the mono-exponential fit can capture sufficient differences in CDPs to differentiate remote and infarcted myocardial segments, the capability of the approach to identify non-flow limiting stensosis thatare clinically significant remains to be investigated.

4.2.5 CONLUSION

Repeatedly acquired BOLD CMR post regadenoson administration enables the extraction of coronary relaxation parameters and capture the BOLD response from peak vasodilation. CDP appear to have the capacity to reliably differentiate disease and healthy myocardium and have better tolerance for degraded image quality, hence improving the reliability of BOLD CMR.

Chapter 5 BOLD CMR with Hypercapnia

5.1 Arterial CO2 as a Potent Coronary Vasodilator

5.1.1 INTRODUCTION

A large number of studies have investigated the effect of carbon dioxide tension in arterial blood ($PaCO_2$) on myocardial blood flow (MBF) (132-141), but their conclusions on the sensitivity of CO_2 to invoke an increase in MBF has been variable. Specifically, studies have reported that an increase in $PaCO_2$ has marked (134,135), minimal (137,138) or no (133,139) effect on myocardial blood flow (MBF). These findings may be explained by one or more of the commonly shared aspects of these studies: (a) an indistinct stimulus due to the inability to independently, precisely and rapidly control $PaCO_2$; (b) confounding physiologic effects resulting from the use of isolated heart-lung or *in-situ* preparations; and (c) uncertain measures of the outcome variable due to limitations of the surrogate metrics of MBF.

If CO_2 were to be a powerful coronary vasodilator, it would have important scientific and clinical implications. For instance, in the absence of controlled levels of $PaCO_2$ the efficacy of novel experimental myocardial therapies may be confounded. Clinically, $PaCO_2$ may affect the results of invasive and non-invasive cardiac stress tests, coronary revascularization, and other procedures that depend on or wish to regulate MBF during intervention (142).

Our aim was to investigate the effects of $PaCO_2$ on MBF while minimizing contributions from factors that can unintentionally reduce or inaccurately report on sensitivity of $PaCO_2$ on MBF. To this end, we used a clinically relevant animal model along with (i) a validated strategy to

precisely and rapidly establish desired levels of $PaCO_2$, while holding PaO_2 constant; (ii) the gold-standard method for quantifying MBF in vivo; and (iii) validated image analysis platform to derive MBF values across the different coronary supply territories. We compared our findings to the effects of standard dose of adenosine in the same animal models with and without coronary stenosis to quantify MBF and flow deficit regions under peak tolerable $PaCO_2$. To determine whether the potential change in MBF in response to $PaCO_2$ overlaps the same mechanistic path as adenosine, we quantified MBF under hypercapnia and adenosine following caffeine administration – a substrate that is known to competitively inhibit the adenosine receptors affecting coronary artery resistance.

5.1.2 MATERIALS AND METHODS

5.1.3 Study Design

The objective of this study was to test whether physiologically acceptable hypercapnia can increase MBF to the same extent as adenosine – a well-known potent coronary vasodilator, which is routinely used in clinical cardiac stress testing (125). Previous investigations that aimed to examine the effect of elevated levels $PaCO_2$ on MBF have been limited by one or more methodological limitations. The current study overcomes these limitations through (a) prospective targeting of $P_{ET}CO_2$ to reach precise levels of $PaCO_2$ using a closed-loop gas-delivery system within 2-3 breaths while keeping PaO_2 fixed (143-145); (b) validated noninvasive imaging that is capable of reporting quantitative measures of MBF in vivo (146); (c) an accepted image analysis approach for quantifying MBF and related metrics (147); and (d) a clinically relevant animal model to investigate MBF under various physiological conditions (45). Prospectively targeted computerized control of end-tidal CO_2 ($PETCO_2$) method has evolved

into a reliable approach for fine, rapid and independent control of end-tidal partial pressures of CO_2 ($PETCO_2$) and O_2 ($PETO_2$) (143,144). Importantly, the $PETCO_2$ attained with prospective end-tidal targeting, is equal to $PaCO_2$ (144) —the independent variable with respect to vasoreactivity (143) which we investigated in this work. We used prospective end-tidal targeting to control $PaCO_2$ and ^{13}N-ammonia Positron Emission Tomography (PET) to measure of MBF, *in vivo* (142,148). We acquired cardiac images under rest, hypercapnia and following adenosine infusion in a clinically relevant canine model (149,150) with and without coronary stenosis. In the forthcoming text, we refer to $P_{ET}CO_2$ when referring to what was measured and $PaCO_2$ when referring to the vasoactive stimulus. We quantified MBF at each physiological condition using a validated image analysis approach (147). On the basis of changes in MBF in response to hypercapnia and adenosine, we quantified myocardial perfusion reserve (MPR, defined as ratio of MBF at stress (adenosine or hypercapnia) and MBF at rest). In canines with coronary stenosis, we quantified the relative volume of myocardial flow deficit under hypercapnia and adenosine. Specifically, first we examined whether the global and regional MBF and MPR are equivalent under conditions of hypercapnic stimulus ($P_{ET}CO_2$ ~ 60 mmHg) (45) and clinical dose of adenosine routinely used for cardiac stress testing (140 □g/kg/min) (125) in intact animals. Next, we examined regional changes in MBF and MPR under the same hypercapnic stimulus in animals subjected to coronary stenosis. Here we examined whether the total perfusion defects identified with hypercapnia are the same as with adenosine.

The mechanism mediating the observed hypercapnia-induced myocardial hyperemia from the above studies is not clear. However, the cellular and molecular pathways involved in adenosine-based coronary vasodilation are well understood (125). In the heart, increased levels of adenosine cause the extracellular A_{2A} receptors to initiate a set of cascading events that

ultimately converge on ATP-dependent K^+-dependent channels to relax vascular smooth muscles of the coronary arteries, thus leading to vasodilation. It is also known that caffeine is a potent nonselective competitive inhibitor of A_{2A} receptor and counteracts the downstream effects of adenosine (151). To investigate whether the mechanism of action of adenosine and hypercapnia are the same, we tested whether a known inhibitor of adenosine-mediated myocardial hyperemia, caffeine, can also abolish hyperemic MBF under hypercapnia (152). The institutional Animal Care and Use Committee approved all animal studies.

5.1.4 Animal Model & Preparation

Study Groups: Three groups of animals were studied: (a) Intact animals (*Group Intact*, n=10): In preparation for imaging studies, animals were fasted for 18 hours, sedated and anesthetized with propofol (2.0-5.0 mg/kg, IV) and intubated. (b) Animals with Coronary Stenosis (*Group Stenosis*, n=10): In addition to the above preparation, each animal was implanted with an occluder to implement stenosis of the left-anterior descending coronary (LAD), as previously described (45). (c) Pre-treatment of intact animals with caffeine (*Group Caffeine*, n=5): Animals were prepared as described above (*Group Intact*) but imaging was performed before and 10 minutes after caffeine administration (5 mg/kg, IV, chased by a 10 cc saline flush).

Anesthesia and Ventilation: All animals were transferred to the scanner table and were initially mechanically ventilated (Model 2002 Halowell EMC, MA, USA) with tidal volume 7-10 ml/kg, frequency 12-15/min, and inspiration to expiration ratio 1:2. A secondary sequential gas delivery circuit, functionally similar to that used for spontaneous ventilation was interposed between the animal and the ventilator to enable end-tidal prospective gas control. During end-tidal gas control, tidal volume was increased to 10-15 ml/kg and frequency to 15-20 /min to assure end-

tidal rebreathing. ECG, peripheral blood oxygenation (SpO_2), heart rate and blood pressure (diastolic, systolic and mean) were monitored. During the imaging studies, anesthesia was maintained with a continuous infusion of low dose propofol (0.03-0.1 mg/kg/min, IV).

Prospective Targeting of $PaCO_2$ and PaO_2: Prospective targeting of $PaCO_2$ and PaO_2 was accomplished using an algorithm-driven computerized gas blender administering gases to a sequential gas delivery breathing circuit (RespirAct™, Thornhill Research Inc., Toronto, Canada) as previously described (143). At rest and during adenosine infusion, $P_{ET}CO_2$ was targeted at ~35 mmHg and during hypercapnia $P_{ET}CO_2$ was targeted at ~60 mmHg, all while targeting isoxia at $P_{ET}O_2$ ~125mmHg.

Stenosis Studies: In *Group Stenosis*, imaging was performed within 2 minutes of establishing non-flow limiting stenosis at rest by ensuring that that occlusion did not lead to any visually evident ST-elevation at rest. In addition (a) first-pass perfusion MRI (153) at rest prior to release of occlusion at the terminal point of the study to determine flow abnormalities; (b) cine MRI to

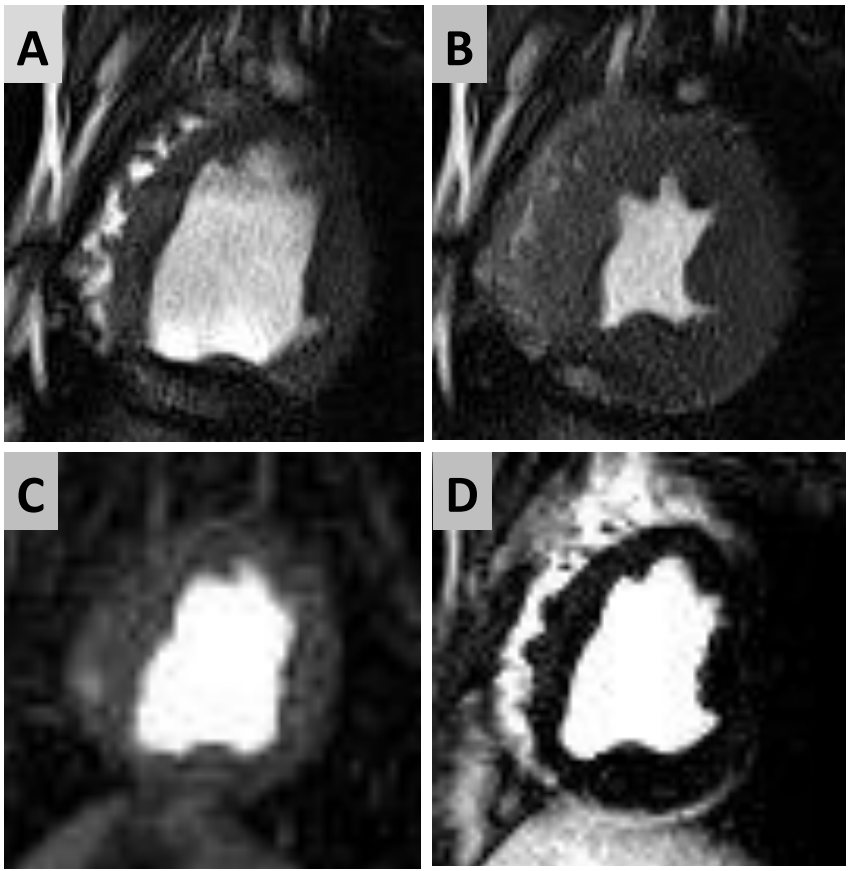

ascertain any wall motion abnormalities or edema (115); and (c) late-gadolinium enhancement MRI to rule out myocardial infarction. Fig 5.1 shows a representative case from the animals included as part of the Group Stenosis for analysis in which there was no evidence of rest perfusion anomalies or myocardial damage at rest at the terminal point of the studies.

Fig. 5.1 MRI-based validation of non-flow limiting stenosis. Balanced steady-state free-precession cine images were acquired in the presence of LAD stenosis at rest. End diastolic and systolic images from the cine series are shown in panels A and B. Note the absence of any wall motion or hyperintense regions (indicative of edema) in the anterior segments of the myocardial wall. Panels C and D show first-pass perfusion images at peak myocardial enhancement and late-gadolinium enhanced images obtained at rest, which show the absence of perfusion defects and infarction.

Two out of the 10 animals subjected to coronary stenosis, showed evidence of rest perfusion defects and mild sub-endocardial evidence of late-gadolinium enhancement in the anterior lateral wall and were excluded from further analysis. Thus, a total of 8 animals from *Group Stenosis* were analyzed.

5.1.5 Noninvasive Assessment of MBF with ^{13}N PET

All PET images were acquired using a whole body clinical Biograph mMR (Siemens Healthcare, Erlangen, Germany) in 3-dimensional (3D) list mode using ^{13}N-ammonia (200 MBq, IV bolus (3-5 s) followed by 10 cc saline flush) as the blood flow tracer. Prior to each PET scan, magnetic resonance images were acquired to correct for photon attenuation. Attenuation correction was performed using segmentation of images obtained with a 2-point Dixon MR imaging pulse sequence, which has been shown to be effective for cardiac studies in both humans and canines (116,117). Data acquisition spanned over 10 minutes and began a few seconds before the ^{13}N-ammonia injection. In *Group Intact*, images were acquired during hypercapnia and adenosine infusion at rest to investigate the MBF response in the absence of

coronary stenosis. Specifically, under adenosine, PET acquisitions were prescribed following 2 minutes of adenosine infusion; and under hypercapnia, 1 minute after the desired $P_{ET}CO_2$ value was reached. A time delay was introduced between the sequential PET acquisitions at each physiological condition to ensure sufficient decay of each ^{13}N-ammonia dose (5 half-lives, ~50 minutes). In *Group Stenosis*, images were acquired at rest, hypercapnia and adenosine before and after infliction of LAD coronary stenosis. In *Group Caffeine*, rest scans were acquired pre- and post-caffeine treatment. This was followed by post-caffeine treatment scans under hypercapnia and adenosine. Other aspects of the imaging protocols implemented in *Group Stenosis* and *Group Caffeine* were similar to that implemented in *Group Intact*. In all animal groups, the order of adenosine and hypercapnia stimulations was randomized and the animals were allowed to recover to baseline $P_{ET}CO_2$ between the protocols. A schematic representation of the sequential execution of the study protocols in the three different groups of animals is provided in Fig. 5.2.

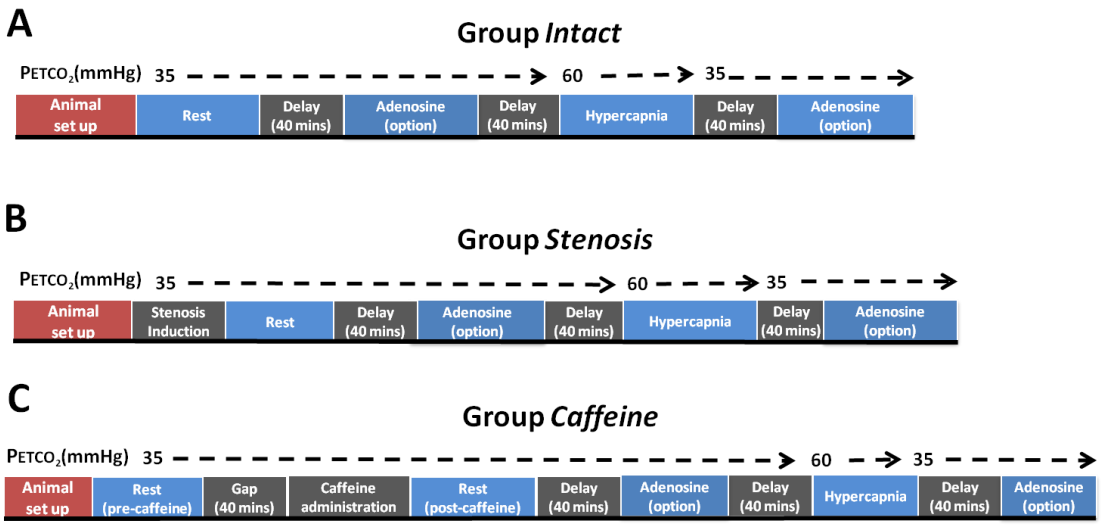

Fig. 5.2 Chronological order of 13N-ammonia PET data collection in Group intact (A), Group Stenosis (B) and Group Caffeine (C). PETCO2 at the different points of imaging are shown over the blocks. PETCO2 was held constant as described in text. In all studies, adenosine and hypercapnia were

randomized ("Adenosine (option)" denotes that PET images were acquired before or after hypercapnia, but only once). A 40-minutes delay was introduced between acquisitions to ensure sufficient decay of the radiotracer between acquisitions. In Group Stenosis, LAD stenosis was induced as described in text with additional MRI scans performed at the very end (not shown) to ensure absence of rest flow defects, myocardial stunning or infarction. In Group Caffeine, pre- and post-caffeine rest exams were performed in the order as described and the PET acquisitions under adenosine and hypercapnia were performed post-caffeine and the order was randomized.

5.1.6 PET Reconstruction and Quantifications of MBF and MPR

An experienced technologist verified the registration of the MRI attenuation map with the PET images visually, and alignment was corrected if necessary by manual 3D translation. Sixteen dynamic PET frames were reconstructed (twelve 10-s, two 30-s, one 1-min, and one 6-min frames, for a total of 10 min). Standard reconstruction (2-dimensional attenuation-weighted ordered-subsets expectation maximization) was used with 3 iterations and 14 subsets and 3D post filtering with a 5-mm Gaussian kernel (154). Transverse data were reformatted to a 168 x 168 x 47 matrix with 2-mm pixels for each dynamic frame. Late perfusion images were reconstructed using 7 min of the acquisition after a 2-min delay to allow for blood-pool clearance. The reconstruction parameters were identical to the dynamic reconstruction.

Global and regional myocardial blood flow (MBF) values in ml/min/g and myocardial perfusion reserve (MPR) values were derived automatically from the PET data using the automated QPET software (Cedars-Sinai Medical Center, Los Angeles, CA, USA), as described previously (154). Left ventricular contours were determined automatically from summed dynamic image data, discounting the first 2 min. The region for the left ventricular input function was derived automatically by placing a cylindrical region of interest (1-cm radius and 2-cm length) with its vertical-axis oriented along the long-axis of the heart and centered in the middle of the valve

plane. An expert reader reviewed the left ventricular contours and placement of region-of-interest to determine the arterial input function. Dynamic myocardial samples were obtained from the polar map, by analyzing all time frames within the fixed left ventricular contour boundaries. Using a standard 2-compartment kinetic model for ^{13}N-ammonia, stress and rest flow values in ml/min/g were computed for each sample on the polar map as previously described (119). MPR was computed as a ratio, by dividing each stress polar map sample by the corresponding rest sample at each point. The MPR values were corrected by adjusting the resting flow by the resting rate-pressure product, following standard processing technique, in QPET. The global MBF at stress and rest was computed within the whole LV region bounded by the LV plane. The regional MPR was then obtained by dividing the polar map into three regions (left anterior descending artery (LAD), left circumflex coronary artery (LCx), and right coronary artery (RCA)) using the 17-segment model of the American Heart Association. Regional and global MPR values were extracted automatically for further analysis.

5.1.7 Quantification of Total Reduction in Perfusion Volume

Myocardial perfusion defect territory of *Group Stenosis* was measured using the stress-rest change analysis in QPET software (154,155). In the analysis, perfusion images from both provocative stresses were registered to the rest images using the short-axis images; a 2-pass registration algorithm was used to minimize the overcompensation between rest and stress (155). Subsequently, the "stress-rest" perfusion difference was derived from the voxels contained within the stress contour volume. The count differences between the stimulations were then divided by the total rest counts, resulting in a relative count change measure, which was defined

as the measure of perfusion difference between stress and rest, as previously demonstrated (155). Total reduction in myocardial perfusion volume was derived as a fraction of the total LV myocardial volume (TRP, %LV).

5.1.8 Statistical Analysis

All statistical analyses were performed in IBM SPSS (V21.0, NY, USA). Statistical significance was established for $p<0.05$. All results are reported as mean ± standard deviation (SD). In all studies (*Group Intact*, *Group Stenosis* and *Group Caffeine*), two-way repeated measurement ANOVA tests were used to examine the regional MBF and MPR in response to hypercapnia and adenosine. Two factors were set to be the regional coronary territories (LAD, LCx and RCA) and the physiological states (MBF: rest, hypercapnia, adenosine; MPR: hypercapnia, adenosine). One-way repeated measurement ANOVA tests were used to examine the differences of Global MBF (rest, hypercapnia and adenosine) and hemodynamic indices (heart rate, blood pressure, and rate-pressure product). For both tests, post-hoc comparison with Bonferroni correction was used to examine if the null hypothesis was rejected. Global MPR from all studies and TRP between hypercapnia and adenosine were compared using paired t test. An equivalence test was performed with a confidence interval of 90% to determine whether the global MBF was different under adenosine and hypercapnia in *Group Intact*; the same was performed for global MPR. Linear correlation analyses were performed between hypercapnia and adenosine in all studies to compare regional MBF, regional MPR and TRP. Bland-Altman analysis was also performed to determine the limits of agreement and bias between hypercapnia and adenosine. All results are shown as mean ± SD.

5.1.9 RESULTS

5.1.9.1 Hypercapnia can induce more than a 2-fold increase in myocardial blood flow

We acquired cardiac PET images in intact canines (Group Intact, n=10) under rest ($P_{ET}CO_2$ ~ 35 mmHg), at peak hypercapnia ($P_{ET}CO_2$ ~ 60 mmHg) (45,156) and 2-3 minutes following standard adenosine infusion (140 μg/kg/min) (157) while holding $PETO_2$ relatively constant ($PETO_2$ ~ 125 mmHg). We quantified global and regional MBF and MPR from the PET images. Table 1 summarizes the measured mean arterial CO_2, O_2 and hemodynamic variables of interest in Group Intact. The results are shown in Fig. 5.3 and mean global and regional MBF and MPR are tabulated in Table 5.1.

Group Intact (n=10)	**$P_{ET}CO_2$ (mmHg)**	**$P_{ET}O_2$ (mmHg)**	**SBP (mmHg)**	**HR (per min)**	**RPP (mmHg/minx10^3)**

Adenosine	37.5 ± 2.9	119.9±7.0	128.6 ± 16.8	99.6 ± 34.7*	12.3 ± 4.9*
Hypercapnia	60.6 ± 1.4*	121.3±5.8	130.2 ± 14.3	81.8 ± 16.8	10.9 ± 2.4
Rest	36.9 ± 1.6	118.3±5.2	121.2±12.1	65.4 ± 15.2	8.2 ± 2.3
Group Stenosis (n=7)	$PaCO_2$ (mmHg)	PaO_2 (mmHg)	SBP (mmHg)	HR (per min)	RPP (mmHg/minx10^3)
Adenosine	37.3 ± 2.4	128.0 ± 4.9	111.8 ± 32.1	120.8 ± 26.9*	13.9 ± 6.1*
Hypercapnia	60.6 ± 1.2*	123.7 ± 5.6	118.2 ± 25.3	101.2 ± 23.0	12.0 ± 5.2*
Rest	35.9 ± 3.4	126.0 ± 4.5	118.1 ± 30.7	73.4 ± 17.0	8.9 ± 2.9
Group Caffeine (n=5)	$PaCO_2$ (mmHg)	PaO_2 (mmHg)	SBP (mmHg)	HR (per min)	RPP (mmHg/minx10^3)
Adenosine	35.1 ± 0.6	123.7 ± 3.0	125.8 ± 8.0	65.4 ± 29.9	6.9 ± 1.7
Hypercapnia	59.9 ± 2.3*	128.9 ± 6.8	128.3 ± 11.6	69.8 ± 10.8	9.3 ± 3.6
Rest	34.5 ± 1.2	125 ± 3.6	124.0 ± 11.2	56.6 ± 23.2	7.1 ± 4.0

Table 5.1 Targeted arterial blood gas estimates and hemodynamic parameters

*SBP: Systolic Arterial Blood Pressure; HR: Heart Rate; and RPP: Rate Pressure Product (MAP x HR). *denotes statistically significant difference within the hemodynamic or vital indexes compared to values at rest.*

Representative peak myocardial uptake (short- and long-axis), dynamic myocardial uptake curves and polar maps of MBF under rest and stress (hypercapnia and adenosine) along with corresponding MPR are shown in Fig. 5.3 A, B and C. An increase in myocardial uptake of the tracer, MBF and MPR were evident between rest and hypercapnia and were similar to those observed with adenosine.

Mean global and regional (classified according to supply territories of left-anterior descending (LAD), left-circumflex (LCx), and right (RCA) coronary arteries) MBF under hypercapnia and adenosine showed marked increases compared to rest (Fig. 5.3D). Global MBF under adenosine and hypercapnia were both significantly higher than at rest ($p<0.05$, for both) and were not different from one another ($p=0.33$). Global MBF increase in response to adenosine and hypercapnia were found to be equivalent with a margin of equivalence of 0.26 ml/min/g (1/3 of the standard deviation of the difference in MBF, 0.8 ml/min/g) at $\square = 0.05$. Global MBF normalized by rate-pressure-product under adenosine ($1.16 \times 10^{-5} \pm 0.80 \times 10^{-5}$) and hypercapnia ($1.26 \times 10^{-5} \pm 0.56 \times 10^{-5}$) were significantly different from rest ($0.67 \times 10^{-5} \pm 0.33 \times 10^{-5}$, $p<0.05$ for both), but were not different from one another ($p=1.00$). Regional MBF under adenosine and hypercapnia were significantly higher than at rest but were not different from one another ($p>0.8$, for all). Collective comparison of regional MBFs between hypercapnia and adenosine were positively correlated ($R=0.73$, $p<0.05$) and showed good agreement (bias of 0.19 ml/g/min, Fig. 5.3E).

Mean global MPR with adenosine and hypercapnia were significantly greater than 2 and were found to be equivalent with a margin of equivalence of 0.50 (1/3 of the standard deviation of the difference in MPR, 1.54) at $\square = 0.05$. Similar observations were evident for regional MPR with hypercapnia and adenosine with $p<0.05$ for all territories. The MPRs in the respective territories did not differ under hypercapnia and adenosine ($p=1.00$, for all comparisons; Fig. 5.3F). Comparison between regional MPR under adenosine and hypercapnia showed significant correlation ($R = 0.75$, $p<0.05$) and good agreement with a bias of 0.35 (Fig. 5.3G).

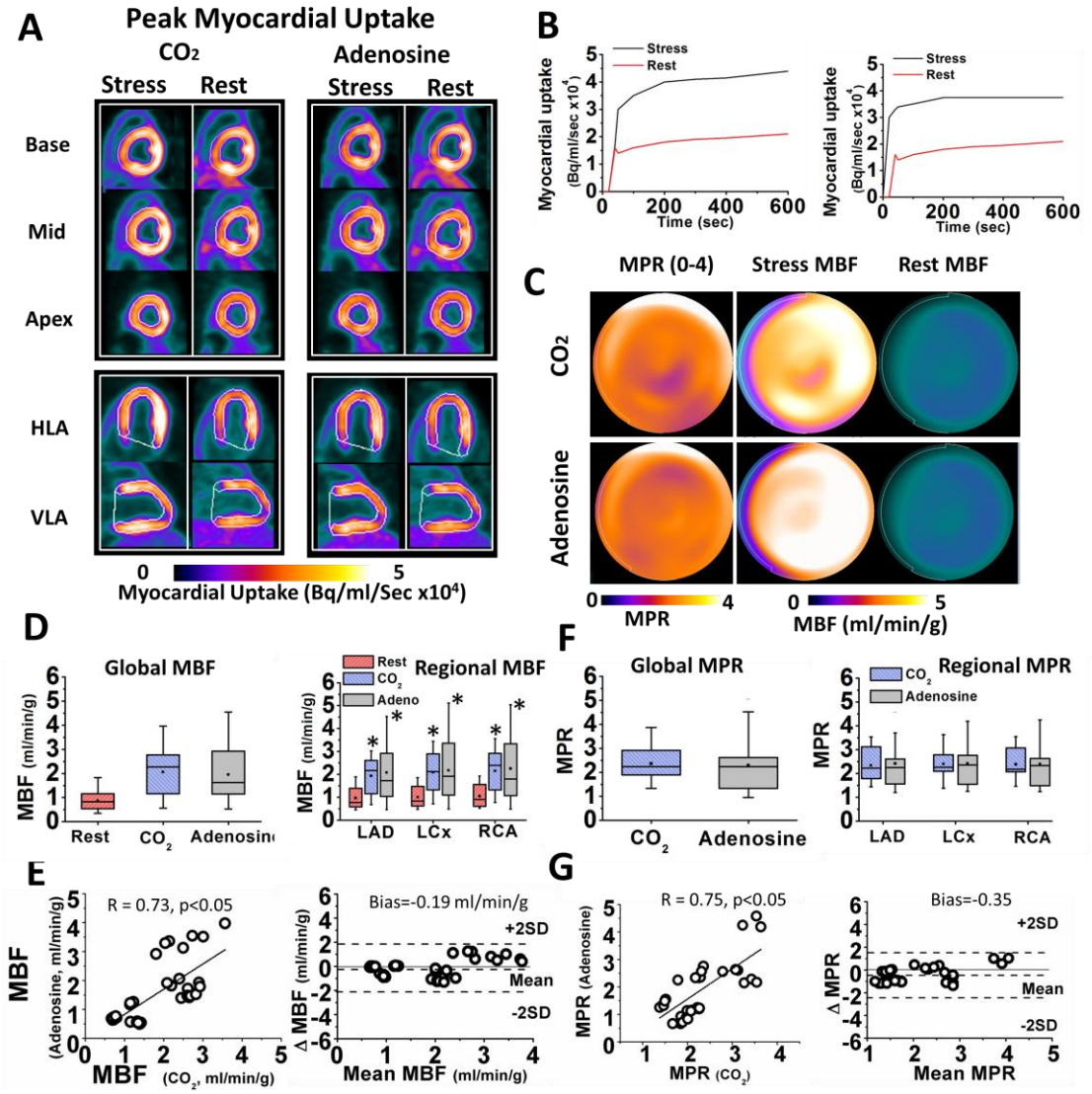

Figure 5.3.Global and Regional Myocardial Blood Flow Response to Hypercapnia and Adenosine in Intact Canines. Panel A shows representative short- (Base, Mid, Apex) and long-axis (horizontal (HLA) and vertical (VLA)) PET images of peak myocardial uptake of 13N-ammonia during hypercapnia of PaCO2 ~ 60 mmHg (CO2), standard clinical dose of adenosine infusion (Adenosine) and under baseline conditions with PaCO2 ~ 35 mmHg (Rest). These visual results show the increase in myocardial uptake of radiotracer relative to rest under hypercapnia and adenosine. Panel B shows the corresponding dynamic radiotracer uptake curves, which further verify the increased myocardial uptake responses to hypercapnia and adenosine stresses relative to rest. Panel C shows the corresponding Myocardial Perfusion Reserves (MPRs) under hypercapnia and adenosine (for the case in panels A and B) as well as myocardial blood flow (MBF) as polar maps. Panel D shows the global and regional mean MBF at rest and under hypercapnia and adenosine. In both cases, MBFs were significantly higher during hypercapnia

*and adenosine compared to rest. No significant differences in regional MBFs were observed between the different coronary supply territories. Panel E shows the correlation (linear regression) and agreement (Bland-Altman plots) between regional MBF under adenosine and hypercapnia. Both regression and Bland-Altman analyses showed good correlation ($R=0.73$, $p<0.05$) and agreement (bias= -0.19 ml/min/g) in regional MBFs under the two different stresses. Panel F and G show similar analyses of MPR under hypercapnia and adenosine. No differences in global or regional MPR differences were observed between hypercapnia and adenosine. Good regional MPR correlations ($R=0.75$, $p<0.05$) and good agreement (bias = -0.35) were observed between respective regional responses to hypercapnia and adenosine. * denotes $p<0.05$.*

The observed range of MBF at rest (0.44 ml/min/g to 1.93 ml/min/g) and adenosine (0.47 ml/min/g to 5.10 ml/min/g) and range of MPR under adenosine (1.20 to 4.57) across the animals is consistent with previous reports (149,150). We conclude that an increase in arterial $PaCO_2$ of 25 mmHg can increase MBF more than 2-fold in all myocardial territories subtended by fully patent coronary arteries, which is a hallmark of all clinically meaningful vasodilators (158). Notably, we found that such an increase in MBF is not different from that is observed with intravenously administered adenosine and is not attributable to changes in myocardial oxygen consumption (work) indexed by rate-pressure product.

5.1.9.2 Hypercapnia can be used to identify regional impairments in MBF and MPR due to coronary artery stenosis

To determine whether myocardial territories supplied by stenotic coronary arteries can be identified under hypercapnia, we studied canines (Group Stenosis, n=8) subjected to LAD coronary stenosis under hypercapnia and adenosine infusion with ^{13}N-ammonia PET. Table 1 summarizes the estimates of mean arterial CO_2, O_2 and hemodynamic variables of interest in

Group Stenosis. Results are shown in Fig. 5.4 and mean global and regional MBF and MPR are tabulated in Table 5.2. Global and regional MBF and MPR values obtained from ^{13}N-ammonia PET images from the different groups of animals under various physiological statuses are shown in Table 5.2 (Group Intact), 5.3 (Group Stenosis) and 5.4 (Group Caffeine). The results are shown as mean ± SD.

MBF	**Regional (ml/min/g)**		
	LAD	LCx	RCA
Adenosine	1.4±0.6	2.3±1.0	2.7±1.1
Hypercapnia	1.4±0.3	2.2±1.0	2.5±1.1
Rest	0.6±0.1	0.5±0.1	0.6±0.1
MPR	**Regional**		
	LAD	LCx	RCA
Adenosine	2.2±0.6	3.8±1.4	4.7±1.4
Hypercapnia	2.1±0.5	3.8±1.3	4.2±1.6

Table 5.2: *Global and Regional MBF and MPR in Group Intact*

Representative short- and long-axis peak myocardial uptake images and polar maps of MBF and MPR from an animal with LAD stenosis obtained at rest ($PETCO_2$ ~ 35 mmHg) and the two

different states of stress (hypercapnia ($PETCO_2$ ~ 60 mmHg) and adenosine) are shown in Fig. 5.4 A, B and C. Rest/stress images and MPR maps under hypercapnia and adenosine were visually highly concordant. Notably, decreased peak myocardial uptake and MPR were evident only in the anterior lateral wall of the myocardium (consistent with the supply territory of distal LAD coronary artery).

Mean regional MBF in LAD, LCx and RCA supply territories at rest, hypercapnia and adenosine are shown in Fig. 5.4D. MBF values were not different at rest among the different supply territories ($p>0.4$, for all). MBF increased under hypercapnia and adenosine ($p<0.05$, for all territories), albeit the increase in the LAD territory was significantly lower than in the LCx and RCA territories (with hypercapnia and adenosine; both $p<0.05$). However, MBF under hypercapnia was not different between the LCx and RCA territories (hypercapnia: $p=0.21$); the same was true under adenosine ($p= 0.50$). For each myocardial supply territory, MBF under hypercapnia and adenosine were not different ($p=1.00$, for all). Collective comparisons of regional MBF between hypercapnia and adenosine showed significant correlation ($R=0.69$, $p<0.05$) and good agreement with a bias of 0.41 ml/min/g (Fig. 5.4E).

Mean regional MPR under hypercapnia and adenosine for LAD, LCx and RCA are shown in Fig. 5.4F. MPR values were not higher than 2.0 in LAD territories (hypercapnia: $p=0.48$ and adenosine: $p=0.52$) but were significantly higher than 2.0 in the LCx and RCA ($p<0.05$ for hypercapnia and adenosine) territories. MPR under hypercapnia was not different between the LCx and RCA territories (hypercapnia: $p=0.59$); the same was true under adenosine ($p = 0.34$). For each myocardial supply territory, MPR under hypercapnia and adenosine were not different ($p>0.5$ for all). Collective comparisons of regional MPR between hypercapnia and

adenosine showed significant correlation (R=0.71, p<0.05) and good agreement with a bias of 0.21 (Fig. 5.4G).

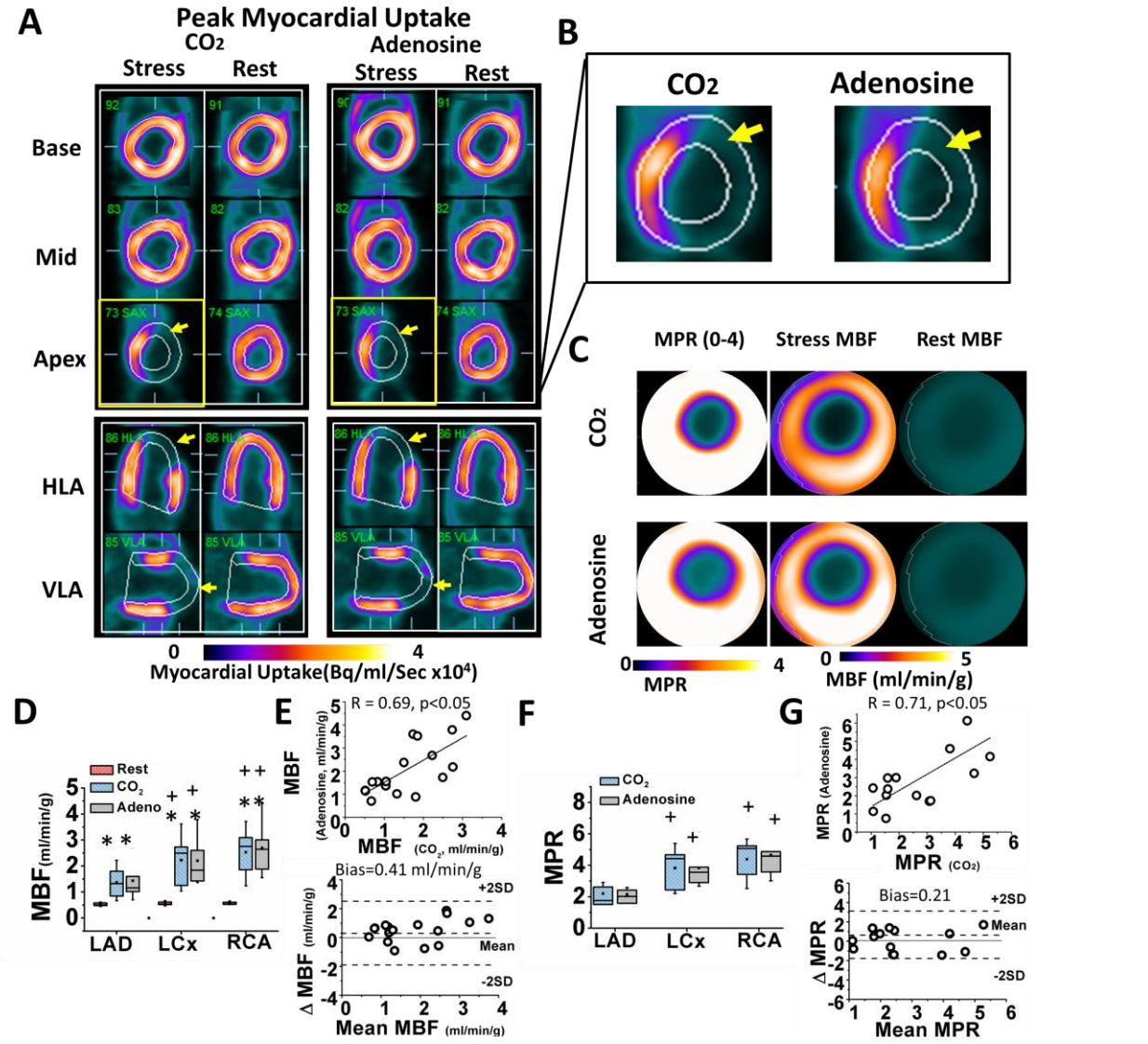

Figure 5.4. Regional Myocardial Blood Flow Response to Hypercapnia and Adenosine in the Presence of Coronary Stenosis. Panel A shows representative short- (Base, Mid, Apex) and long-axis (HLA and VLA) PET images of peak myocardial uptake of 13N-ammonia during hypercapnia of PaCO2 ~ 60 mmHg (CO2), standard clinical dose of adenosine (Adenosine) and at rest with PaCO2 ~ 35 mmHg (Rest) in a canine with a coronary stenosis of the LAD. Note the differentially lower uptake of the radiotracer in the

*anterior lateral wall (as evidenced by the lower signal in myocardial segments supplied by the distal LAD, yellow arrows) under hypercapnia and adenosine. For ease of visualization, reduced tracer uptake in the LAD territory during peak uptake in remote regions (i.e., those not impaired by coronary stenosis) is highlighted in the zoomed-in apical short-axis image under hypercapnia and adenosine in panel B. For the case in panel A, rest and stress MBF (under hypercapnia and adenosine) and corresponding MPR are shown as polar maps in panel C. These images show marked preferential reduction in MBF and MPR in the supply regions of the LAD, which are visually evident and spatially consistent under hypercapnia and adenosine. Panel D shows mean regional MBF at rest, hypercapnia and adenosine. MBF across all coronary supply territories were higher relative to rest under adenosine and hypercapnia but the MBF under hypercapnia and adenosine were significantly higher in the RCA and LCx territories relative to LAD. Regional MBF under hypercapnia and adenosine showed significant positive correlation ($R=0.65$, $p<0.05$) and agreement (0.41 ml/min/g). Panels F and G show similar analyses of regional MPR under hypercapnia and adenosine. No differences in regional MPR were observed between hypercapnia and adenosine but significant differences in MPR between LAD and other territories (RCA and LCx) were observed. Significant positive regional MPR correlations ($R=0.71$, $p<0.05$) and good agreement (bias = 0.21) were observed between respective regional responses to hypercapnia and adenosine. * denotes $p<0.05$ compared to conditions of rest; and +denotes $p<0.05$ compared to LAD under stress.*

Our findings here suggest that myocardial territories supplied by a stenotic coronary artery can be identified using a hypercapnic stimulus ($PaCO_2$ ~ 60 mmHg) as well as adenosine on the basis of reduced MBF and MPR.

MBF	Global	Regional **(ml/min/g)**		
	(ml/min/g)	LAD	LCx	RCA
Adenosine	2.2±1.1	2.1±0.7	2.2±0.9	2.2±0.9
Hypercapnia	2.1±0.9	1.9±1.3	2.1±1.4	2.2±1.4
Rest	0.9±0.4	0.9±0.5	0.9±0.4	0.9±0.4
MPR	**Global**	**Regional**		
		LAD	LCx	RCA

Adenosine	2.3±1.0	2.3±0.9	2.4±0.9	2.3±0.9
Hypercapnia	2.6±0.7	2.6±0.9	2.6±1.1	2.6±0.8

Table 5.3: Global and Regional MBF and MPR in Group Stenosis

5.1.9.3 Perfusion defect volumes determined with hypercapnia and adenosine are equivalent

We examined whether hypercapnic stimulus of 25 mmHg can be used to accurately quantify the volume of perfusion defect on the basis of PET in the presence of a coronary stenosis. The total reduction in perfusion volume (TRP, %LV) as a percentage of total LV volume between stress and rest states using a validated approach (155) is shown in Fig. 5.5.

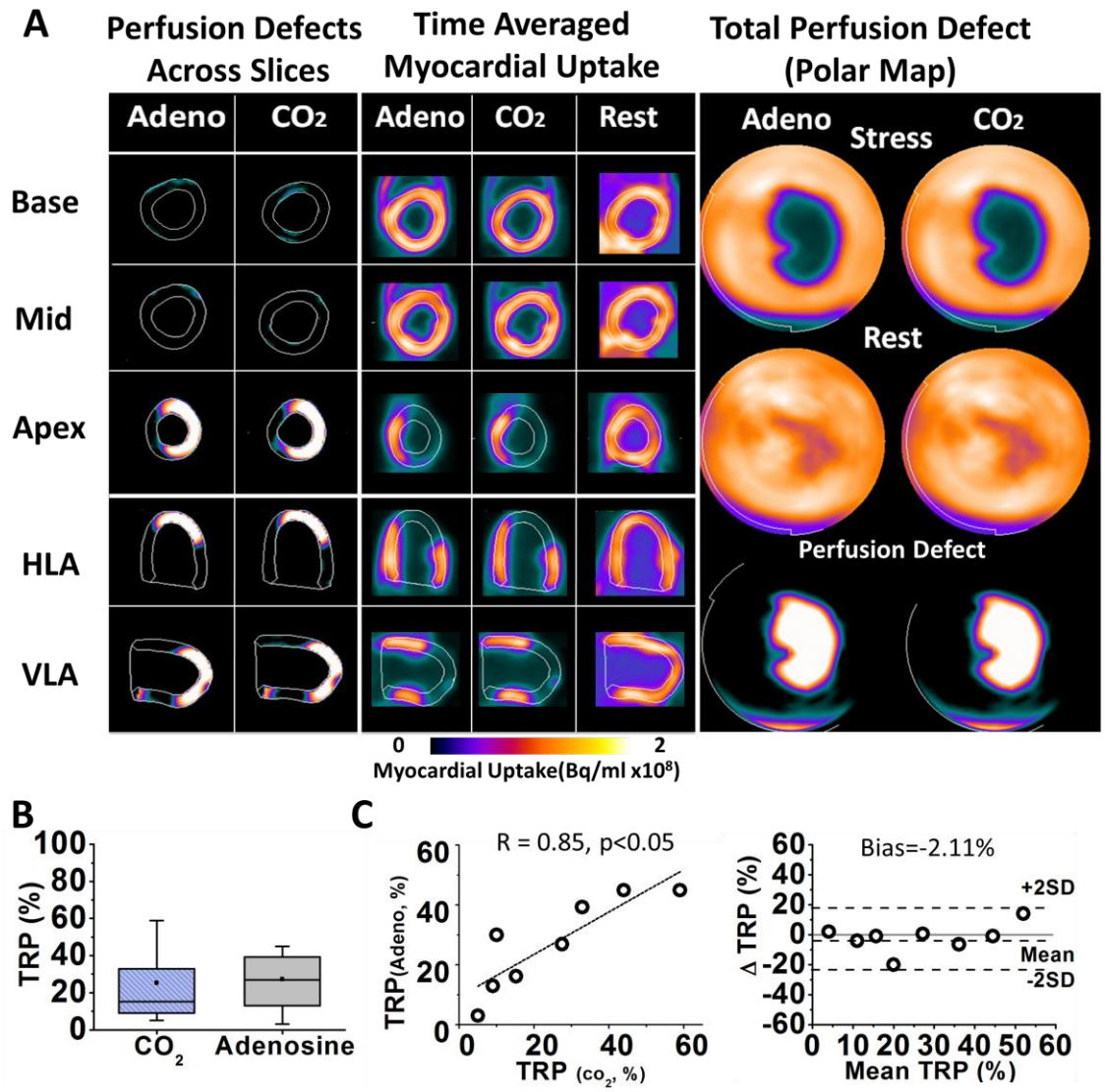

Figure 5.5. Total Myocardial Perfusion Defect Due to Coronary Stenosis Under Hypercapnia and Adenosine. Panel A shows representative short- (Base, Mid, Apex) and long-axis (HLA, VLA) PET images with perfusion defects from the Change Analysis (left) estimated from time-averaged myocardial uptake images (middle) at rest and stress (hypercapnia and adenosine), along with polar images highlighting total perfusion defects (right), for the representative case in Figure 5.4. Note the near identical correspondence in the perfusion defect territories identified in the slices and the whole heart identified under conditions of hypercapnia and adenosine stress. Panel B shows the mean TRP (%LV) under hypercapnia and adenosine. No significant difference in TRP (%LV) was observed under hypercapnia and adenosine. Panel C shows results from linear regression and Bland-Altman analyses.

Significantly high positive correlation (R=0.85, p<0.05) and minor bias (-2.11%) in TRP (%LV) was observed between hypercapnia and adenosine.

Representative images from the change analysis for the LAD stenosis case in Fig. 5.4A is shown in Fig. 5.5A. Perfusion defect regions visually identifiable in the short- and long-axis images along with total perfusion defect regions captured by the polar maps show that the perfusion defect is confined to the lateral wall, which is consistent with LAD stenosis. Mean TRP obtained under hypercapnia and adenosine were not different: 25±19% (hypercapnia) vs. 27±15 % (adenosine); p = 0.12. Direct comparison of TRP within the same subjects under hypercapnia and adenosine were significantly correlated (R=0.85, p<0.05) and were in good agreement with a bias in TRP of 2% (Fig. 5.5C). These findings demonstrate that a hypercapnic stimulus ($PETCO_2$ ~ 60 mmHg) can be used to determine the same spatial extent of myocardial perfusion defect typically assessed with adenosine stress.

5.1.9.4 Caffeine treatment abolishes myocardial hyperemia under adenosine but not hypercapnia

The results are shown in Fig. 5.6 and mean global and regional MBF and MPR tabulated in Table 5.4.

MBF	Global (ml/min/g)	Regional **(ml/min/g)**		
		LAD	LCx	RCA
Adenosine	0.6±0.2	0.5±0.1	0.6±0.2	0.6±0.2
Hypercapnia	0.9±0.2	0.8±0.2	0.9±0.3	1.0±0.2
Rest (post treatment)	0.6±0.2	0.5±0.2	0.6±0.3	0.6±0.3
Rest (pre treatment)	0.8±0.4	0.8±0.4	0.8±0.4	0.9±0.4
MPR	**Global** (ml/min/g)	**Regional** (ml/min/g)		
		LAD	LCx	RCA
Adenosine	1.1±0.6	1.1±0.1	1.1±0.2	1.1±0.1
Hypercapnia	1.8±0.2	1.7±0.6	1.8±0.8	1.8±0.7

Table 5.4: Global and Regional MBF and MPR in Group Caffeine

Representative short- and long-axis peak myocardial uptake images at rest ($PETCO_2$ ~ 35 mmHg), hypercapnia ($PETCO_2$ ~ 60 mmHg) and adenosine (140 □g/kg/min) in a canine treated with caffeine (5 mg/kg) are shown in Fig. 5.6A. The corresponding MBF and MPR values are shown as polar maps (Fig. 5.6B). These results show that in this animal treated with caffeine, although there is no change in MBF between rest and adenosine, hypercapnia is still able to induce myocardial hyperemia.

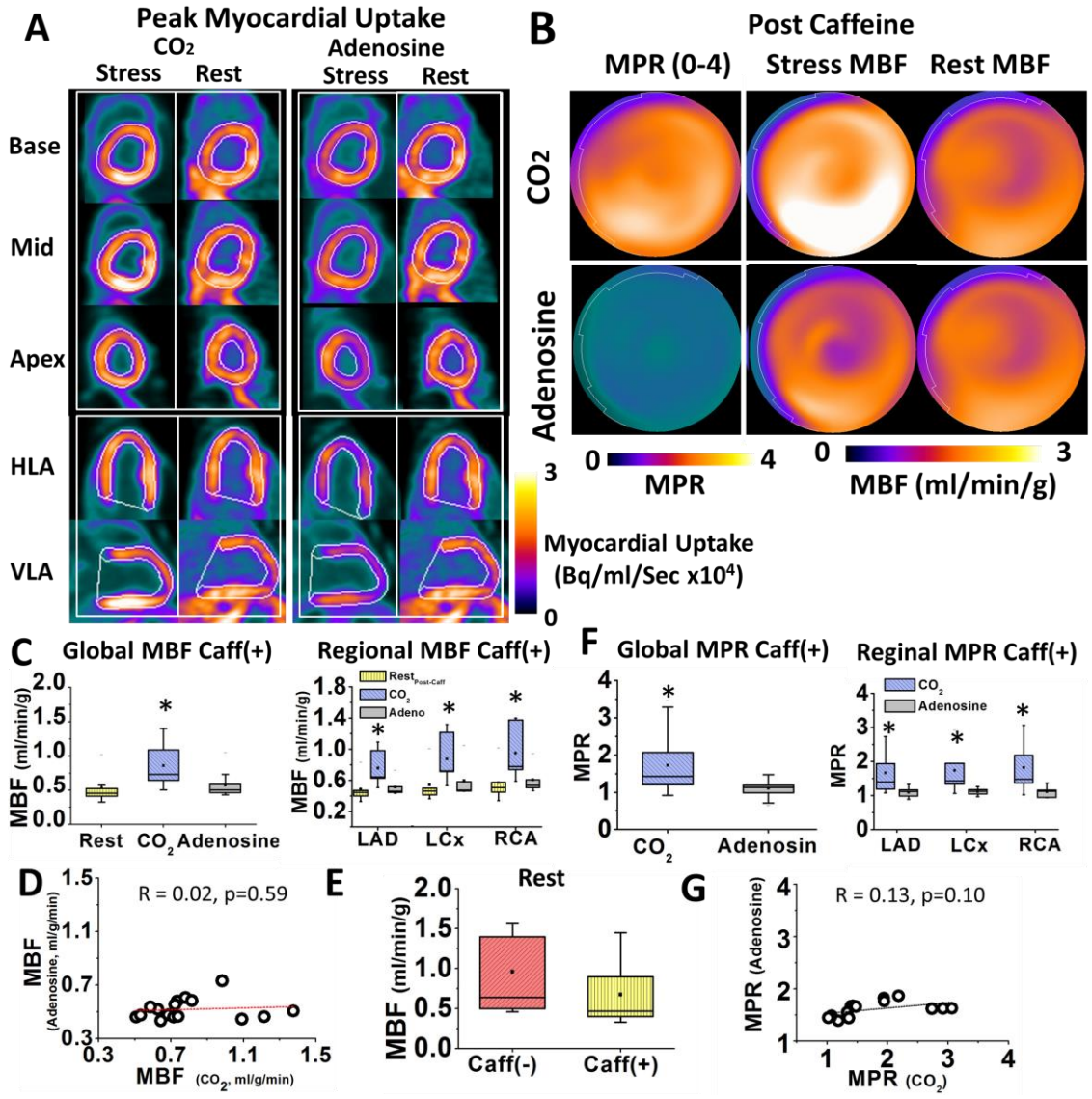

Figure 5.6 Global and Regional Myocardial Blood Flow Response to Hypercapnia and Adenosine Following Caffeine Treatment. Panel A shows representative short- (Base, Mid, Apex) and long-axis (HLA, VLA) PET images acquired during peak myocardial uptake of 13N-ammonia under hypercapnia of PaCO2 ~ 60 mmHg (CO2), standard clinical dose of adenosine (Adenosine) and at baseline conditions with PaCO2 ~ 35 mmHg (Rest) following caffeine treatment. These visual results show that the increase in myocardial uptake of radiotracer relative to rest to occur only under hypercapnia; but not under adenosine. For the case in panel A, rest and stress MBF (under hypercapnia and adenosine) and corresponding MPR are shown as polar maps in panel B. Panel C shows the global and regional mean

*MBF at rest and under hypercapnia and adenosine following caffeine infusion (Caff+). Significant global and regional myocardial hyperemia is observed under hypercapnia; however, the MBF response under adenosine was not different from rest. Panel D shows the results from linear regression analysis between regional MBF under adenosine and hypercapnia; no significant correlation between adenosine and hypercapnia was seen (R=0.02, p=0.59). Panel E shows the MBF at rest before (Caff(-)) and after (Caff(+)) caffeine treatment. Panels E and F show similar analyses of MPR under hypercapnia and adenosine. Both global and regional MPR were significantly higher with hypercapnia than with adenosine. Weak and non-significant correlation was observed between respective regional responses to hypercapnia and adenosine. * denotes p<0.05.*

Mean global MBF at rest (post caffeine) and under adenosine were not different (p=1.00) and were significantly lower than hypercapnia (p<0.05, for both). Mean regional MBF were not different between rest and adenosine (p>0.8, for all territories) but significantly higher with hypercapnia across all territories (all p<0.05). Regional MBF were not different among territories at the different conditions (rest, hypercapnia or adenosine); p>0.1, for all. Refer to Fig. 5.6C. Under caffeine, there was no correlation between MBF under adenosine and hypercapnia (R = 0.02, p=0.59; Fig. 5.6D). There was a trend towards higher resting MBF prior to caffeine treatment but was not statistically significant (p=0.09; Fig. 5.6E). However, the resting MBF normalized by rate-pressure-product were significantly higher prior to caffeine ($1.5x10^{-5}$ (pre-treatment) vs $1.0x10^{-5}$ (post-treatment), p=0.03). These observations are consistent with reports in humans (152) and are likely related to the influence of caffeine on calcium cycling at rest, which is known to promote vascular smooth muscle contraction (159,160).

Under caffeine, the global MPR under adenosine was lower than under hypercapnia (p<0.05). Regional MPR values across the different coronary territories were significantly lower than 2 (p<0.05) with adenosine but were not significantly different from 2.0 with hypercapnia (p=0.17).

Refer to Fig. 5.6F. Regional MPR regressed against adenosine and hypercapnia showed a weak and non-significant correlation (R=0.13, p=0.10). Refer to Fig. 5.6G.

This study showed that under caffeine, hypercapnia increased MBF, albeit by a lower amount than in the absence of it, compared to the complete abolishment of hyperemic response to adenosine. The findings here suggest that the mechanistic underpinnings constituting hyperemic response to hypercapnia and adenosine are not identical.

5.1.10 DISSCUSSION

Measures of blood flow within the myocardium and its modulations in response to various vasoactive stimuli can provide important insights into the health of the heart. Functional status of the myocardium and its ability to rapidly respond with increased MBF to meet oxygen demand is routinely assessed in the clinical environment using artificially elevated levels of adenosine. To date, a number of endogenous vasodilators have been identified and studied with respect to their effect on the myocardium (42). However, the effect of arterial CO_2 on MBF has been unclear. Even though the arterial tension of CO_2 is known to be a fundamental regulator of many physiological processes, its direct influence on MBF has not been well characterized, especially in relation to adenosine. Previous investigations have not been able to rigorously isolate the effects of $PaCO_2$ on MBF primarily because it has not been possible to independently and rapidly control $PaCO_2$. This limitation, coupled with limited access to noninvasive quantification of MBF changes with PET under different levels of $PaCO_2$, has made it difficult to determine whether hypercapnia can be a potent coronary vasodilator to the same extent as adenosine on the heart.

We used precise, independent and rapid control of $PaCO_2$, ^{13}N-ammonia PET, a validated image analysis approach and a clinically relevant animal model to rigorously study whether a physiologically viable hypercapnic stimulus is a potent mediator of MBF. We found that when the $PETCO_2$ is altered from rest (~35 mmHg) to ~ 60 mmHg under isoxic conditions, MBF increases to levels observed with the clinical dose of adenosine. Specifically, these changes in MBF and MPR were both globally and regionally not different from those observed with adenosine in the absence and presence of coronary stenosis. Pre-treatment with caffeine abolished myocardial hyperemia to adenosine, as expected, but not to hypercapnia.

5.1.10.1 Translational Importance of Arterial CO_2 Tension as a Potent Modulator of MBF

Given our findings that MBF is strongly influenced by hypercapnia, both scientific and clinical studies that evaluate MBF or whose outcomes are influenced by MBF need to consider the effect of $PaCO_2$ on their results. Specifically, ongoing studies aimed at therapeutic regeneration of the myocardium and interventional strategies that aim to mechanically regulate MBF may need to evaluate whether hypercapnia influences outcome. Similarly, the effect of $PaCO_2$ on MBF, especially in patients with ischemic heart disease, during intraoperative procedures (e.g., laparoscopic / abdominal robotic surgeries where $PaCO_2$ can be in excess of 70 mmHg) (161), post-operative recovery (when $PaCO_2$ can be in excess of 50 mmHg), or "permissive hypercapnia" in intensive care units (when the $PaCO_2$ is between 90-130 mmHg) (156) need to be reconsidered. Specifically, in patients with critical coronary stenosis that encounter significant hypercapnia, it appears that hypercapnia could trigger severe myocardial ischemia due to coronary steal (*20*), which could be hazardous.

Canines have been the preclinical model of choice in the literature for examining the MBF response to various pharmacological agents (42) that are now routinely used as part of cardiac stress testing, including dipyridamole , adenosine and regadenoson (162). Hence our finding of marked increase in MBF under isoxic hypercapnia has significant translational value especially within the framework of cardiac stress testing. Currently, over 10 million cardiac stress tests are performed in the US per year (125). Since many patients cannot tolerate exercise stress tests, more than half of all stress tests employ intravenously administered pharmacological stress agents, despite their well-known limitations (125). Since elevated levels of $PaCO_2$ can introduce myocardial hyperemia to the same extent as adenosine, it has the potential to be an alternative to these pharmacological agents. A desirable feature of hypercapnia-based vasodilation compared to pharmacological stress agents is that the effects $PaCO_2$ could be rapidly reversed within 2-3 breaths with prospective gas control methods as used in the study (143). In comparison, the effects of pharmacological agents are only reversed with metabolic breakdown of the administered agent or following rapid delivery of antidote, such as aminophylline (125). On the other hand, hypercapnia can induce respiratory acidosis. However, the duration (~ 4-6 mins) and extent of hypercapnia ($\Delta PaCO_2$ ~ 25 mmHg) and the associated drop in pH (~0.1) that is expected in the context of cardiac stress testing has been shown to be safe in humans (163) (164). Although, the safety and tolerance of physiologically meaningful levels of hypercapnic stimulus in patients suspected of having heart disease remains to be systematically investigated, the presence of coronary artery disease is not known to affect the tolerability to hypercapnic increases above 25 mmHg (165) (156) .

Moreover, our findings of differential MBF response to hypercapnia and adenosine following caffeine treatment suggest that the mechanism of action mediating myocardial hyperemia by

these stimuli are at least partly different. Our findings that $PaCO_2$ and adenosine appear to contribute to coronary vasodilation via different mechanisms suggests that it may be possible to synergistically combine increases in $PaCO_2$ and a reduced dose of adenosine with an aim of reducing both of their side effects. The rationale would be that both compounds act as direct coronary artery dilators and in addition, the hypercapnia increases the sympathetic drive, counteracting the hypotensive side effects of adenosine, and compensates for A_{2A} receptor blockade by caffeine.

As noted earlier, a large number of studies have investigated the effects of $PaCO_2$ on MBF. However, the reported sensitivity to invoke myocardial hyperemia, especially within the physiologically tolerable range of $PaCO_2$, from these studies has not indicated that $PaCO_2$ is a potent coronary vasodilator. Among the studies that showed a positive MBF response to hypercapnia, Eberlin and colleagues (134) using closed-chest canines showed that when $PaCO_2$ was altered from 45 mmHg to 82 mmHg, the mean increase in MBF was 2.8% /mmHg increase in $PaCO_2$. Using ^{133}Xe clearance Ledingham et al (135) showed that in response to a change in $PaCO_2$ from 40 mmHg to 100 mmHg, MBF mean increase was 0.50% /mmHg increase in $PaCO_2$ in closed-chest canines. Using ^{131}I aminopyrin, Scheuer et al. (136) showed that when $PaCO_2$ was increased from 38 to 91 mmHg, along with large bicarbonate infusion, the mean increase in MBF was 3.4% /mmHg increase in $PaCO_2$ in canines. In comparison, our closed-chest canine studies using ^{13}N-ammonia PET, showed that when $PaCO_2$ is changed from 35 mmHg to 60 mmHg, the increase in MBF was 5.6% / mmHg increase in $PaCO_2$ – nearly a two-fold increase in sensitivity to hypercapnia than the highest reported sensitivity values in the literature. This observation may be explained on the basis of significant differences between our studies and those of others. Previous studies were relatively slow to establish, maintain and/or

modulate steady-state levels of hypercapnia before making the MBF measurements (typically tens of minutes). These time-consuming manipulations may have contributed to the reduced MBF response to hypercapnia as it has been shown that the onset and extent of MBF response to hypercapnia is fast and degrades with exposure time (135). In comparison, we established the target $PaCO_2$ within a few seconds (2-3 breaths), initiating the MBF measurements within 1-2 minutes and terminating the exposure to hypercapnia within 5-6 minutes. Next, most of the previous studies did not tightly control $PaCO_2$ or PaO_2. This is particularly important for the studies that were performed under hyperoxia, since hyperoxia is known to cause coronary vasoconstriction, which can counteract the vasodilatory response from hypercapnia (42) . In this study we maintained isoxia and independently altered $PaCO_2$ with a precision of 1 mmHg. Moreover, our measurements, particularly those in intact animals, were made in the most noninvasive manner possible using state-of-the-art PET imaging and image processing approaches. These results remain to be extended into humans.

A limitation of this study is that we used the 17-segment model of the AHA to define the perfusion territories, despite its inaccuracies in humans (166) and unintended use for canines. While it is known that the coronary anatomy between canines and humans are different, the overall mapping of the coronary arteries to perfusion territories is similar to humans but not strictly the same (167). In particular, canines are typically left dominant while humans are mostly right dominant (although ~ 20% are left dominant as well) (168). This could contribute to an overestimation of MBF and MPR in the LAD region in the presence of LAD stenosis. Notwithstanding this, we observed a significant MBF difference between the assigned LAD and other supply territories in *Group Stenosis*. Further, the MBF and MPR assigned to individual coronary territories in the absence of coronary stenosis may by slightly different from reality.

However, since there was no statistical difference between the regional territories in *Groups Intact and Caffeine*, the AHA segmentation appears to be a useful model to assign MBF values.

We conclude that the arterial blood CO_2 tension is an independent variable of MBF, which when increased by 25 mmHg can induce MBF to the same level as clinical dose of adenosine. Our studies also suggest that prospectively targeted arterial CO_2 has the capacity to evolve as a potent vasodilator for clinical cardiac stress testing and that all research studies or clinical conditions which require control of MBF could benefit from regulating CO_2 tension of the arterial blood.

5.2 Assessment of Myocardial Reactivity to Targeted Hypercapnia with Free-breathing T_2-prepared Cardiac Blood-Oxygen-Level-Dependent MR

5.2.1 INTRODUCTION

Cardiac stress testing is the standard of care for diagnosing ischemic heart disease (2). It is performed in nearly 10 million patients each year in the US alone. It is conventionally initiated with exercise to induce hyperemia and coupled with imaging to identify stress-induced failure to increase perfusion, or frank hypo-perfusion in myocardial territories. The approximately 50% of patients who find it difficult to perform sufficient exercise for an adequate test are administered coronary vasodilators such as adenosine, which carries a rare but serious risk of heart attack and death (169). A limitation of this approach is that all drugs have complex pharmacology and pharmacokinetics making it difficult to achieve a consistent blood level across patients; there is a large individual variation in response--even to a given blood level.

It has been suggested that increases in the arterial partial pressure of CO_2 ($PaCO_2$), termed hypercapnia, long known as a vasodilator of cerebral vessels (170), may increase coronary blood flow in similar measure (42,135,140,171). Hypercapnia as a myocardial vasodilator has some theoretical advantages over pharmacologic agents. It is a natural intrinsic molecule and can be administered non-invasively through the respiratory system. For the target application of cardiac stress testing it would only need to be applied for one or two minutes, with its effect terminating in seconds. An increase of 10 mmHg, from resting values (about 40 mmHg) is well tolerated in a population similar to that requiring cardiac stress testing (172). It has a favorable safety profile with sustained levels over 3-times resting with no adverse effect on organ function (156). The main technical drawback of the use of hypercapnia has been that precise targeting, modulation, and monitoring of $PaCO_2$, particularly in spontaneously breathing humans.

Recent advances in computerized control of gas delivery (144,173) have enabled the precise and independent control of end-tidal partial pressures of CO_2 ($PETCO_2$) and O_2 ($PETO_2$). Importantly, the $PETCO_2$ attained with one of these methods, prospective end-tidal targeting, is equal to $PaCO_2$ (144) —the independent variable with respect to vasoreactivity (143). A second advance exploited for this study is the refinement of non-invasive MRI-based approach for examining cardiac perfusion (31,68,76). Myocardial Blood-Oxygen-Level-Dependent (BOLD) MRI (174,175) is a noninvasive (radiation- and contrast-agent-free), high-resolution, imaging method that could provide details of myocardial blood flow based on the changes in oxidative state of hemoglobin (176) reflecting the balance between myocardial oxygen demand and supply.

The first hypothesis of this study was that an increase in $PaCO_2$ of up to 10 mmHg in healthy humans would result in changes in myocardial blood flow of the same order of magnitude as

adenosine. To address this hypothesis we compared the effects of hypercapnia on myocardial blood flow in healthy volunteers to published values with adenosine. The second hypothesis of this study was that hypercapnia would result in coronary vasodilation and increase in myocardial blood flow to the same order of magnitude as adenosine, and would generate similar myocardial perfusion patterns on myocardial BOLD MRI in intact dogs and those with LAD stenosis. In addressing both hypotheses, we used myocardial BOLD MRI as a surrogate measure of myocardial blood flow. Hence the purpose of this study was to examine whether controlled and tolerable levels of hypercapnia may be an alterative to adenosine, a routinely used coronary vasodilator, in healthy human subjects and animals.

5.2.2 METHODS

5.2.2.1 Human Studies

Healthy human volunteers (n=18, 9 female, age = 30±5 years, range = 21 – 40 years) were recruited in accordance with the protocol that was reviewed and approved by the Institutional Review Board. Every participant was competent and provided written informed consent and had no history of CAD, lung disease, abnormal cardiac rhythm and rate, kidney/liver disease, and were not contraindicated for cardiac MR exams (completed a detailed cardiac MRI questionnaire). Volunteers were required to be non-smokers, to fast for 12 hours and refrain from intake of caffeine or performance of vigorous exercise prior to the study.

Control of end-tidal gases

Prospective targeting of $P_{ET}CO_2$ and $P_{ET}O_2$ were implemented by an algorithm-driven computerized gas blender administering gases to a sequential gas delivery breathing circuit

(RespirAct™, Thornhill Research Inc., Toronto, Canada). The principle of control of $PETCO_2$ by prospective gas targeting depends on the control of alveolar ventilation ($\dot{V}A$) in the relationship $P_{ET}CO_2 = \dot{V}CO_2 / \dot{V}A$ where $\dot{V}CO_2$ is the measured CO_2 production. Part of the exhaled gas is retained by the breathing circuit in a reservoir. The breathing circuit receives a controlled rate of gas flow. The patient breathes this flow and makes up the balance of breathing with rebreathed gas. As the exhaled gas has already equilibrated with the pulmonary capillary blood, it does not contribute to gas exchange, leaving the gas from the gas blender as the only source of alveolar gas exchange. In other words, the gas blender flow is equal to the $\dot{V}A$ and can therefore be used according to the above equation to target $PETCO_2$ independently of ventilation. As any CO_2 in the inhaled gas can be considered an equivalent reduction in $\dot{V}A$, a combination of gas flow and inspired PCO_2 can generate any $\dot{V}A$, independently of ventilation. Similar considerations are invoked for the control of $P_{ET}O_2$. The underlying rationale for the method and its practical implementation are discussed in greater detail elsewhere (145).

Prior to entering the scanner, the volunteers underwent a trial of an abbreviated targeted breathing sequence consisting of one minute each of $PETCO_2$ targeted at 5 and 10 mmHg, above resting values (Plus 5 and Plus 10 respectively) to evaluate their tolerance to elevated levels of CO_2 and to familiarize them to the variations in CO_2 levels. In the scanner, subjects' $PETCO_2$ was increased to Plus 5 and Plus 10 consecutively, each for 4 min. All subjects tolerated the testing sequences and during MRI.

Cardiac MR and CO_2 Manipulation Protocols

All imaging studies were performed on a 3.0 T clinical MRI system (Siemens MAGNETOM Verio®, Erlangen, Germany). Subjects were placed on the scanner table and continuous monitoring of ECG, pulse oximetry and non-invasive blood pressure readings were established. A posterior spine array coil and a flexible phased-array coil (placed on the chest) were used for signal reception. Following whole-heart shimming and localization of true axes of the heart, ECG-triggered, motion-corrected, free-breathing T_2-prepared SSFP acquisitions (as described previously by Kellman et al (77)) were prescribed over a mid-ventricular slice along the short-axis at each targeted $PaCO_2$ level (as described above). Images were acquired with following parameters: single-shot acquisitions with GRAPPA (rate 2) and 4 signal averages; T_2-preparation time = 40 ms; TR/TE = 2.9/1.5 ms; flip angle = 45^o; slice thickness = 6 mm; in-plane resolution = 1.7 x 1.7 mm^2; trigger pulse of 2; and readout bandwidth (BW) = 1371 Hz/pixel. Myocardial BOLD MR acquisitions were triggered at each $PETCO_2$ level (baseline, Plus 5, and Plus 10) one minute following the stabilization of $PETCO_2$ values. $PETO_2$ was maintained at resting values (i.e., while breathing room air).

5.2.2.2 Canines Studies

Canine Preparation

Mongrel dogs (n=14, 20-25 kg) were studied according to the protocols approved by the Institutional Animal Care and Use Committee of Cedars-Sinai Medical Center. Each dog was sedated with acepromazine (0.5-1·0mg/kg SQ), induced with propofol (2.0-5.0 mg/kg IV), endotracheally intubated, and maintained on inhalational gas anesthesia (2·0-2·5% isoflurane, 1-2 L/min of 100% oxygen). A left lateral thoracotomy was performed at the fifth intercostal space

to expose the heart. Catheters were implanted into the descending aorta (for invasive pressure measurement) and left atrium (for blood sampling). A 20 MHz Doppler probe was affixed on the outer surface of vessel immediately distal to the first branch of the left anterior descending coronary artery (LAD) to enable measurement of left anterior descending coronary artery artery flow velocity. In half of the dogs (n=7), an externally actuated hydraulic occluder was affixed proximal to the Doppler flow probe to allow the induction of LAD stenosis. Subsequently, the chests were closed and the dogs were allowed to recover for at least 7 days prior to imaging studies.

Prior to imaging, dogs were fasted for 18 hours, sedated using acepromazine (0.5-1.0mg/kg SQ) or midazolam (0.4mg/kg IM), anesthetized with propofol (2.0-5.0 mg/kg, IV) and intubated. During the imaging studies, anesthesia was maintained with a continuous infusion of propofol (0.03-0.1 mg/kg/min, IV). Dogs were transferred to the MR scanner table and were initially mechanically ventilated (Model 2002 Halowell EMC, MA, USA) with tidal volume 7-10 ml/kg, frequency 12-15/min, and inspiration to expiration ratio 1:2. A secondary sequential gas delivery circuit, functionally similar to that used for spontaneous ventilation (143,145), was interposed between the dog and the ventilator to enable end-tidal gas control by the RespirAct™ (Figure 5.7). During end-tidal gas control tidal volume was increased to 10-15 ml/kg and frequency to 15-20 /min to assure end-tidal rebreathing. ECG, SPO_2, heart rate, invasive blood pressure (systolic, diastolic, and mean arterial), and temperature (Expression, Invivo, FL, USA) were monitored.

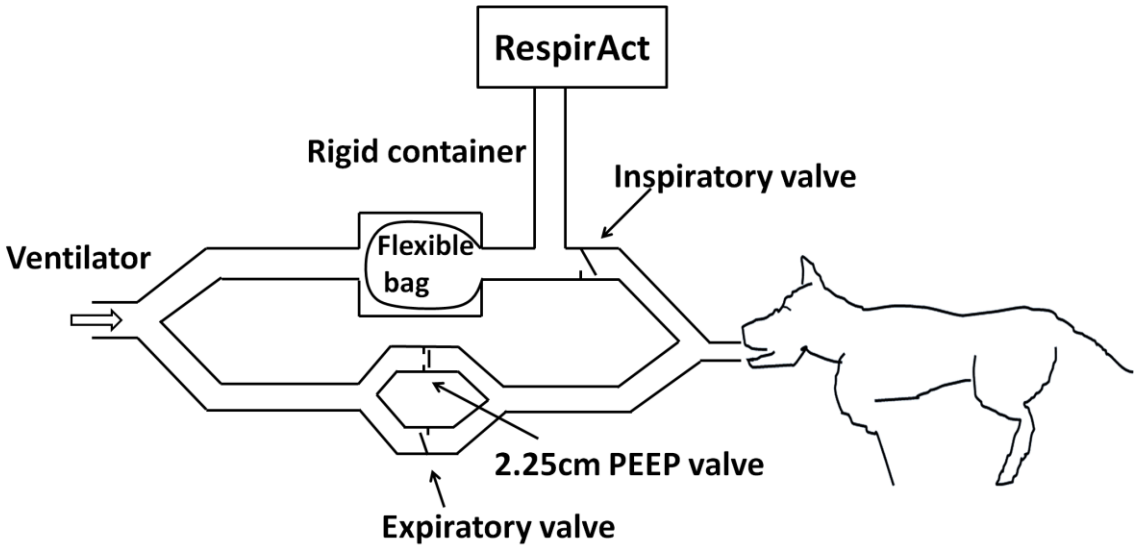

Fig. 5.7: A schematic diagram of the breathing circuit used to ventilate and control the end-tidal gas concentrations in ventilated canines. The gas control system (RespirAct; Thornhill Research) flows a gas mix of carbon dioxide, oxygen, and nitrogen into the circuit. During exhalation, the exhaled gas enters the expiratory limb of the circuit (lower limb in diagram). The expiratory valve opens passively, which allows gas to vent into the ventilatory circuit and then to atmosphere. Also during exhalation, the gas from the gas control system collects in the flexible bag. On the inspiratory cycle of the ventilator, the PEEP valve on the expiratory limb of the circuit directs the ventilator flow down the path of lesser resistance into the rigid container displacing gas from the flexible bag into the canine. When the bag is collapsed, the pressure in the circuit increases until the PEEP valve is overcome and the ventilator gas is directed down the expiratory limb, which results in rebreathing of previously exhaled gas. This results in the sequential delivery of the source gas (ie, fresh gas) followed by the previously exhaled gas. Changes in alveolar ventilation are affected by controlling the concentrations of carbon dioxide, oxygen, and nitrogen in a constant flow of inspired gas by the gas control system according to algorithms described by Slessarev et al (1).

Cardiac MR and Coronary Artery Blood Flow Velocity Measurement Protocol

As the relationship between $PaCO_2$ and changes in coronary flow are unknown, we studied the flow response to a graded range of $PETCO_2$ 30 mmHg, 40 mmHg, 50 mmHg, and 60 mmHg, in

7 dogs. This $PETCO_2$ range is 10 mmHg below and 10 mmHg above our test protocol of target change from 40 mmHg to 50 mmHg and would indicate the available dynamic range of coronary blood flow in response to hypercapnia (Group Ramp Figure 5.8). Coronary blood flow velocities were measured at the different $PETCO_2$. The protocol used to examine the effect of coronary stensosis on blood flow is summarized in Figure 5.8 (Group *Occluder*).

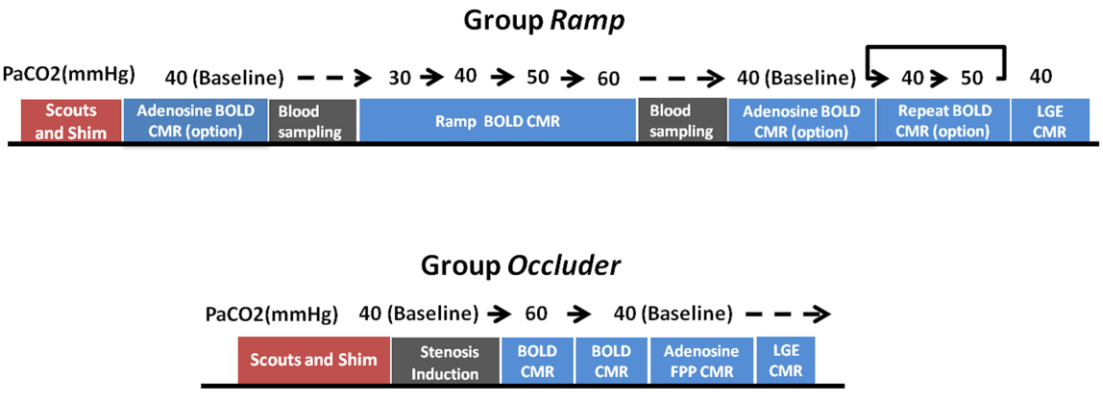

Fig. 5.8: Chronological sequence of data collection. Two groups of canines (ramp [a] and occluder [b] groups) were studied and the data collection events are shown for each group. All canines were scouted and shimmed in the MR imaging system (Scouts and Shim) and the pressure values over the event blocks (or continuation arrows) point to the corresponding Petco2 associated with the event. In ramp group, during the adenosine block, adenosine infusion is started and myocardial BOLD MR acquisitions were performed. This event was randomized so as to induce pharmacological stress either at the beginning of the study or near the end of the study. Thus, if adenosine block is performed near the beginning of the study, the terminal adenosine block is not implemented, and vice versa Stenosis Induction refers to the inflation of the hydraulic occluder to induce LAD stenosis. Stenosis Removal + Recovery refers to deflation of the hydraulic occluder to remove the LAD stenosis.

All imaging studies were performed on a 3.0 T clinical MRI system (Siemens MAGNETOM Verio®, Erlangen, Germany). Dogs, prepared in the manner described above, were placed on the scanner table in the feet-first right-lateral position. The imaging protocol (localizations, cardiac

shimming, and BOLD MR) and the scan parameters were the same as that used for the human studies (listed above), except the in-plane resolution was 1.7 x 1.7 mm^2.

Adenosine and CO_2 protocol order was randomized; BOLD MR was prescribed over identical imaging slices. In two dogs from Group *Ramp*, BOLD MR acquisitions were also performed in the long axis views (LVOT) for visualization purposes (not included in quantitative analysis), at baseline ($PETCO_2$ ~ 40 mmHg) and at peak hypercapnia ($PETCO_2$ ~ 60 mmHg). In both cases, the dogs were allowed to recover to baseline conditions between the protocols (verified by attaining $PETCO_2$ ~ 40 mmHg and restoration of resting Doppler coronary blood flow velocity). Specifically, BOLD MR acquisitions were prescribed following 2 minutes of adenosine infusion (140 □g/kg/min, IV) and approximately 1 minute after the desired $PETCO_2$ values were reached. Prior to, or right after, the baseline ($PETCO_2$ ~ 40 mmHg) and peak hypercapnia ($PETCO_2$ ~ 60 mmHg) BOLD acquisitions, the Doppler transducer (Triton Technology Inc, CA, USA) was connected to the wires originating from the surgically implanted Doppler probe and root-mean-square Doppler flow velocity values were recorded. In dogs where LAD stenosis was to be induced, peak hyperemic coronary blood flow velocity measured at PETCO2 ~ 60 mmHg was reduced to coronary blood flow velocity measured under PETCO2 ~ 40; and (c) after 3 minutes of adenosine infusion. Once the imaging studies were completed, dogs were euthanized.

5.2.2.3 Image Analysis

Two expert reviewers (H.Y, R.D.) evaluated the images in consensus, each with more than 4 years of experience evaluating cardiac MR images. Reviewers were blinded to any other patient or canine data.

Myocardial BOLD MR images, obtained from humans and canines, were analyzed using ImageJ, (version 1.46, National Institutes of Health, MA, USA). Contours were traced to segment the myocardium (excluding the papillary muscles) and mean signal intensity of the myocardium was measured for each experimental condition. At each condition, *% Hyperemic BOLD Response*, and % coronary blood flow velocity were computed, relative to baseline and mean *% Hyperemic BOLD Response* was computed for each study group. For Group *Occluder*, the myocardium into AHA 6 segments and the *% Hyperemic BOLD Response* was computed for each segment at different experimental conditions ($PETCO_2$ ~ 60 mmHg; and adenosine) by normalizing the BOLD intensity at hypercapnia and adenosine by BOLD intensities obtained under $PETCO_2$ ~ 40 mmHg. First-pass perfusion images (acquired with adenosine under LAD stenosis) were also segmented in the same fashion. The segments identified to have perfusion defects on the first-pass perfusion images were labeled as Affected and matched to the segments on myocardial BOLD MR images acquired under hypercapnia and adenosine; all others were labeled Remote.

5.2.2.4 Statistical Analysis

In humans, multiple, repeated measurements ANOVA were performed to test whether the rate-pressure product, and blood pressure (systolic, diastolic, and mean arterial) were different from baseline at the two different hypercapnic states. Repeated measurements ANOVA was performed on the mean *% Hyperemic BOLD Response* measured to determine whether the responses observed at Plus 5 and Plus 10 were different from the values reported by Arnold *et al* (175) for adenosine. All values are reported as mean ± SD and statistical significance was established for $p<0.05$. Statistical analysis was performed in IBM SPSS (V21.0, NY, USA).

In dogs, repeated measurements ANOVA tests were performed to examine whether the rate-pressure product, heart rate, and blood pressure (systolic, diastolic, and mean arterial) were different between baseline, hypercapnia, and adenosine. Post-hoc comparison with Bonferroni correction was used if the null hypothesis was rejected. Correlation analysis was performed between measured values of $PaCO_2$ and $PETCO_2$ at different physiological states for dogs from Group *Ramp*. *%Hyperemic BOLD Response* from Group *Ramp* was fitted to $PETCO_2$ using a sigmoidal model (170). The reproducibility of *%Hyperemic BOLD Response*, for a given $PETCO_2$ was evaluated from repeat measurements obtained in dogs from repeat myocardial BOLD measurements in Group Ramp, was examined with a paired t-test. A paired t-test was also performed to evaluate whether *%Hyperemic BOLD Response* and *% Hyperemic Coronary Blood Flow Velocity Response* obtained at the highest $PETCO_2$ from Group *Ramp* were different from *% Hyperemic Responses* obtained with adenosine. A two-way repeated measurement ANOVA was used to test the effects of region (two categories: remote and affected) and type of vasodilator (two categories: hypercapnia and adenosine) and their interaction on *% Hyperemic BOLD Response*. Kappa (Cohen's) statistic was used to determine the level of concordance between the perfusion defects observed with hypercapnia and adenosine. For this purpose, the segments positive for perfusion defect were identified as those conforming to mean segmental intensities that are at least one SD below the mean intensity of the myocardium; all others were considered to be normal (no perfusion defect).

5.2.3 RESULTS

5.2.3.1 Human Volunteer Studies

Physiological parameters recorded from the volunteers at baseline and the two elevated $PETCO_2$ (Plus 5 and Plus 10) are summarized in Table 1. Systolic, diastolic and mean arterial blood pressure and rate-pressure product did not differ between conditions (baseline, Plus 5, and Plus 10). Myocardial BOLD MR images of a healthy human volunteer at baseline and hypercapnia (Plus 10) showed a marked increase in BOLD signal intensity in response to hypercapnia (Figure 5.9A). The response at Plus 5 was not greater than that at baseline (102±3% (Plus 5) vs. 100% (baseline), p=0.64); the response at Plus 10 was greater than the one at baseline (111±10% (Plus 10) vs. 100% (baseline), p<0.01) and Plus 5 (111±10% (Plus 10) vs. 102±3% (Plus 5), p < 0.01) (Figure 5.9B). The mean response at Plus 10 in our volunteers was not different (111±10% (Plus 10) vs. 112±11% (adenosine), p=0.75) from adenosine (175).

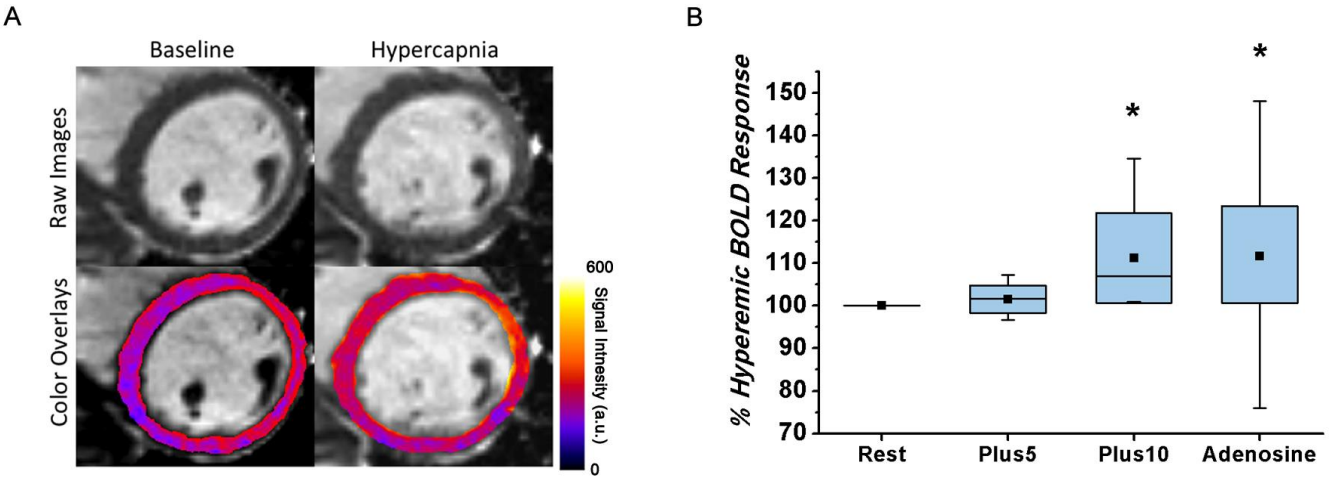

*Fig 5.9 Effect of changing arterial CO2 on Myocardial BOLD MR signal intensities in healthy humans. Representative short-axis Myocardial BOLD MR images collected from a human volunteer at baseline (PETCO2= 37 mmHg) and hypercapnia (PETCO2 = 47 mmHg) are shown in panel A. BOLD signal intensity increased during hypercapnia. For ease of visualization, color overlays of the left ventricle (with color bar showing BOLD signal intensity in arbitrary units (a.u.)) corresponding to the gray scale images are shown directly below. Box plot showing the dependence of % Hyperemic BOLD Response on PETCO2 and standard dose of adenosine is shown in panel B. % Hyperemic Response increased at higher PETCO2 values; response at Plus 10 did not differ from that due to standard adenosine infusion. %Hyperemic BOLD Response for adenosine is from reported values in the literature (175). *denotes statistically significant difference relative to Rest ($p < 0.05$). Top and bottom of boxes indicate (upper limit +1 SD and lower limit -1 SD, respectively; error bars (whiskers) are maximum and minimum of data. The mean and median are represented as a point and a band within the box, respectively. For adenosine, the whiskers represent the boundaries of 1st and 99th percentile of the data.*

5.2.3.2 Canine Studies

Figure 5.10 shows examples of raw data for $PETCO_2$ for Group Ramp (Figure 10C) and Repeat Measurement (Figure 5.10D) and their respective ensemble flow responses (Figure 5.10A and 5.10B, respectively). Figure 5.10A shows the flattening out of the slope of BOLD response to changes in $PETCO_2$ above and below the range 40-50 mmHg. Figure 5.10B shows a more than 6% change in BOLD signal in response to hypercapnia. Mean *% Hyperemic BOLD Responses* between the two hyperemic and baseline states did not differ (7±3% (first cycle) vs. 10±4% (second cycle), p=0.74).

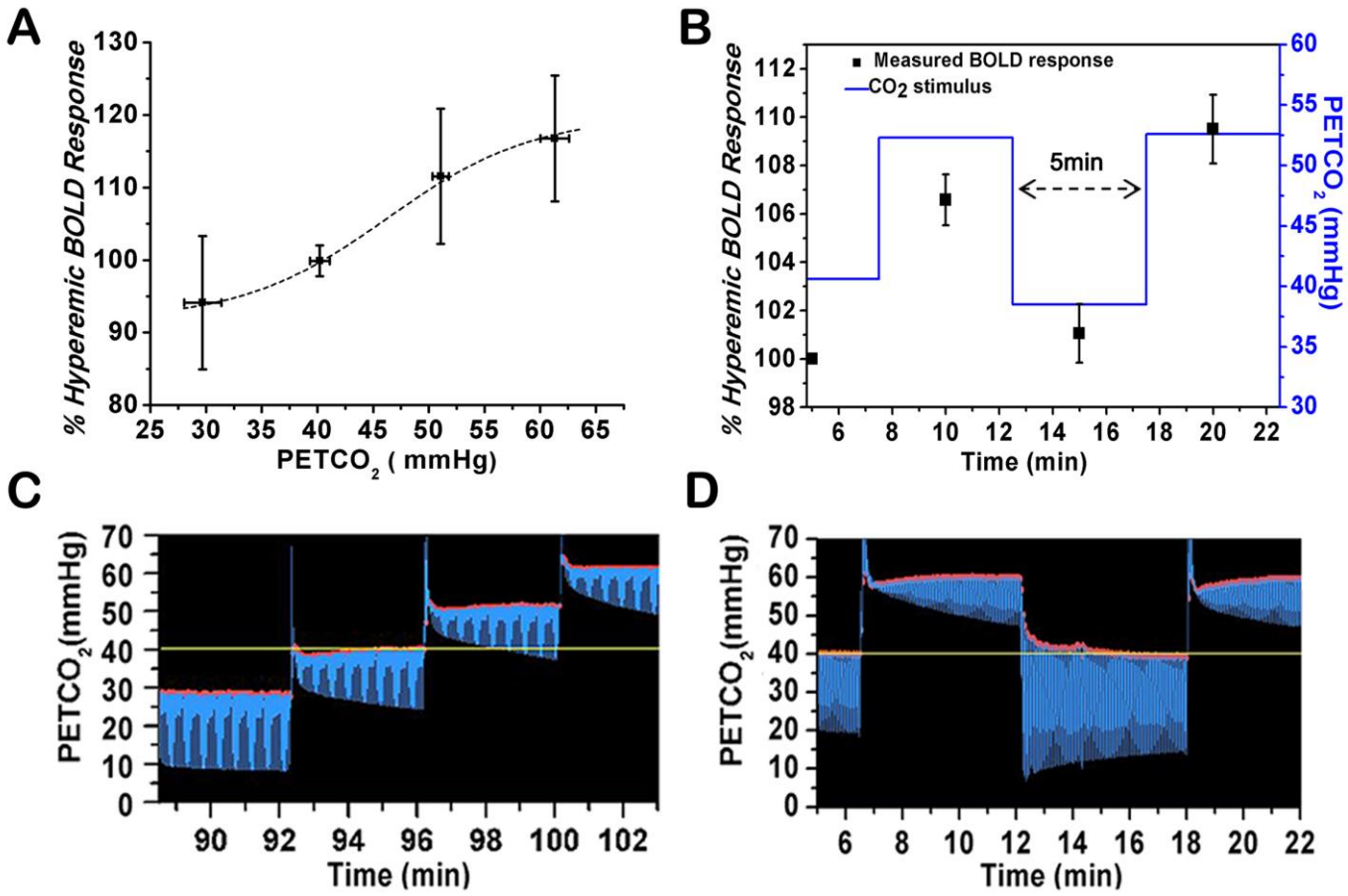

Figure 5.10 Relation between % Hyperemic BOLD Response and PETCO2 in canines. % Hyperemic BOLD Response (defined in text) is directly related to PaCO2 (30 to 60 mmHg) and shows a sigmoidal relation (data fitted to individual measurements) over the range of PETCO2 values studied (A). When the PETCO2 was modulated between 40 and 50 mmHg, % Hyperemic BOLD Response also showed equivalent changes, (B). For reference, average % Hyperemic BOLD Response at the different PETCO2 levels is shown. Panels C and D show the dynamic and precisely targeted changes in PETCO2 administered to the animals.

Mean *% Hyperemic BOLD Responses* and *% Hyperemic Coronary Blood Flow Velocity Response* during peak hypercapnia (mean $PETCO_2$ = 56±5 mmHg, Table 1) and adenosine infusion were not statistically different (BOLD: 117±14% (hypercapnia) vs. -114±23%(adenosine), p=0.80, coronary blood flow velocity: 120±15% (hypercapnia) vs.

126±22%(adenosine), p=1.00, Figure 5.11). Physiologic responses to changes in $PaCO_2$ are summarized in Table 2.

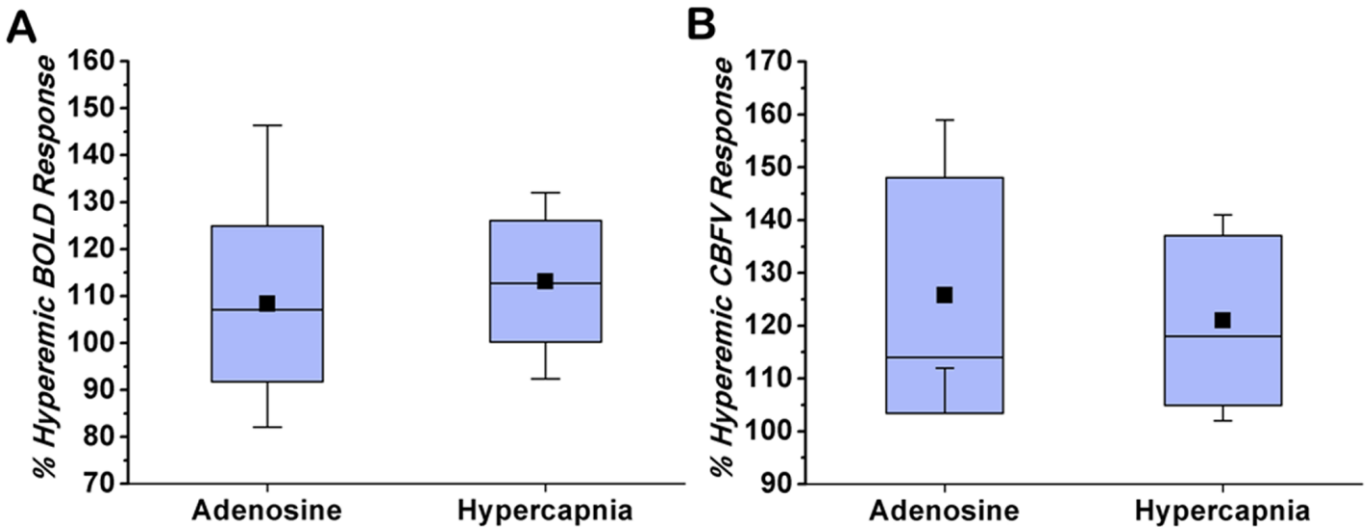

Fig 5.11 Box and whisker plot of (a) percentage of hyperemic BOLD response and (b) percentage of hyperemic coronary blood flow velocity response because of peak hypercapnia (Paco2, 56 mm Hg ±5) and adenosine infusion (clinical dose) in canines from ramp group. The mean percentage hyperemic BOLD response and percentage hyperemic coronary blood flow velocity response between the peak hypercapnic state and adenosine were not different (P = .80, P > .99, respectively).

	Baseline	Plus 5	Plus10
$PETCO_2$ (mmHg)	38 ± 3	43 ± 3* (p<0.01)	47 ± 3* (p<0.01)
$PETO_2$ (mmHg)	110 ± 6	111 ± 3 (p=1)	116 ± 4 (p=1)
Heart Rate (beats/min)	65 ± 10	69 ± 12 (p=1)	72 ± 11* (p<0.05)
Systolic blood pressure (mmHg)	109 ± 10	109 ± 8 (p=1)	111 ± 9 (p=1)
Diastolic blood pressure (mmHg)	60 ± 9	61 ± 9 (p=1)	63 ± 8 (p=1)
Mean arterial pressure	85 ± 8	85 ± 8 (p=1)	87 ± 8 (p=1)
Rate-pressure product	7000 ± 1572	7428 ± 1686 (p=1)	7675 ± 1737 (p=1)

Table 5.5: Physiological parameters measured in healthy human volunteers during cardiac MR studies

p values provided in the parenthesis are relative to baseline and (*) denotes cases where statistical significance (p< 0.05) was evident. Plus 5 and Plus denote 5 and 10 mmHg of PETCO2 above baseline.

	Baseline	Hypocapnia	Hypercapnia	Adenosine
Targeted $PaCO_2$ (mmHg)	40 ± 1	30 ± 2*(p<0.01)	56 ± 5*(p<0.01)	-
Actual $PaCO_2$ (mmHg)	43 ± 4	35 ± 5*(p<0.01)	54 ± 7* (p<0.01)	43 ± 4(p=1)
Targeted PaO_2 (mmHg)	113 ± 10	107± 12 (p=1)	111 ± 9 (p=1)	-
Actual PaO_2 (mmHg)	101 ± 14	102 ± 19 (p=1)	102 ± 16 (p=1)	101 ± 14(p=1)
Heart Rate (beats/min)	86 ± 14	80 ± 20 (p=1)	105 ± 29*(p<0.01)	119 ± 27*(p<0.01)
Systolic blood pressure (mmHg)	94 ± 9	96 ± 8 (p=1)	92 ± 7 (p=0.7)	80 ± 13*(p<0.01)
Diastolic blood pressure (mmHg)	58 ± 11	57 ± 12 (p=1)	54 ± 11(p=1)	46 ± 16 (p=0.41)
Mean arterial pressure (mmHg)	76 ± 9	77 ± 9 (p=1)	73 ± 8 (p=1)	63 ± 14 (p=0.2)
Rate-pressure product (bpm x mmHg)	8050 ± 2472	7674 ± 2011(p=1)	9567 ± 2595 (p=0.8)	9015 ± 2147(p=1)
SPO_2 (%)	95.7 ± 0.5	95.1 ± 0.4 (p=1)	94.9 ± 1.4 (p=1)	95.7 ± 0.5 (p=1)
Temperature (^oF)	99.7 ± 1.2	100 ± 1.4 (p=1)	99.8 ± 1.2 (p=1)	101 ± 1.4 (p=1)

*Table 5.6: Physiological parameters measured in Group Ramp during cardiac MR studies. p values provided in the parenthesis are relative to baseline and * denotes cases where statistical significance (p< 0.05) was evident.*

The hypercapnia-induced hyperemic response in healthy canines was visualized as an increase in BOLD signal intensity relative to baseline (Figure 5.12).

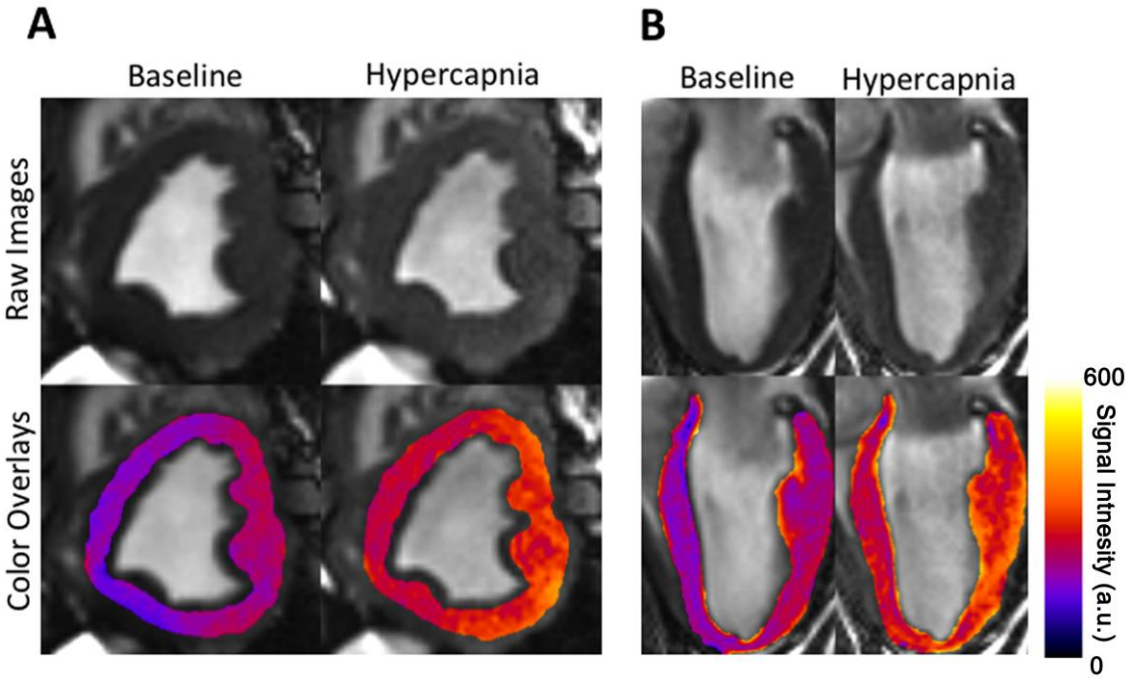

Figure 5.12: Images show effect of changing arterial carbon dioxide on myocardial BOLD MR signal intensities. Representative short (a) and long (b) axis myocardial BOLD MR images collected from a canine from ramp group under baseline (P_{ETCO_2}, 42 mm Hg) and hypercapnia (P_{ETCO_2}, 55 mm Hg) are shown. Note the increase in signal intensity in images under hypercapnia relative to baseline. For ease of visualization, color overlays of the left ventricle (with color bar showing BOLD signal intensity in arbitrary units [a.u.]) corresponding to the grayscale images are shown directly below.

Myocardial BOLD images from Group *Occluder* showed diminished BOLD responses in the Affected (LAD) territory, but increased responses in the Remote (unaffected) territory in the presence of LAD stenosis (Figure 5.13).

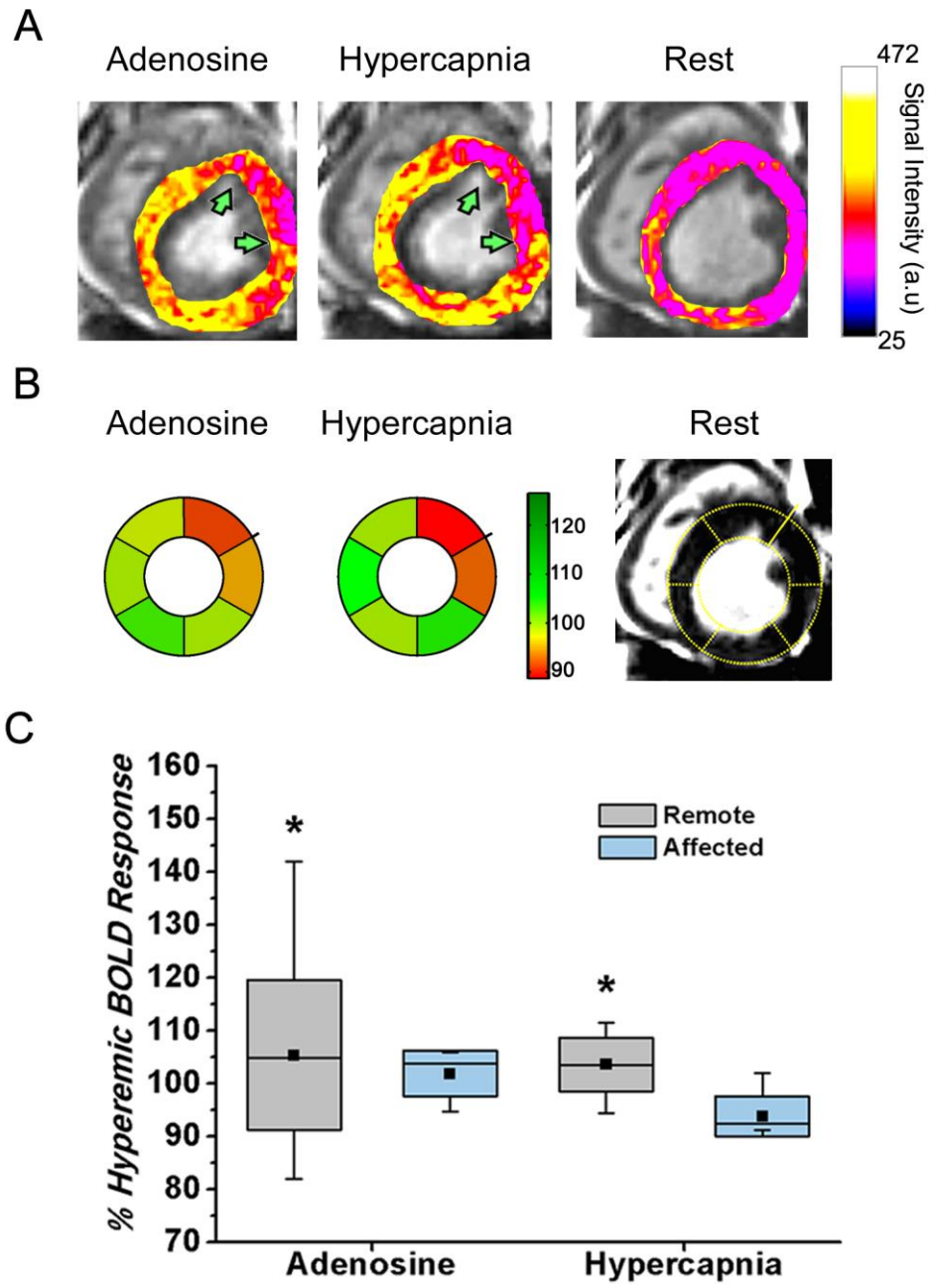

Fig 5.13 BOLD Response to adenosine versus hypercapnia in the presence of LAD stenosis in canines. (A) Representative color-overlaid BOLD MR images acquired during adenosine infusion, hypercapnia, and rest from a canine with a LAD stenosis. Color bar shows myocardial BOLD MR signal intensity. Images acquired under adenosine infusion and at rest were obtained under normocapnia. (B) Bull's eye plots constructed from images in panel A; the raw rest image with segmentation details is shown for reference. The point of radial extension on the epicardial contour of the bull's eye plots and rest BOLD MR image indicates the right-ventricular insertion point. Color base is shown to index the magnitude of

*the BOLD response between rest and stress. Note the close correspondence in hypoperfused territories between hypercapnia and adenosine (arrows, panel A) and the normalized BOLD response of myocardial segments at both hyperemic states (adenosine and hypercapnia) relative to resting state in panel B. (C) Box plot showing % Hyperemic BOLD Response from Affected and Remote (unaffected) segments in the presence of LAD stenosis in canines. Box plot presentation is the same as before. * denotes statistically significant difference relative to Affected territories (p<0.05). Actual values in panel C are: For adenosine: 1.01 ± 0.04 (stenosis segments) and 1.06± 0.04 (remote segments); and for hypercapnia: 0.94± 0.04 (stenosis segments) and 1.04± 0.04 (remote segments).*

%Hyperemic BOLD Response from animals from Group *Occluder* measured under hypercapnia (mean $PETCO_2$ = 55±3 mmHg) and adenosine from the Affected and Remote segments in the presence of LAD stenosis showed no difference in the responses to the two vasodilatory stimuli (1±4% (hypercapnia) vs. -6±4%(adenosine), p=0.12) in canines with patent coronary arteries; there was, however, a significant (105±10% (remote) vs. 97±5%(affected), p=0.01) difference in *%Hyperemic BOLD Response* between Remote and Affected segments in canines with LAD stenosis. The concordance between the segments identified as ischemic with adenosine and hypercapnic stimuli was high (=0.75, 95% CI=(0.48,1.00)), indicating that the region and extent of ischemic and non-ischemic territories identified with both forms of stimuli are not different.

5.2.4 DISCUSSION

The key finding of this study is that free-breathing T_2-prepared myocardial BOLD MR responses under hypercapnia of 10 mmHg and adenosine are not different. In particular, we found that that in humans a modest, precisely controlled, increase in baseline $PETCO_2$ of 10 mmHg was both tolerable and sufficient to elicit a measurable increase in myocardial BOLD signal intensity. In

this pilot study, the extent of increase in myocardial BOLD response was not different from that of adenosine. The controlled studies in canines with and without coronary artery stenosis yielded additional important insights. First, canine studies showed a sigmoidal relationship between $PaCO_2$ and BOLD response. This data also indicated that the mean increase in $PaCO_2$ above baseline by 11 mmHg encompassed a substantial portion of this dynamic range and resulted in an increase in myocardial blood flow similar to that elicited in response to a standard clinical dose of adenosine. Notably, the reproducible BOLD responses observed following repeat stimulation between baseline and equivalent hypercapnic states indicate that the response did not diminish or potentiate with repetition. This implies the possibility that hypercapnic stimulation is reversible and repeatable, and would therefore allow repeat testing at a single session. In addition, in canines with coronary artery stenosis, hypercapnia and adenosine resulted in similar BOLD responses. While we found the heart rate to increase during hypercapnia, we also found a concomitant decrease in blood pressure, with both contributions causing no statistical changes in the rate-pressure product, a metric that is commonly used to assess cardiac work (Tables 1 and 2). Hence within the scope of this work (i.e. in limited subjects, both animals and humans) it appears that increased heart rate associated with hypercapnia may not lead to an increase in oxygen demand. Nonetheless, additional studies are necessary to explore the mechanism of action of CO_2 mediating to coronary vasodilation and observed physiological changes, such as heart rate, in response to hypercapnia. Collectively, these findings warrant more direct investigation as to whether hypercapnia could result in data equivalent to that of pharmacologic vasodilators for cardiac stress testing.

5.2.4.1 Limitations of Previous Studies Relating $PaCO_2$ to Myocardial Blood Flow

A major limitation of previous studies has been the inadequate control of the $PaCO_2$, the actual physiologic stimulus to the coronary arteries. Tzou et al (138) found that even in the presence of mild hyperoxia (inspired O_2 concentration of 40%), increasing the $PETCO_2$ by 10 mmHg, increased the proximal LAD flow velocity by 37%. In contrast, Momen et al (139) did not detect any increase in coronary blood flow velocity in response to 5% CO_2 in oxygen. However, their inspired gas was hyperoxic possibly resulting in coronary vasoconstriction, and it is well known that a constant inspired CO_2 concentration does not have a consistent effect on the $PaCO_2$ (144,177-179); the authors did not measure $PaCO_2$ or report $PETCO_2$. Yokoyama et al (141) administered 7% CO_2 via a non-rebreathing mask, managing to increase the $PaCO_2$ from 40.2±2.4 mmHg to only 43.1±2.7 mmHg, a statistically significant increase, but a physiologically trivial one. It is not surprising that they did not find CO_2-attributable coronary vasodilation (180,181). In our study, an increase in $PETCO_2$ of 5 mmHg was also insufficient to generate a measurable change in myocardial blood flow, but differs from these studies in important ways. First, we attained significantly greater hypercapnic stimulus of 10 mmHg. Second, in our study the $PaCO_2$ was known from the $PETCO_2$ (143). This relationship has only been shown to hold for sequential rebreathing, as used by prospective targeting (143,182). Third, in our subjects, normoxia was maintained to avoid vasoconstriction.

The recent study by Beaudin et al (140) is particularly relevant to our study. These investigators applied an euoxic hypercapnic stimulus of 9 mmHg in humans and measured the effect on coronary sinus blood flow with MRI. They found that myocardial blood flow (indexed by coronary sinus flow) increased by 34±4.6% similar to that of cerebral blood flow. After accounting for the increase in myocardial blood flow due to the work-induced increase in MVO_2,

the increase in myocardial blood flow, representing that from vasodilation alone, was 17.1±5.7%. This study, with a few caveats, is comparable to ours. Beaudin et al (140) implemented a 14-second breath-hold to enable the cardiac MR-based coronary sinus blood flow measures. Such breath-hold induces further substantial hypercapnia, and rapidly developing hypoxia (183), both potent coronary artery vasodilators. Although outside of the breath-hold, Beaudin et al (140) accurately target $PETCO_2$ and $PETO_2$, unlike prospective targeting methods, these values do not reliably reflect the arterial values (184). Finally, the flow data was derived as a product of the cross-sectional area of the coronary sinus (measured from MR images) and the through-plane velocity of the blood. Given the size of the coronary sinus and the spatial/temporal resolution of the imaging, there may be significant differences between the actual size of the coronary sinus and that designated. Nevertheless, both their study and ours support consideration of hypercapnia as a stimulus for cardiac stress test.

5.2.4.2 Advantages and Disadvantages and Limitations of Hypercapnia and Myocardial BOLD MR

Hypercapnia of about 10 mmHg from baseline is benign since it is within the physiologic range and is commonly experienced in day-to-day living by most people ((185,186). With few exceptions (e.g., increased intracranial pressure) there is no known risk or contra-indication to an increase of $PaCO_2$ of 10 mmHg. The main effects of hypercapnia are dyspnea, and in some, stimulation of the sympathetic nervous system resulting in increase in heart rate and blood pressure. In a study of 400 consecutive patients undergoing a 10 mmHg increase in $PETCO_2$ for cerebral blood flow studies using BOLD MRI, over 90% of subjects tolerated the stimulus (172). While we expect this number to be lower than 10% in the cardiac setting, there will likely be patients who will not tolerate this procedure. While there are ways to identify such patient

population through a short screening test (examination of tolerance to short hypercapnic stimulus as we have done in this study) prior to undergoing imaging, we do not expect that hypercapnic stimulus will become an exclusive provocative agent for cardiac stress testing in all subjects. Those that cannot tolerate or are contraindicated for hypercapnic stimulus may need to resort to pharmacological stress test should that be a suitable option for them. In every case, the sensation of dyspnea, resolved within 2-4 breaths with restoration of normocapnia.

As BOLD contrast is based on the oxygen saturation of hemoglobin, it reflects the balance between oxygen supply and demand, a feature of value in the assessment of ischemic heart disease. This feature of myocardial BOLD MRI differs from standard perfusion imaging methods that provide information only on blood supply but not demand (187). In the healthy myocardium, adenosine infusion has been reported to elicit BOLD responses that are between 10 – 25% 3T (62,175), with the individual amplitude of response determined by the specific imaging approach. Among the various imaging approaches, T_2-prep scheme has been studied by a number of different investigators and have also been validated against microspheres (31). In particular, the T_2-prep SSFP approaches at 3T (175) has shown mean hyperemic BOLD response from healthy myocardium between 15-17%. In this study we showed that the free-breathing BOLD response at 3T using the T_2-prepared SSFP acquisition scheme is 14±24% with adenosine and 17±14% with hypercapnia in canines, which are consistent with previous reports.

5.2.4.3 Study Limitations

Healthy human subjects were exposed only to hypercapnia but not adenosine as we considered it necessary to compare available data before performing invasive tests. We chose a 10 mmHg hypercapnic stimulus for the human studies because considerable experience exists with this

'dose' in an elderly population with cerebrovascular disease (172), presumably with similar comorbidities (including ventilatory limitations) to those in patients with coronary disease.

While the observed coronary blood flow velocity responses in canines were similar to previous reports, some groups have shown that coronary blood flow velocity reserves in excess of 2.0 in healthy subjects (138,188). These latter differences likely stem from the differences in coronary blood flow velocity measurement position along the coronary artery (188). Moreover, since our stenosis studies relied on knowing the peak blood flow velocity prior to creation of hypoperfusion, we were unable to randomize the $PaCO_2$ levels. Given that the LAD constriction likely only introduced hypoperfusion and not ischemia, we do not anticipate the non-randomization of $PETCO_2$ between 40 mmHg and 60 mmHg to have any effect on our findings. However, additional studies are needed to confirm this.

In this study, we only evaluated one level of stenosis. Stenosis was created by reducing the blood flow to baseline levels in LAD under hypercapnia of 60 mmHg; hence, the true reduction of coronary diameter was not available to us. This aspect of the study was intended only as a proof of principle for identifying redistributions of blood flow and comparing the extent to that of adenosine for perspective.

To the best of our knowledge there are no validation studies in the literature for defining perfusion deficit territories based on signal thresholding of first-pass perfusion MR images. In this study with limited sample size, we observed that visual assessment of perfusion territories to correspond closely to 1SD decrease in segmental signal intensity relative to remote segments. However, the same analysis with 2SD criterion tended to underestimate the segments with perfusion defects, which may be explained on the basis of number of factors. Among these,

partial volume effects, extent of perfusion territory, and animal-to-animal variation in supply territory of the coronary arteries are some viable reasons. A more thorough analysis is expected to be necessary to establish a viable criterion, which is outside the scope of this study.

This was an exploratory study. We anticipate that additional studies are necessary before hypercapnia can be considered a suitable stimulus for cardiac stress testing.

Chapter 6 Summary and Future Directions

6.1 SUMMARY

Assessment of myocardial perfusion is critical in the functional characterization of CAD. FPP-MRI is a high resolution and non-radioactive approach for probing myocardial perfusion. However, it requires administration of a Gadolinium based contrast agent, which is contraindicated in patients with end-stage chronic kidney disease (CKD). Myocardial blood-oxygen-level-dependent (BOLD) CMR is a non-contrast and ionizing-radiation-free approach for examining myocardial perfusion. It has the capacity to fill the need to assess myocardial repeat assessment of myocardial perfusion in the CKD patients, who have high prevalence of coronary artery disease. Despite previous advancements, BOLD CMR is still limited by one or more of the following challenges: inadequate spatial coverage, imaging speed, imaging cofounders, need for multiple breath holds and imaging artifacts, particularly at 3T. In chapter 3 of this dissertation, a 3D whole-heart, fast quantitative BOLD sequence is developed and validated with simultaneously acquired quantitative N^{13}-ammonia PET perfusion. The technique was developed to address the current limitations and build a reliable method to acquire fast, robust and reliable BOLD images. In chapter 3.1, a high efficiency imaging platform was developed to acquire free-breathing, whole-heart T2 mapping under resting condition within 5 minutes at 3T. The platform utilizes affine transforms to correct for respiratory motion and achieves near perfect imaging efficiency during free-breathing. It also addresses imaging artifacts at 3T with well-designed adiabatic T2 preparation and GRE readouts. The technique was validated with commercially available 2D techniques and showed the capability of detecting myocardial edema in animals

with acute myocardial infarction. This was recently published in Magnetic Resonance in Medicine.

In chapter 3.2, the T2 mapping platform is extended and tailored for BOLD CMR ischemic testing by incorporating an SR preparation pulse and optimized imaging trajectory and parameters. The approach further reduces the acquisition time while eliminating a key confounder of the BOLD signal. These improvements enable the technique to accommodate short and unstable imaging window under vasodilatory stress. The method was implemented and tested in canine models and human subjects. The BOLD effect was validated in a state of the art clinical PET/MR scanner with simultaneously acquired quantitative ^{13}N-ammonia PET perfusion images. This is also the first demonstration of the correlation between cardiac BOLD signal and quantitative PET perfusion under identical physiological conditions. This work has been published in an abstract form in the 2016 SCMR annual meeting and a full manuscript is currently under review by JACC: Cardiovascular Imaging.

Future studies should investigate the applicability of the proposed technique in patients. In addition, this fast and reliable BOLD CMR acquisition technique, when integrated the innovative vasodilation strategies developed in chapter 4 and 5, has the capacity to markedly improve the current state of BOLD CMR.

Besides the MR technical developments, this dissertation also pushes forward the imaging reliability through the advancements of new strategies for examining coronary vasodilation. Chapter 4 and 5 explore innovative imaging prtocols with two newer vasodilators (Regadenoson and Hypercapnia) to enable more suitable imaging environments for BOLD CMR.

The current vasodilation strategies for ischemia testing are designed for other imaging modalities, which depend of first-passage of a contrast agent. Improved vasodilation methods that can take advantages of BOLD CMR, such as repeat measurements, while minimizing the shortcomings can significantly increase the reliability of the exam and assist in the reliable application of BOLD CMR in the clinical settings. In chapter 4, regadenoson, a clinically available vasodilator, is explored for BOLD CMR acquisition. The study in chapter 4.1 takes advantage of the longer physiological half-life of regadenoson and explores the delayed vasodilation effect by acquiring BOLD images at a time point with more stable cardiac conditions. The results show significantly improved robustness in image quality and reliability for evaluating BOLD signal changes compared to the standard approach. This effect was tested in animals and validated with ^{13}N-ammonia PET perfusion. The study has been published in abstract form in the JCMR 2016 and was nominated for the early career award in the 2016 SCMR annual Meeting.

The study in chapter 4.2 takes the method one step further to explore the full time course of coronary vasodilation with repeatedly acquired BOLD images. The study explores post regadenoson coronary dynamics in animal models under conditions of health and disease by monitoring BOLD signal changes in the myocardium. Significant CDP differences between healthy and affected myocardial territories were observed in the study. CDPs showed high accuracy for detecting affected myocardium. The preliminary results from chapter 4 demonstrate the potential of improving reliability and sensitivity of cardiac BOLD exams with better designed vasodilation and imaging strategies. Further investigations are needed for the single time point regadenoson BOLD exam to determine the best imaging timing. It is expected that one needs to optimize the trade-off between imaging robustness and the level of vasodilation to

reliably detect CAD. In addition, the preliminary CDP studies in the dissertation are performed in animal models and healthy human volunteers. The connection between the CDPs and the coronary physiological condition in patients remains to be explored.

Chapter 5 explores vasodilation effect with controlled arterial CO2 level and its applicability in cardiac BOLD MRI. Unlike the conventional pharmacological stress agents, CO2 is an intrinsic molecule that can be noninvasively modulated through respiratory system. Utilizing hypercapnia in cardiac BOLD exams can potentially reduce the risk of the adverse side effects from the conventional pharmacological stress agents and increases exam reliability with repeat stimulations. The capability of inducing vasodilation with controlled hypercapnia is first examined in chapter 5.1 with PET. Quantitative ^{13}N-ammonia PET was used in animals with and without coronary stenosis to investigate the vasodilatory capacity of the coronary arteries during hypercapnia with a computerized gas control delivery system to precisely target the arterial CO2 level. This work showed that controlled iso-oxic hypercapnia can increase myocardial blood flow to a comparable extent of adenosine and provide similar capability in ischemic volume identification. This work has been published in an abstract form in the 2016 AHA annual meeting and is currently under review by JACC: Basic to Translational Science.

The efficacy of hypercapnic vasodilation in BOLD CMR exam is further explored in chapter 5.2. The study investigated the BOLD response induced by hypercapnia in human volunteers and animal models. The result showed the hypercapnic BOLD response is comparable to the standard clinical dose adenosine and has similar capability of identifying ischemic territories. In addition, the study established the reversible and repeatable BOLD responses following repeat hypercapnic stimulations, which would allow for repetitive rest and stress alternation at a single

session. This work has been published in the Radiology in 2014. Future directions to extend BOLD CMR through the use of our findings here are discussed in the following section.

6.2 Next Steps: Cardiac Functional MRI with CO_2 Stimulation Paradigm

The fundamental limitations of BOLD MRI associated with reliable detection of myocardial ischemia stems from its inherently low sensitivity and specificity due to low BOLD contrast-to-noise ratio (CNR). In integrating the developments in this dissertation, we expect to overcome these barriers through: (i). Utilizing the developed technique in chapter 3 to acquire 3D images at 3T (instead of 1.5T) to increase BOLD CNR and perform high-resolution, free-breathing, BOLD imaging to ensure rapid data collection, volumetric coverage, with free gas-exchange capability; and (ii). Employment of general linear model (GLM) data analysis to further improve sensitivity and specificity with repeat stimulation using the prospective CO_2 targeting technique developed in chapter 5.

GLM analysis is one of the primary reasons for the success of BOLD MRI in the brain, which was also limited by sensitivity and specificity in the early days (35). At the core of GLM is a regression analysis that determines the statistical significance between repeated stimuli and the associated (repeated) measured responses. In the brain, the stimulus is easily repeatable (i.e. they are visual or cognitive) and leads to vasodilation and a concomitant BOLD response. To date, myocardial BOLD responses are induced via intravenously injected stimulus, adenosine, and cannot be repeated due to its adverse side effects and costs. Based on our findings in chapter 5, we will anticipate that precisely targeted PaCO2 may evolve as a noninvasive alternative to adenosine to repeatedly stimulate the heart and measure the responses with the 3D BOLD CMRI (as developed in chapter 3). The PaCO2-based repeat stimulations have the capacity to provide a

unique opportunity to capture the BOLD signal across multiple data sets. This can offer unprecedented amplification in sensitivity and specificity for a reliable and noninvasive means for evaluating the myocardial perfusion reserve on the basis of BOLD CMR.

Efforts from the past 20 years in the field of cardiac BOLD MRI have finally pushed the technique in the sight of clinical applications. The studies in this dissertation are expected to pave the way for more reliable detection and quantification of ischemic volume and to close the gap between research and clinical settings. Hence push BOLD CMR forward as a clinical useful instrument to benefit the needed patients and improve patient outcomes.

Reference

1. Writing Group M, Mozaffarian D, Benjamin EJ et al. Heart Disease and Stroke Statistics-2016 Update: A Report From the American Heart Association. Circulation 2016;133:e38-360.
2. Hachamovitch R, Hayes SW, Friedman JD, Cohen I, Berman DS. Comparison of the short-term survival benefit associated with revascularization compared with medical therapy in patients with no prior coronary artery disease undergoing stress myocardial perfusion single photon emission computed tomography. Circulation 2003;107:2900-7.
3. Hachamovitch R, Berman DS. The use of nuclear cardiology in clinical decision making. Semin Nucl Med 2005;35:62-72.
4. Shaw LJ, Berman DS, Maron DJ et al. Optimal medical therapy with or without percutaneous coronary intervention to reduce ischemic burden: results from the Clinical Outcomes Utilizing Revascularization and Aggressive Drug Evaluation (COURAGE) trial nuclear substudy. Circulation 2008;117:1283-91.
5. Weintraub WS, Spertus JA, Kolm P et al. Effect of PCI on quality of life in patients with stable coronary disease. N Engl J Med 2008;359:677-87.
6. Group BDS, Frye RL, August P et al. A randomized trial of therapies for type 2 diabetes and coronary artery disease. N Engl J Med 2009;360:2503-15.
7. Boden WE, O'Rourke RA, Teo KK et al. Optimal medical therapy with or without PCI for stable coronary disease. N Engl J Med 2007;356:1503-16.
8. Pijls NH, van Schaardenburgh P, Manoharan G et al. Percutaneous coronary intervention of functionally nonsignificant stenosis: 5-year follow-up of the DEFER Study. Journal of the American College of Cardiology 2007;49:2105-11.

9. Tonino PA, De Bruyne B, Pijls NH et al. Fractional flow reserve versus angiography for guiding percutaneous coronary intervention. N Engl J Med 2009;360:213-24.

10. Pijls NH, Fearon WF, Tonino PA et al. Fractional flow reserve versus angiography for guiding percutaneous coronary intervention in patients with multivessel coronary artery disease: 2-year follow-up of the FAME (Fractional Flow Reserve Versus Angiography for Multivessel Evaluation) study. Journal of the American College of Cardiology 2010;56:177-84.

11. Gershlick AH, de Belder M, Chambers J et al. Role of non-invasive imaging in the management of coronary artery disease: an assessment of likely change over the next 10 years. A report from the British Cardiovascular Society Working Group. Heart 2007;93:423-31.

12. Berman DS, Hachamovitch R, Shaw LJ et al. Roles of nuclear cardiology, cardiac computed tomography, and cardiac magnetic resonance: Noninvasive risk stratification and a conceptual framework for the selection of noninvasive imaging tests in patients with known or suspected coronary artery disease. Journal of nuclear medicine : official publication, Society of Nuclear Medicine 2006;47:1107-18.

13. Porter TR, Xie F. Myocardial perfusion imaging with contrast ultrasound. JACC Cardiovascular imaging 2010;3:176-87.

14. Greenwood JP, Maredia N, Younger JF et al. Cardiovascular magnetic resonance and single-photon emission computed tomography for diagnosis of coronary heart disease (CE-MARC): a prospective trial. Lancet 2012;379:453-60.

15. Shaw LJ, Marwick TH, Zoghbi WA et al. Why all the focus on cardiac imaging? JACC Cardiovascular imaging 2010;3:789-94.

16. Miller TD, Hodge DO, Christian TF, Milavetz JJ, Bailey KR, Gibbons RJ. Effects of adjustment for referral bias on the sensitivity and specificity of single photon emission computed tomography for the diagnosis of coronary artery disease. The American journal of medicine 2002;112:290-7.

17. Kuo PH, Kanal E, Abu-Alfa AK, Cowper SE. Gadolinium-based MR contrast agents and nephrogenic systemic fibrosis. Radiology 2007;242:647-9.

18. Friedrich MG, Niendorf T, Schulz-Menger J, Gross CM, Dietz R. Blood oxygen level-dependent magnetic resonance imaging in patients with stress-induced angina. Circulation 2003;108:2219-23.

19. Karamitsos TD, Leccisotti L, Arnold JR et al. Relationship between regional myocardial oxygenation and perfusion in patients with coronary artery disease: insights from cardiovascular magnetic resonance and positron emission tomography. Circulation Cardiovascular imaging 2010;3:32-40.

20. Jahnke C, Gebker R, Manka R, Schnackenburg B, Fleck E, Paetsch I. Navigator-gated 3D blood oxygen level-dependent CMR at 3.0-T for detection of stress-induced myocardial ischemic reactions. JACC Cardiovascular imaging 2010;3:375-84.

21. Marckmann P, Skov L, Rossen K et al. Nephrogenic systemic fibrosis: suspected causative role of gadodiamide used for contrast-enhanced magnetic resonance imaging. Journal of the American Society of Nephrology : JASN 2006;17:2359-62.

22. High WA, Ayers RA, Chandler J, Zito G, Cowper SE. Gadolinium is detectable within the tissue of patients with nephrogenic systemic fibrosis. J Am Acad Dermatol 2007;56:21-6.

23. Larson K, Gagnon A, Darling M, Patterson J, Cropley T. Nephrogenic Systemic Fibrosis Manifesting a Decade After Exposure to Gadolinium. JAMA Dermatol 2015;doi: 10.1001/jamadermatol.2015.0976.

24. Yancy CW, Jessup M, Bozkurt B et al. 2013 ACCF/AHA guideline for the management of heart failure: a report of the American College of Cardiology Foundation/American Heart Association Task Force on practice guidelines. Circulation 2013;128:e240-327.

25. Heywood JT, Fonarow GC, Costanzo MR, Mathur VS, Wigneswaran JR, Wynne J. High prevalence of renal dysfunction and its impact on outcome in 118,465 patients hospitalized with acute decompensated heart failure: a report from the ADHERE database. 2007;13:422-30.

26. Ahmed A, Campbell RC. Epidemiology of chronic kidney disease in heart failure. 2008;4:387-99.

27. Sarnak MJ, Levey AS, Schoolwerth AC et al. Kidney disease as a risk factor for development of cardiovascular disease: a statement from the American Heart Association Councils on Kidney in Cardiovascular Disease, High Blood Pressure Research, Clinical Cardiology, and Epidemiology and Prevention. Circulation 2003;108:2154-69.

28. Gansevoort RT, Correa-Rotter R, Hemmelgarn BR et al. Chronic kidney disease and cardiovascular risk: epidemiology, mechanisms, and prevention. Lancet 2013;382:339-52.

29. Atalay MK, Forder JR, Chacko VP, Kawamoto S, Zerhouni EA. Oxygenation in the rabbit myocardium: assessment with susceptibility-dependent MR imaging. Radiology 1993;189:759-64.

30. Foltz WD, Huang H, Fort S, Wright GA. Vasodilator response assessment in porcine myocardium with magnetic resonance relaxometry. Circulation 2002;106:2714-9.

31. Fieno DS, Shea SM, Li Y, Harris KR, Finn JP, Li D. Myocardial perfusion imaging based on the blood oxygen level-dependent effect using T2-prepared steady-state free-precession magnetic resonance imaging. Circulation 2004;110:1284-90.

32. Dharmakumar R, Arumana JM, Larson AC, Chung Y, Wright GA, Li D. Cardiac phase-resolved blood oxygen-sensitive steady-state free precession MRI for evaluating the functional significance of coronary artery stenosis. Investigative radiology 2007;42:180-8.

33. Zheng J, Wang J, Rowold FE, Gropler RJ, Woodard PK. Relationship of apparent myocardial T2 and oxygenation: towards quantification of myocardial oxygen extraction fraction. Journal of magnetic resonance imaging : JMRI 2004;20:233-41.

34. Miyamoto MI, Vernotico SL, Majmundar H, GS T. Pharmacologic stress myocardial perfusion imaging: a practical approach. Journal of nuclear cardiology : official publication of the American Society of Nuclear Cardiology 2007.

35. K. J. Friston, A. P. Holmes, K. J. Worsley, J.-P. Poline, C. D. Frith, Frackowiak RSJ. Statistical parametric maps in functional imaging: A general linear approach. Human Brain Mapping 1994.

36. Hendel RC, Berman DS, Di Carli MF et al. ACCF/ASNC/ACR/AHA/ASE/SCCT/SCMR/SNM 2009 Appropriate Use Criteria for Cardiac Radionuclide Imaging: A Report of the American College of Cardiology Foundation Appropriate Use Criteria Task Force, the American Society of Nuclear Cardiology, the American College of Radiology, the American Heart Association, the

American Society of Echocardiography, the Society of Cardiovascular Computed Tomography, the Society for Cardiovascular Magnetic Resonance, and the Society of Nuclear Medicine. Journal of the American College of Cardiology 2009;53:2201-29.

37. Klocke FJ, Baird MG, Lorell BH et al. ACC/AHA/ASNC guidelines for the clinical use of cardiac radionuclide imaging--executive summary: a report of the American College of Cardiology/American Heart Association Task Force on Practice Guidelines (ACC/AHA/ASNC Committee to Revise the 1995 Guidelines for the Clinical Use of Cardiac Radionuclide Imaging). Circulation 2003;108:1404-18.

38. Gould KL. Does coronary flow trump coronary anatomy? JACC Cardiovascular imaging 2009;2:1009-23.

39. Meijboom WB, Van Mieghem CA, van Pelt N et al. Comprehensive assessment of coronary artery stenoses: computed tomography coronary angiography versus conventional coronary angiography and correlation with fractional flow reserve in patients with stable angina. Journal of the American College of Cardiology 2008;52:636-43.

40. Koolen JJ, Pijls NH. Coronary pressure never lies. Catheterization and cardiovascular interventions : official journal of the Society for Cardiac Angiography & Interventions 2008;72:248-56.

41. Ladapo JA, Blecker S, Douglas PS. Physician decision making and trends in the use of cardiac stress testing in the United States: an analysis of repeated cross-sectional data. Annals of internal medicine 2014;161:482-90.

42. Feigl EO. Coronary physiology. Physiol Rev 1983;63:1-205.

43. Duncker DJ, Bache RJ. Regulation of coronary vasomotor tone under normal conditions and during acute myocardial hypoperfusion. Pharmacology & therapeutics 2000;86:87-110.

44. NEJM. Coronary disfunction. 2014.

45. Yang HJ, Yumul R, Tang R et al. Assessment of myocardial reactivity to controlled hypercapnia with free-breathing T2-prepared cardiac blood oxygen level-dependent MR imaging. Radiology 2014;272:397-406.

46. Fischer K, Guensch DP, Friedrich MG. Response of myocardial oxygenation to breathing manoeuvres and adenosine infusion. European heart journal cardiovascular Imaging 2015;16:395-401.

47. Jensen KP, Ryde U. How O2 binds to heme: reasons for rapid binding and spin inversion. The Journal of biological chemistry 2004;279:14561-9.

48. Wang Y, Liu T. Quantitative susceptibility mapping (QSM): Decoding MRI data for a tissue magnetic biomarker. Magnetic resonance in medicine 2015;73:82-101.

49. Ferris CF, Febo M, Luo F et al. Functional magnetic resonance imaging in conscious animals: a new tool in behavioural neuroscience research. Journal of neuroendocrinology 2006;18:307-18.

50. Ogawa S, Lee TM, Kay AR, Tank DW. Brain magnetic resonance imaging with contrast dependent on blood oxygenation. Proceedings of the National Academy of Sciences of the United States of America 1990;87:9868-72.

51. Ogawa S, Tank DW, Menon R et al. Intrinsic signal changes accompanying sensory stimulation: functional brain mapping with magnetic resonance imaging. Proceedings of the National Academy of Sciences of the United States of America 1992;89:5951-5.

52. Kwong KK, Belliveau JW, Chesler DA et al. Dynamic magnetic resonance imaging of human brain activity during primary sensory stimulation. Proceedings of the National Academy of Sciences of the United States of America 1992;89:5675-9.

53. Kaul S, Jayaweera AR. Coronary and myocardial blood volumes: noninvasive tools to assess the coronary microcirculation? Circulation 1997;96:719-24.

54. Wacker CM, Hartlep AW, Pfleger S, Schad LR, Ertl G, Bauer WR. Susceptibility-sensitive magnetic resonance imaging detects human myocardium supplied by a stenotic coronary artery without a contrast agent. Journal of the American College of Cardiology 2003;41:834-40.

55. Wendland MF, Saeed M, Lauerma K, de Crespigny A, Moseley ME, Higgins CB. Endogenous susceptibility contrast in myocardium during apnea measured using gradient recalled echo planar imaging. Magnetic resonance in medicine 1993;29:273-6.

56. Li D, Dhawale P, Rubin PJ, Haacke EM, Gropler RJ. Myocardial signal response to dipyridamole and dobutamine: demonstration of the BOLD effect using a double-echo gradient-echo sequence. Magnetic resonance in medicine 1996;36:16-20.

57. Wacker CM, Bock M, Hartlep AW et al. Changes in myocardial oxygenation and perfusion under pharmacological stress with dipyridamole: assessment using T*2 and T1 measurements. Magnetic resonance in medicine 1999;41:686-95.

58. Boxerman JL, Hamberg LM, Rosen BR, Weisskoff RM. MR contrast due to intravascular magnetic susceptibility perturbations. Magnetic resonance in medicine 1995;34:555-66.

59. Zheng J. Assessment of myocardial oxygenation with MRI. Quantitative imaging in medicine and surgery 2013;3:67-72.

60. Tsaftaris SA, Zhou X, Tang R, Li D, Dharmakumar R. Detecting myocardial ischemia at rest with cardiac phase-resolved blood oxygen level-dependent cardiovascular magnetic resonance. Circulation Cardiovascular imaging 2013;6:311-9.

61. Gati JS, Menon RS, Ugurbil K, Rutt BK. Experimental determination of the BOLD field strength dependence in vessels and tissue. Magnetic resonance in medicine 1997;38:296-302.

62. Dharmakumar R, Arumana JM, Tang R, Harris K, Zhang Z, Li D. Assessment of regional myocardial oxygenation changes in the presence of coronary artery stenosis with balanced SSFP imaging at 3.0 T: theory and experimental evaluation in canines. Journal of magnetic resonance imaging : JMRI 2008;27:1037-45.

63. Shea SM, Fieno DS, Schirf BE et al. T2-prepared steady-state free precession blood oxygen level-dependent MR imaging of myocardial perfusion in a dog stenosis model. Radiology 2005;236:503-9.

64. Bernhardt P, Manzke R, Bornstedt A et al. Blood oxygen level-dependent magnetic resonance imaging using T2-prepared steady-state free-precession imaging in comparison to contrast-enhanced myocardial perfusion imaging. International journal of cardiology 2011;147:416-9.

65. Karamitsos TD, Arnold JR, Pegg TJ et al. Patients with syndrome X have normal transmural myocardial perfusion and oxygenation: a 3-T cardiovascular magnetic resonance imaging study. Circulation Cardiovascular imaging 2012;5:194-200.

66. Walcher T, Manzke R, Hombach V, Rottbauer W, Wohrle J, Bernhardt P. Myocardial perfusion reserve assessed by T2-prepared steady-state free precession blood oxygen

level-dependent magnetic resonance imaging in comparison to fractional flow reserve. Circulation Cardiovascular imaging 2012;5:580-6.

67. Arnold S, Victor MB, Beyer C. Estrogen and the regulation of mitochondrial structure and function in the brain. The Journal of steroid biochemistry and molecular biology 2012;131:2-9.

68. Tsaftaris SA, Tang R, Zhou X, Li D, Dharmakumar R. Ischemic extent as a biomarker for characterizing severity of coronary artery stenosis with blood oxygen-sensitive MRI. Journal of magnetic resonance imaging : JMRI 2012;35:1338-48.

69. Abdel-Aty H, Zagrosek A, Schulz-Menger J et al. Delayed enhancement and T2-weighted cardiovascular magnetic resonance imaging differentiate acute from chronic myocardial infarction. Circulation 2004;109:2411-6.

70. Friedrich MG, Sechtem U, Schulz-Menger J et al. Cardiovascular magnetic resonance in myocarditis: A JACC White Paper. Journal of the American College of Cardiology 2009;53:1475-87.

71. Verhaert D, Thavendiranathan P, Giri S et al. Direct T2 quantification of myocardial edema in acute ischemic injury. JACC Cardiovascular imaging 2011;4:269-78.

72. Usman AA, Taimen K, Wasielewski M et al. Cardiac magnetic resonance T2 mapping in the monitoring and follow-up of acute cardiac transplant rejection: a pilot study. Circulation Cardiovascular imaging 2012;5:782-90.

73. Payne AR, Casey M, McClure J et al. Bright-blood T2-weighted MRI has higher diagnostic accuracy than dark-blood short tau inversion recovery MRI for detection of acute myocardial infarction and for assessment of the ischemic area at risk and myocardial salvage. Circulation Cardiovascular imaging 2011;4:210-9.

74. He T, Gatehouse PD, Smith GC, Mohiaddin RH, Pennell DJ, Firmin DN. Myocardial T2* measurements in iron-overloaded thalassemia: An in vivo study to investigate optimal methods of quantification. Magnetic resonance in medicine : official journal of the Society of Magnetic Resonance in Medicine / Society of Magnetic Resonance in Medicine 2008;60:1082-9.

75. Papanikolaou N, Ghiatas A, Kattamis A, Ladis C, Kritikos N, Kattamis C. Non-invasive myocardial iron assessment in thalassaemic patients. T2 relaxometry and magnetization transfer ratio measurements. Acta radiologica 2000;41:348-51.

76. Arnold JR, Karamitsos TD, Bhamra-Ariza P et al. Myocardial oxygenation in coronary artery disease: insights from blood oxygen level-dependent magnetic resonance imaging at 3 tesla. Journal of the American College of Cardiology 2012;59:1954-64.

77. Kellman P, Aletras AH, Mancini C, McVeigh ER, Arai AE. T2-prepared SSFP improves diagnostic confidence in edema imaging in acute myocardial infarction compared to turbo spin echo. Magn Reson Med 2007;57:891-7.

78. Abdel-Aty H, Simonetti O, Friedrich MG. T2-weighted cardiovascular magnetic resonance imaging. Journal of magnetic resonance imaging : JMRI 2007;26:452-9.

79. Giri S, Chung YC, Merchant A et al. T2 quantification for improved detection of myocardial edema. Journal of cardiovascular magnetic resonance : official journal of the Society for Cardiovascular Magnetic Resonance 2009;11:56.

80. Thavendiranathan P, Walls M, Giri S et al. Improved detection of myocardial involvement in acute inflammatory cardiomyopathies using T2 mapping. Circulation Cardiovascular imaging 2012;5:102-10.

81. He T, Gatehouse PD, Anderson LJ et al. Development of a novel optimized breathhold technique for myocardial T2 measurement in thalassemia. Journal of magnetic resonance imaging : JMRI 2006;24:580-5.

82. Guo S, Bozkaya D, Ward A et al. Treating relapsing multiple sclerosis with subcutaneous versus intramuscular interferon-beta-1a: modelling the clinical and economic implications. PharmacoEconomics 2009;27:39-53.

83. van Heeswijk RB, Feliciano H, Bongard C et al. Free-breathing 3 T magnetic resonance T2-mapping of the heart. JACC Cardiovascular imaging 2012;5:1231-9.

84. Giri S, Shah S, Xue H et al. Myocardial T(2) mapping with respiratory navigator and automatic nonrigid motion correction. Magnetic resonance in medicine : official journal of the Society of Magnetic Resonance in Medicine / Society of Magnetic Resonance in Medicine 2012;68:1570-8.

85. Raman SV, Simonetti OP, Winner MW, 3rd et al. Cardiac magnetic resonance with edema imaging identifies myocardium at risk and predicts worse outcome in patients with non-ST-segment elevation acute coronary syndrome. Journal of the American College of Cardiology 2010;55:2480-8.

86. Abdel-Aty H, Cocker M, Meek C, Tyberg JV, Friedrich MG. Edema as a very early marker for acute myocardial ischemia: a cardiovascular magnetic resonance study. Journal of the American College of Cardiology 2009;53:1194-201.

87. Gerber BL, Raman SV, Nayak K et al. Myocardial first-pass perfusion cardiovascular magnetic resonance: history, theory, and current state of the art. Journal of cardiovascular magnetic resonance : official journal of the Society for Cardiovascular Magnetic Resonance 2008;10:18.

88. Schar M, Kozerke S, Fischer SE, Boesiger P. Cardiac SSFP imaging at 3 Tesla. Magnetic resonance in medicine : official journal of the Society of Magnetic Resonance in Medicine / Society of Magnetic Resonance in Medicine 2004;51:799-806.

89. Nezafat R, Stuber M, Ouwerkerk R, Gharib AM, Desai MY, Pettigrew RI. B1-insensitive T2 preparation for improved coronary magnetic resonance angiography at 3 T. Magnetic resonance in medicine : official journal of the Society of Magnetic Resonance in Medicine / Society of Magnetic Resonance in Medicine 2006;55:858-64.

90. Jenista ER, Rehwald WG, Chen EL et al. Motion and flow insensitive adiabatic T2 - preparation module for cardiac MR imaging at 3 Tesla. Magnetic resonance in medicine : official journal of the Society of Magnetic Resonance in Medicine / Society of Magnetic Resonance in Medicine 2013;70:1360-8.

91. Stuber M, Botnar RM, Danias PG, Kissinger KV, Manning WJ. Submillimeter three-dimensional coronary MR angiography with real-time navigator correction: comparison of navigator locations. Radiology 1999;212:579-87.

92. Bhat H, Ge L, Nielles-Vallespin S, Zuehlsdorff S, Li D. 3D radial sampling and 3D affine transform-based respiratory motion correction technique for free-breathing whole-heart coronary MRA with 100% imaging efficiency. Magnetic resonance in medicine : official journal of the Society of Magnetic Resonance in Medicine / Society of Magnetic Resonance in Medicine 2011;65:1269-77.

93. Manke D, Nehrke K, Bornert P. Novel prospective respiratory motion correction approach for free-breathing coronary MR angiography using a patient-adapted affine motion model. Magnetic resonance in medicine : official journal of the Society of

Magnetic Resonance in Medicine / Society of Magnetic Resonance in Medicine 2003;50:122-31.

94. Luis I SW, Ng L, Cates J, and the Insight Software Consortium, (www.itk.org). The ITK Software Guide, 2nd Ed. Updated for ITK version 2.4. 2.4 ed, 2005.

95. Kali A, Cokic I, Tang RL et al. Determination of location, size, and transmurality of chronic myocardial infarction without exogenous contrast media by using cardiac magnetic resonance imaging at 3 T. Circulation Cardiovascular imaging 2014;7:471-81.

96. Sharif B, Dharmakumar R, Arsanjani R et al. Non-ECG-gated myocardial perfusion MRI using continuous magnetization-driven radial sampling. Magnetic resonance in medicine : official journal of the Society of Magnetic Resonance in Medicine / Society of Magnetic Resonance in Medicine 2014.

97. van Heeswijk RB, Piccini D, Feliciano H, Hullin R, Schwitter J, Stuber M. Self-navigated isotropic three-dimensional cardiac T mapping. Magnetic resonance in medicine : official journal of the Society of Magnetic Resonance in Medicine / Society of Magnetic Resonance in Medicine 2014.

98. Wassmuth R, Prothmann M, Utz W et al. Variability and homogeneity of cardiovascular magnetic resonance myocardial T2-mapping in volunteers compared to patients with edema. Journal of cardiovascular magnetic resonance : official journal of the Society for Cardiovascular Magnetic Resonance 2013;15:27.

99. Ghugre NR, Pop M, Barry J, Connelly KA, Wright GA. Quantitative magnetic resonance imaging can distinguish remodeling mechanisms after acute myocardial infarction based on the severity of ischemic insult. Magnetic resonance in medicine : official journal of

the Society of Magnetic Resonance in Medicine / Society of Magnetic Resonance in Medicine 2013;70:1095-105.

100. Pang J, Sharif B, Arsanjani R et al. Accelerated whole-heart coronary MRA using motion-corrected sensitivity encoding with three-dimensional projection reconstruction. Magnetic resonance in medicine : official journal of the Society of Magnetic Resonance in Medicine / Society of Magnetic Resonance in Medicine 2014.

101. Wright KL, Hamilton JI, Griswold MA, Gulani V, Seiberlich N. Non-Cartesian parallel imaging reconstruction. Journal of magnetic resonance imaging : JMRI 2014.

102. Doneva M, Bornert P, Eggers H, Stehning C, Senegas J, Mertins A. Compressed sensing reconstruction for magnetic resonance parameter mapping. Magnetic resonance in medicine : official journal of the Society of Magnetic Resonance in Medicine / Society of Magnetic Resonance in Medicine 2010;64:1114-20.

103. MacFall JR, Riederer SJ, Wang HZ. An analysis of noise propagation in computed T2, pseudodensity, and synthetic spin-echo images. Medical physics 1986;13:285-92.

104. von Knobelsdorff-Brenkenhoff F, Prothmann M, Dieringer MA et al. Myocardial T1 and T2 mapping at 3 T: reference values, influencing factors and implications. Journal of cardiovascular magnetic resonance : official journal of the Society for Cardiovascular Magnetic Resonance 2013;15:53.

105. Pang J, Bhat H, Sharif B et al. Whole-heart coronary MRA with 100% respiratory gating efficiency: self-navigated three-dimensional retrospective image-based motion correction (TRIM). Magnetic resonance in medicine : official journal of the Society of Magnetic Resonance in Medicine / Society of Magnetic Resonance in Medicine 2014;71:67-74.

106. Hachamovitch R. Impact of ischemia and scar on therapeutic benefit of myocardial revascularization. Herz 2013;38:344-9.

107. Atkinson DJ, Burstein D, Edelman RR. First-pass cardiac perfusion: evaluation with ultrafast MR imaging. Radiology 1990;174:757-62.

108. Manka R, Paetsch I, Schnackenburg B, Gebker R, Fleck E, Jahnke C. BOLD cardiovascular magnetic resonance at 3.0 tesla in myocardial ischemia. Journal of cardiovascular magnetic resonance : official journal of the Society for Cardiovascular Magnetic Resonance 2010;12:54.

109. Yang HJ, Sharif B, Pang J et al. Free-breathing, motion-corrected, highly efficient whole heart T2 mapping at 3T with hybrid radial-cartesian trajectory. Magnetic resonance in medicine 2016;75:126-36.

110. Ding H, Fernandez-de-Manuel L, Schar M et al. Three-dimensional whole-heart T2 mapping at 3T. Magnetic resonance in medicine 2015;74:803-16.

111. Liu A, Wijesurendra RS, Francis JM et al. Adenosine Stress and Rest T1 Mapping Can Differentiate Between Ischemic, Infarcted, Remote, and Normal Myocardium Without the Need for Gadolinium Contrast Agents. JACC Cardiovascular imaging 2016;9:27-36.

112. Bloch F. Nuclear Induction. Phys Rev 1946;70.

113. Rongen GA, Brooks SC, Pollard MJ et al. Effect of adenosine on heart rate variability in humans. Clinical science 1999;96:597-604.

114. Sharif B, Dharmakumar R, Arsanjani R et al. Non-ECG-gated myocardial perfusion MRI using continuous magnetization-driven radial sampling. Magnetic resonance in medicine 2014;72:1620-8.

115. Kumar A, Beohar N, Arumana JM et al. CMR imaging of edema in myocardial infarction using cine balanced steady-state free precession. JACC Cardiovascular imaging 2011;4:1265-73.

116. Marshall HR, Prato FS, Deans L, Theberge J, Thompson RT, Stodilka RZ. Variable lung density consideration in attenuation correction of whole-body PET/MRI. Journal of nuclear medicine : official publication, Society of Nuclear Medicine 2012;53:977-84.

117. Vontobel J, Liga R, Possner M et al. MR-based attenuation correction for cardiac FDG PET on a hybrid PET/MRI scanner: comparison with standard CT attenuation correction. European journal of nuclear medicine and molecular imaging 2015;42:1574-80.

118. Thomasson D, Purdy D, Finn JP. Phase-modulated binomial RF pulses for fast spectrally-selective musculoskeletal imaging. Magnetic resonance in medicine 1996;35:563-8.

119. Nakazato R, Berman DS, Dey D et al. Automated quantitative Rb-82 3D PET/CT myocardial perfusion imaging: normal limits and correlation with invasive coronary angiography. Journal of nuclear cardiology : official publication of the American Society of Nuclear Cardiology 2012;19:265-76.

120. Slomka PJ. Software approach to merging molecular with anatomic information. Journal of nuclear medicine : official publication, Society of Nuclear Medicine 2004;45 Suppl 1:36S-45S.

121. Vohringer M, Flewitt JA, Green JD et al. Oxygenation-sensitive CMR for assessing vasodilator-induced changes of myocardial oxygenation. Journal of cardiovascular magnetic resonance : official journal of the Society for Cardiovascular Magnetic Resonance 2010;12:20.

122. Dharmakumar R, Hong J, Brittain JH, Plewes DB, Wright GA. Oxygen-sensitive contrast in blood for steady-state free precession imaging. Magnetic resonance in medicine 2005;53:574-83.

123. Guo H, Au WY, Cheung JS et al. Myocardial T2 quantitation in patients with iron overload at 3 Tesla. Journal of magnetic resonance imaging : JMRI 2009;30:394-400.

124. Ghugre NR, Ramanan V, Pop M et al. Myocardial BOLD imaging at 3 T using quantitative T2: application in a myocardial infarct model. Magnetic resonance in medicine 2011;66:1739-47.

125. Zoghbi GJ, Iskandrian AE. Selective adenosine agonists and myocardial perfusion imaging. Journal of nuclear cardiology : official publication of the American Society of Nuclear Cardiology 2012;19:126-41.

126. Hsin-Jung Yang, Damini Dey, Jane M Sykes et al. Towards reliable myocardial blood-oxygen-level-dependent (BOLD) CMR using late effects of regadenoson with simultaneous 13n-amm. Journal of Cardiovascular Magnetic Resonance 2016;18(Suppl 1):O19.

127. Avants BB, Tustison NJ, Song G, Cook PA, Klein A, Gee JC. A reproducible evaluation of ANTs similarity metric performance in brain image registration. Neuroimage 2011;54:2033-44.

128. Felmlee MA, Morris ME, Mager DE. Mechanism-based pharmacodynamic modeling. Methods in molecular biology 2012;929:583-600.

129. Gordi T, Frohna P, Sun HL, Wolff A, Belardinelli L, Lieu H. A population pharmacokinetic/pharmacodynamic analysis of regadenoson, an adenosine A2A-receptor agonist, in healthy male volunteers. Clinical pharmacokinetics 2006;45:1201-12.

130. Al Jaroudi W, Iskandrian AE. Regadenoson: a new myocardial stress agent. Journal of the American College of Cardiology 2009;54:1123-30.

131. Jaroudi S, Kakourou G, Cawood S et al. Expression profiling of DNA repair genes in human oocytes and blastocysts using microarrays. Human reproduction 2009;24:2649-55.

132. Markwalder J, Starling EH. A note on some factors which determine the blood-flow through the coronary circulation. The Journal of physiology 1913;47:275-85.

133. Eckenhoff JE, Hafkenschiel JH, Landmesser CM. The coronary circulation in the dog. The American journal of physiology 1947;148:582-96.

134. Eberlein HJ. [Coronary blood supply and oxygen supply of the heart under various CO2 tensions and anesthetics]. Archiv fur Kreislaufforschung 1966;50:18-87.

135. Ledingham IM, McBride TI, Parratt JR, Vance JP. The effect of hypercapnia on myocardial blood flow and metabolism. J Physiol 1970;210:87-105.

136. Scheuer J. The effects of respiratory and metabolic alkalosis on coronary flow, hemodynamics and myocardial carbohydrate metabolism. Cardiologia 1968;52:275-86.

137. van den Bos GC, Drake AJ, Noble MI. The effect of carbon dioxide upon myocardial contractile performance, blood flow and oxygen consumption. The Journal of physiology 1979;287:149-61.

138. Tzou WS, Korcarz CE, Aeschlimann SE, Morgan BJ, Skatrud JB, Stein JH. Coronary flow velocity changes in response to hypercapnia: assessment by transthoracic Doppler echocardiography. J Am Soc Echocardiogr 2007;20:421-6.

139. Momen A, Mascarenhas V, Gahremanpour A et al. Coronary blood flow responses to physiological stress in humans. American journal of physiology Heart and circulatory physiology 2009;296:H854-61.

140. Beaudin AE, Brugniaux JV, Vohringer M et al. Cerebral and myocardial blood flow responses to hypercapnia and hypoxia in humans. Am J Physiol Heart Circ Physiol 2011;301:H1678-86.

141. Yokoyama I, Inoue Y, Kinoshita T, Itoh H, Kanno I, Iida H. Heart and brain circulation and CO2 in healthy men. Acta Physiol (Oxf) 2008;193:303-8.

142. Gould KL, Johnson NP, Bateman TM et al. Anatomic versus physiologic assessment of coronary artery disease. Role of coronary flow reserve, fractional flow reserve, and positron emission tomography imaging in revascularization decision-making. Journal of the American College of Cardiology 2013;62:1639-53.

143. Ito S, Mardimae A, Han J et al. Non-invasive prospective targeting of arterial P(CO2) in subjects at rest. J Physiol 2008;586:3675-82.

144. Prisman E, Slessarev M, Azami T, Nayot D, Milosevic M, Fisher J. Modified oxygen mask to induce target levels of hyperoxia and hypercarbia during radiotherapy: a more effective alternative to carbogen. Int J Radiat Biol 2007;83:457-62.

145. Slessarev M, Han J, Mardimae A et al. Prospective targeting and control of end-tidal CO2 and O2 concentrations. The Journal of physiology 2007;581:1207-19.

146. Herzog BA, Husmann L, Valenta I et al. Long-term prognostic value of 13N-ammonia myocardial perfusion positron emission tomography added value of coronary flow reserve. J Am Coll Cardiol 2009;54:150-6.

147. Slomka PJ, Alexanderson E, Jacome R et al. Comparison of clinical tools for measurements of regional stress and rest myocardial blood flow assessed with 13N-ammonia PET/CT. Journal of nuclear medicine : official publication, Society of Nuclear Medicine 2012;53:171-81.

148. Valk PE. Positron emission tomography : basic science and clinical practice. London ; New York: Springer, 2003.

149. Kuhle WG, Porenta G, Huang SC et al. Quantification of regional myocardial blood flow using 13N-ammonia and reoriented dynamic positron emission tomographic imaging. Circulation 1992;86:1004-17.

150. Camici PG, Gropler RJ, Jones T et al. The impact of myocardial blood flow quantitation with PET on the understanding of cardiac diseases. European heart journal 1996;17:25-34.

151. Riou LM, Ruiz M, Rieger JM et al. Influence of propranolol, enalaprilat, verapamil, and caffeine on adenosine A(2A)-receptor-mediated coronary vasodilation. J Am Coll Cardiol 2002;40:1687-94.

152. Bottcher M, Czernin J, Sun KT, Phelps ME, Schelbert HR. Effect of caffeine on myocardial blood flow at rest and during pharmacological vasodilation. Journal of nuclear medicine : official publication, Society of Nuclear Medicine 1995;36:2016-21.

153. Wilke N, Simm C, Zhang J et al. Contrast-enhanced first pass myocardial perfusion imaging: correlation between myocardial blood flow in dogs at rest and during hyperemia. Magnetic resonance in medicine 1993;29:485-97.

154. Nakazato R, Dey D, Alexanderson E et al. Automatic alignment of myocardial perfusion PET and 64-slice coronary CT angiography on hybrid PET/CT. Journal of nuclear cardiology : official publication of the American Society of Nuclear Cardiology 2012;19:482-91.

155. Slomka PJ, Nishina H, Berman DS et al. Automatic quantification of myocardial perfusion stress-rest change: a new measure of ischemia. Journal of nuclear medicine : official publication, Society of Nuclear Medicine 2004;45:183-91.

156. Feihl F, Perret C. Permissive hypercapnia. How permissive should we be? American journal of respiratory and critical care medicine 1994;150:1722-37.

157. Druz RS. Current advances in vasodilator pharmacological stress perfusion imaging. Seminars in nuclear medicine 2009;39:204-9.

158. Klocke FJ, Simonetti OP, Judd RM et al. Limits of detection of regional differences in vasodilated flow in viable myocardium by first-pass magnetic resonance perfusion imaging. Circulation 2001;104:2412-6.

159. Guerrero A, Singer JJ, Fay FS. Simultaneous measurement of Ca2+ release and influx into smooth muscle cells in response to caffeine. A novel approach for calculating the fraction of current carried by calcium. The Journal of general physiology 1994;104:395-422.

160. Ahn HY, Karaki H, Urakawa N. Inhibitory effects of caffeine on contractions and calcium movement in vascular and intestinal smooth muscle. British journal of pharmacology 1988;93:267-74.

161. Frumin MJ, Epstein RM, Cohen G. Apneic oxygenation in man. Anesthesiology 1959;20:789-98.

162. Trochu JN, Zhao G, Post H et al. Selective A2A adenosine receptor agonist as a coronary vasodilator in conscious dogs: potential for use in myocardial perfusion imaging. Journal of cardiovascular pharmacology 2003;41:132-9.

163. Potkin RT, Swenson ER. Resuscitation from severe acute hypercapnia. Determinants of tolerance and survival. Chest 1992;102:1742-5.

164. Willie CK, Tzeng YC, Fisher JA, Ainslie PN. Integrative regulation of human brain blood flow. The Journal of physiology 2014;592:841-59.

165. Brian JE, Jr. Carbon dioxide and the cerebral circulation. Anesthesiology 1998;88:1365-86.

166. Javadi MS, Lautamaki R, Merrill J et al. Definition of vascular territories on myocardial perfusion images by integration with true coronary anatomy: a hybrid PET/CT analysis. J Nucl Med 2010;51:198-203.

167. Scheel KW, Ingram LA, Gordey RL. Relationship of coronary flow and perfusion territory in dogs. The American journal of physiology 1982;243:H738-47.

168. Abuchaim DC, Tanamati C, Jatene MB, Marcial ML, Aiello VD. Coronary dominance patterns in hypoplastic left heart syndrome. Revista brasileira de cirurgia cardiovascular : orgao oficial da Sociedade Brasileira de Cirurgia Cardiovascular 2011;26:604-8.

169. Aldweib N, Negishi K, Hachamovitch R, Jaber WA, Seicean S, Marwick TH. Impact of repeat myocardial revascularization on outcome in patients with silent ischemia after previous revascularization. Journal of the American College of Cardiology 2013;61:1616-23.

170. Harper AM, Glass HI. Effect of alterations in the arterial carbon dioxide tension on the blood flow through the cerebral cortex at normal and low arterial blood pressures. J Neurol Neurosurg Psychiatry 1965;28:449-52.

171. Guensch DP, Fischer K, Flewitt JA, Friedrich MG. Impact of intermittent apnea on myocardial tissue oxygenation--a study using oxygenation-sensitive cardiovascular magnetic resonance. PloS one 2013;8:e53282.

172. Spano VR, Mandell DM, Poublanc J et al. CO2 blood oxygen level-dependent MR mapping of cerebrovascular reserve in a clinical population: safety, tolerability, and technical feasibility. Radiology 2013;266:592-8.

173. Wise RG, Pattinson KT, Bulte DP et al. Dynamic forcing of end-tidal carbon dioxide and oxygen applied to functional magnetic resonance imaging. J Cereb Blood Flow Metab 2007;27:1521-32.

174. Karamitsos TD, Leccisotti L, Arnold JR et al. Relationship between regional myocardial oxygenation and perfusion in patients with coronary artery disease: insights from cardiovascular magnetic resonance and positron emission tomography. Circ Cardiovasc Imaging 2011;3:32-40.

175. Wolf GK, Gomez-Laberge C, Kheir JN et al. Reversal of dependent lung collapse predicts response to lung recruitment in children with early acute lung injury. Pediatric critical care medicine : a journal of the Society of Critical Care Medicine and the World Federation of Pediatric Intensive and Critical Care Societies 2012;13:509-15.

176. Pauling L, Coryell CD. The Magnetic Properties and Structure of Hemoglobin, Oxyhemoglobin and Carbonmonoxyhemoglobin. Proceedings of the National Academy of Sciences of the United States of America 1936;22:210-6.

177. Baddeley H, Brodrick PM, Taylor NJ et al. Gas exchange parameters in radiotherapy patients during breathing of 2%, 3.5% and 5% carbogen gas mixtures. Br J Radiol 2000;73:1100-4.

178. Foex P, Ryder WA. Effect of CO2 on the systemic and coronary circulations and on coronary sinus blood gas tensions. Bull Eur Physiopathol Respir 1979;15:625-38.

179. Mark CI, Slessarev M, Ito S, Han J, Fisher JA, Pike GB. Precise control of end-tidal carbon dioxide and oxygen improves BOLD and ASL cerebrovascular reactivity measures. Magn Reson Med 2010;64:749-56.

180. Case RB, Greenberg H. The response of canine coronary vascular resistance to local alterations in coronary arterial P CO2. Circ Res 1976;39:558-66.

181. Powers ER, Bannerman KS, Fitz-James I, Cannon PJ. Effect of elevations of coronary artery partial pressure of carbon dioxide (PCO2) on coronary blood flow. J Am Coll Cardiol 1986;8:1175-81.

182. Fierstra J, Machina M, Battisti-Charbonney A, Duffin J, Fisher JA, Minkovich L. End-inspiratory rebreathing reduces the end-tidal to arterial PCO2 gradient in mechanically ventilated pigs. Intensive care medicine 2011;37:1543-50.

183. Sasse SA, Berry RB, Nguyen TK, Light RW, Mahutte CK. Arterial blood gas changes during breath-holding from functional residual capacity. Chest 1996;110:958-64.

184. St Croix CM, Cunningham DA, Kowalchuk JM et al. Estimation of arterial PCO2 in the elderly. J Appl Physiol 1995;79:2086-93.

185. Midgren B, Hansson L. Changes in transcutaneous PCO2 with sleep in normal subjects and in patients with chronic respiratory diseases. European journal of respiratory diseases 1987;71:388-94.

186. E. P. Trulock I. Arterial Blood Gases. In: Walker HK HW, Hurst JW, editor Clinical Methods: The History, Physical, and Laboratory Examinations. 3 ed. Boston: Butterworths, 1990.

187. Karamitsos TD, Dass S, Suttie J et al. Blunted myocardial oxygenation response during vasodilator stress in patients with hypertrophic cardiomyopathy. Journal of the American College of Cardiology 2013;61:1169-76.

188. Ashikawa K, Kanatsuka H, Suzuki T, Takishima T. Phasic blood flow velocity pattern in epimyocardial microvessels in the beating canine left ventricle. Circ Res 1986;59:704-11.